Spring 5-2015

Petrogenesis and Paleostress Analysis of the Mesozoic Mill Brook Dike Zone in the Mount Dartmouth 7.5' Quadrangle, New Hampshire

Graham Grear Oxman
Bates College, goxman@bates.edu

Petrogenesis and Paleostress Analysis of the Mesozoic Mill Brook Dike Zone in the Mount Dartmouth 7.5' Quadrangle, New Hampshire

Presented to
The Faculty of the Department of Geology
Bates College

An Honors Thesis
In partial fulfillment of the requirements for the
Degree of Bachelor of Science

By
Graham Grear Oxman
Lewiston, ME
March 30, 2015

Table of Contents

Table of Figures

Acknowledgements

I have enormous gratitude for Dyk Eusden, for his invaluable advice and guidance throughout the writing and work done for this thesis. His enthusiasm and excellent teaching have been inspirational to me, and his love of the White Mountains and their geology have imbued me with an appreciation of geology that will remain with me for a long time to come. I am forever grateful to Bev Johnson, for being a source of wisdom, always pushing me to be better, and not letting me give in. I would like to thank Genevieve Robert for her guidance and patience with me. I would also like to thank Holly Gurney for helping me to make my academic experience at Bates the best it could possibly be, and always being willing to lend a listening ear. A thank you as well to the rest of the Geology Department and the Imaging Center.

I wouldn't have made it through this process without the company of some of the best people I have had the privilege to know: Dan, Cheyenne, the Twins, Zoe, Jackie, Noel, Grace, just to name a few. To name them all would be another whole document unto itself, but you all know who you are. I am eternally grateful to you all for supporting me through this stressful (yet rewarding!) process, and offering support and incentives all along the way. Thank you for listening to me both kvetch and rejoice about my thesis. I can only hope I have been as good a friend to you all as you have been to me.

I have been lucky to have been given a wonderful family. I wouldn't be the man I am today without my father and brother. Dad, thank you for always being there for me, no matter what time of day it is and no matter how esoteric my concern was. Your tough love pushed me to finish this project, and pushed me to ask more of myself. William, your quick wit never failed to bring me back to myself. Thank you both.

Light is not so much something that reveals, as it is itself the revelation.

-James Turrell

Abstract

Field mapping linked with petrogenetic and brittle structural studies of Mesozoic basalt dikes was performed in the Mount Dartmouth 7.5' Quadrangle, adjacent to the Presidential Range, NH. This was done in hopes of creating a better understanding of the intrusion and brittle deformational history of the basalt dikes, particularly in relation to the regional tectonic context. Field work done during the summer of 2014 revealed a 100 meter wide, 7.8 km long zone containing multiple mafic dikes that are exceptionally well exposed at the junction of NH Rt. 115 and the Cherry Mountain road. The largest dike in the zone is approximately 20 meters in width, comparable in size to the largest dikes mapped in the Northeast (e.g. Christmas Cove dike, Higganum dike).

The newly named Mill Brook Dike Zone was previously discovered and described by Katherine Fowler-Billings in 1944. The orientation of the Dike Zone is N-S and steeply dipping. Within the zone, the strike and dip of dikes ranges from 207, 63°SE to 178, 79°W to 5, 69°E. The chill margins were approximately 3-5 cm in from edge of dike, while the core of the dike contained 1-3 cm subhedral plagioclase grains, creating a porphyritic texture. When viewed in thin section, the plagioclase grains show significant magmatic oscillatory zoning. Additionally, there is notable alteration of the pyroxenes and amphiboles, primarily sericite and chlorite alteration. In some samples there is cataclasis of all the grains, likely due to hydrothermal alteration during faulting.

The Mill Brook dike cuts through the Jurassic Cherry Mountain syenite pluton along the western edge of the quadrangle, but was not observed to crosscut the Jurassic Conway granite in the south of the quadrangle. A regional, dike-parallel N-S, steeply dipping joint set was also discovered. Previous work in the adjacent Mount Washington region found mafic intrusions and associated joints striking (from oldest to youngest) NE-SW and E-W, but found only joints and no dikes striking N-S related to the youngest joint set. Additionally, no E-W striking joints were observed in the Mount Dartmouth quadrangle. Comparison of fracture data between the two areas of greatest outcrop exposure (Upper Falls and the Mill Brook Bridge) revealed restriction of the N-S paleostress field to the Mill Brook area. This indicates local variations in paleostress fields on a much smaller order of magnitude than previously thought.

Geochemical data from the Mill Brook Dike Zone shows a fractionation trend, indicating that the N-S striking dikes are of one magmatic suite. The data also show that the Mill Brook Dike Zone is geochemically distinct from other comparably large mafic intrusions in the Northeast, signifying that the Mill Brook Dike Zone did not form as part of the Central Atlantic Magmatic Province (CAMP). The Mill Brook Dike Zone and its joints are likely younger than the Late Cretaceous New England-Quebec igneous province and record a significant period of basalt magmatism during E-W extension in the Cretaceous.

1. Introduction

1.1 Purpose

Four hundred sixty million years ago, the creation of Pangea began with the Taconic orogeny. After four additional orogenies, the landmasses of Laurentia and Gondwana combined to form Pangea. For many million years, little major tectonic activity occurred. This changed approximately 200 million years ago, when the separation of Gondwana and Laurentia began (Figure 1). The rifting of these two continents caused extensive brittle deformation along the modern-day east coast of North America. This brittle deformation is exhibited as normal faulting, mafic intrusions, and joints.

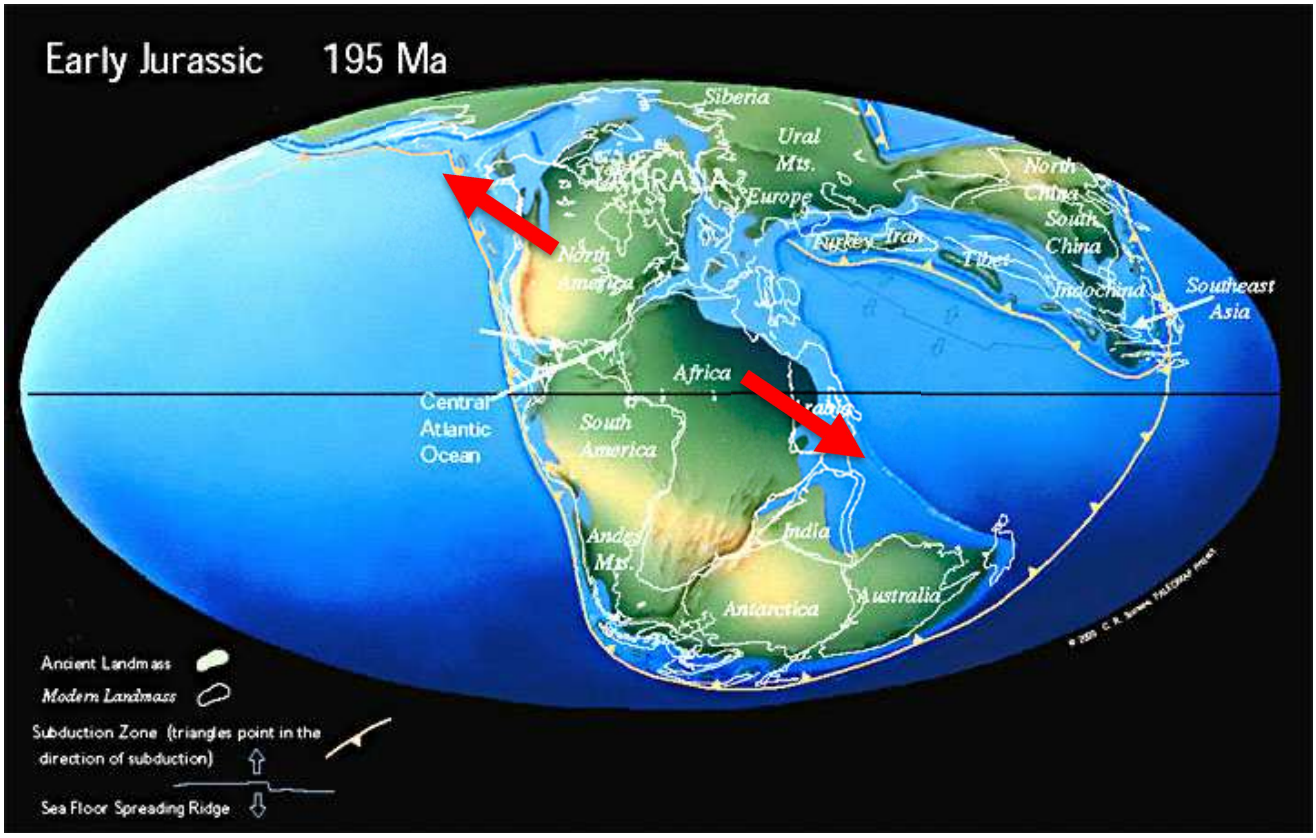

Figure 1: The paleomap of the Early Jurassic (195 Ma) shows the orientation of tectonic plates prior to the rifting event. The red paired arrows show the relative direction of rifting of the North American and African plates. (Modified from Scotese, 2010).

In-depth regional work has been done using the mafic intrusions and joint sets to reconstruct the paleostress orientations primarily in New England and Quebec (McHone and

Butler, 1984; McHone 1988; Faure et al., 1996a, Faure et al., 1996b, Faure et al., 2006). Yet as instructive as this work is, it is a simplification on a regional scale, and does not necessarily reflect the complexity seen on a local scale. Some work has been undertaken to understand the local paleostress fields of New Hampshire, specifically in the White Mountains and the areas adjacent to them, but more needs to be done to facilitate a greater understanding of Mesozoic extensional events in the Northern Appalachians. Higher resolution mapping of fractures and dikes can be used to correlate local extensional history to regional Mesozoic extension, with the potential to revamp regional studies.

In particular, this study focuses on reconstructing the Mesozoic paleostress orientations in the Mount Dartmouth 7.5" Quadrangle, New Hampshire. The Mount Dartmouth Quadrangle is the quadrangle immediately west of the Mount Washington Quadrangle, which contains the majority of the Presidential Range. This study purports to add to previous similar studies done by Castro (2010), Gardner (2010), and Kindley (2011), all of which mapped dikes and fractures in the Presidential Range. The proximity of the Mount Dartmouth Quadrangle to the Presidential Range presents an excellent opportunity to extend the previous work across several rock units into a greater local understanding of the deformational history of the White Mountain area in New Hampshire.

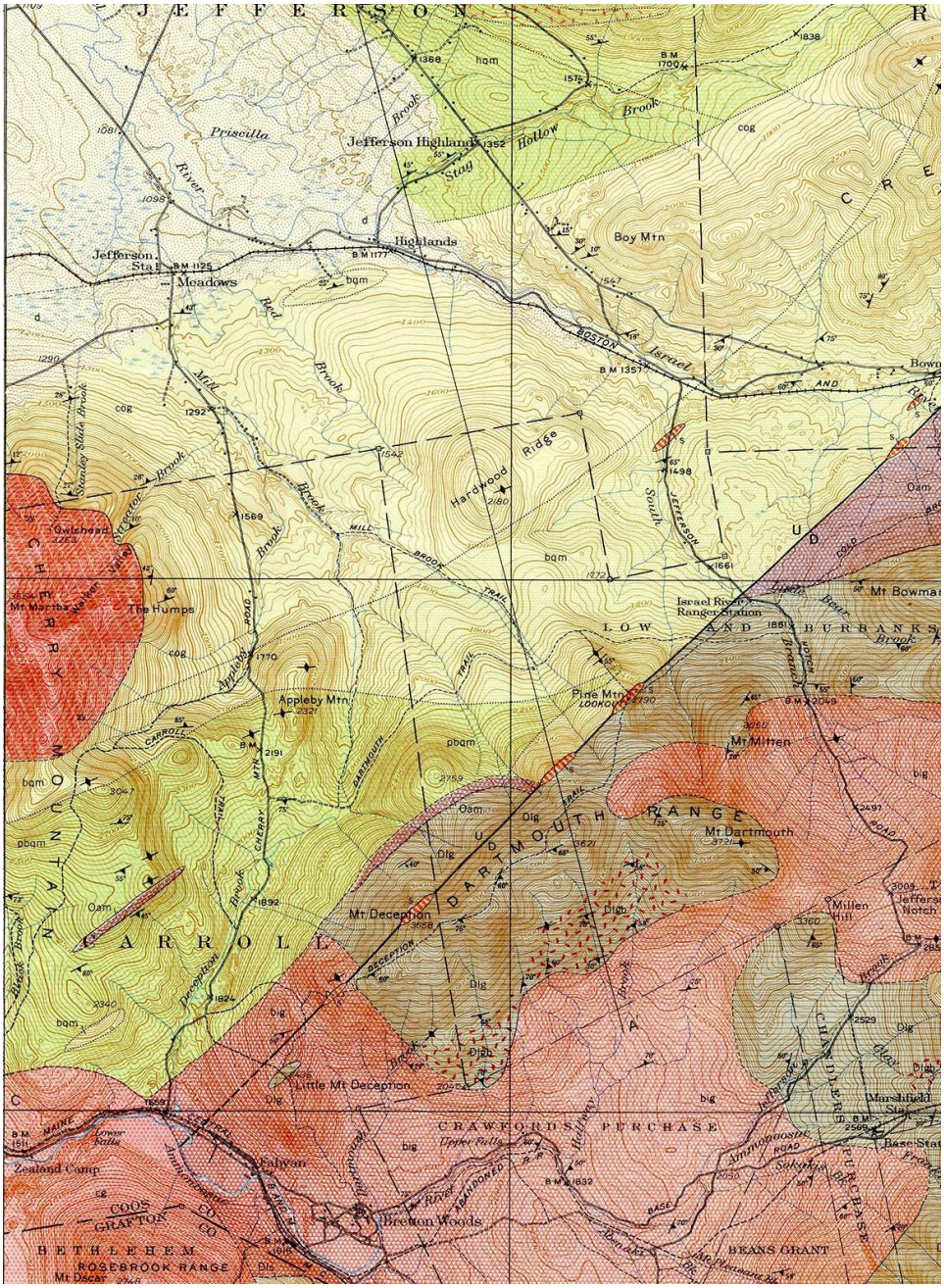

Figure 2: The map published in the 1940's by Marland P. Billings and Katherine Fowler-Billings. The major fault cutting through the quadrangle is the Pine Peak Fault, along with its associated silicified zones. The rock units indicated by the shades of green belong to the Oliverian series. The large red polygon in the middle left is the Cherry Mountain Syenite. The stippled purple represents the Ammonoosuc Volcanics. The light red polygons around the Bretton Woods area are both the Bretton Woods granite and the Conway granite (lower left corner). The rock unit composing the bulk of the Dartmouth range (gray-green in color) is the Rangeley Formation (Billings et al., 1946).

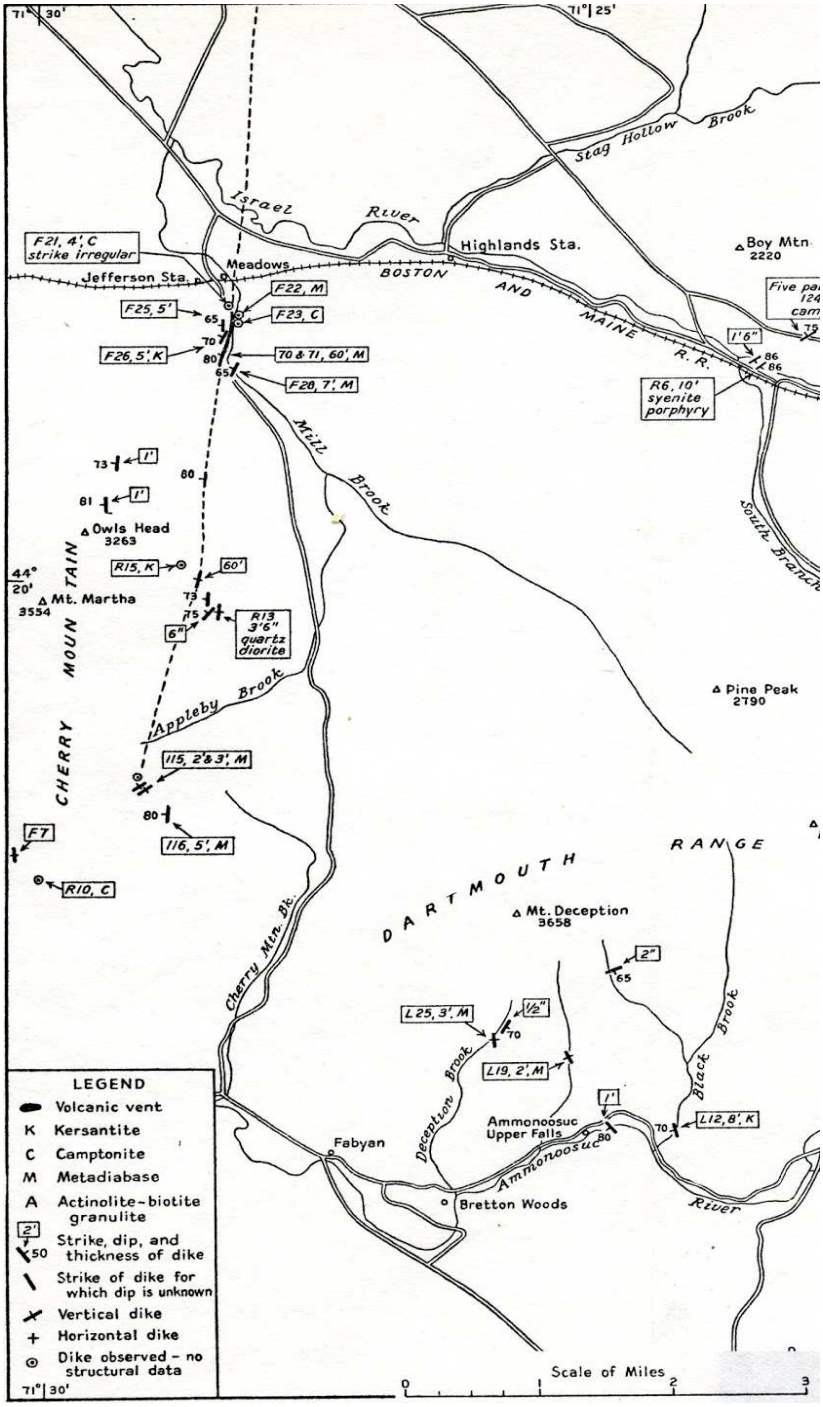

Figure 3: Katherine Fowler-Billings map of the various mafic dikes present in the Mount Dartmouth Quadrangle. The width of each dike is plotted alongside its strike and dip symbol. Additionally, the rock type is also noted alongside the size of the dike. Note the large dike that begins in the upper left corner and continues to halfway through the quad along the western edge. There is a scale in the lower right corner (Fowler-Billings, 1944).

The Mount Dartmouth Quadrangle was last mapped in the 1940's by Marland Billings and Katherine Fowler-Billings (see Figure 2). Fowler-Billings additionally mapped the mafic intrusions of the quadrangle in 1944, finding 122 separate dikes (Figure 3). Fowler-Billings (1944) found four orientations of mafic dikes in the quadrangle. The quadrangle itself does not have many accessible exposures of bedrock, but there are several excellent locations of exposure. The quadrangle is also characterized by a variety of rock types, including those associated with the Jefferson Dome complex (Billings et al., 1946).

The primary goals of this study were to: 1) map the basalt dikes and associated fractures in the field; 2) determine which brittle structures can be correlated to the observed mafic intrusions; 3) perform a petrographic and geochemical analysis on the basalts in order to evaluate their petrogenesis and tectonic setting; and 4) to determine the sequence of, and paleostress fields for, the intrusion of these basalts and their associated fractures. This project built on previous work done by Castro (2010), Gardner (2010) and Kindley (2011).

1.2 Regional Geologic Setting

1.2a Terranes

Taconian metamorphism resulted in upper-amphibolite facies in New England, while the foreland deposits suggest volcanic arcs associated with the closing of the Iapetus Ocean (Hatcher, 2010). The major suture associated with the Taconic orogeny forms the Baie Verte-Brompton line extending from Newfoundland through New England. Hatcher (2010) stated that the Taconic orogeny is associated with arc-accretion. The Salinic orogeny began in the late Silurian when the Ordovician Tetagouche-Exploits back-arc basin subducted beneath Laurentia (Reusch and van Staal, 2011). During this time, Gander accreted to Laurentia, and became the basement on which the Central Maine Basin sediments were deposited (Dorais et al., 2009). In particular, it was the collision of the Ganderian St. Croix block with Laurentia that caused the Salinic Orogeny (Reusch and van Staal, 2011). The Acadian and Neo-Acadian orogeny are associated with the closing of the Rheic Ocean, which Hatcher (2010) refers to as the "zippered north-to-south closing" as Avalon and Carolinia collided with Laurentia. This orogeny is characterized by large terrane accretion. Hatcher (2010) proposes that the Alleghanian orogeny comprised rotation and transpression of the Gondwana and Laurentia continents, based on fault kinematics and stratigraphy. This resulted in the formation of

Pangea. Hatcher (2010) proposes that this zipper-like closure began in the northeastern Appalachians, and closed the Theic Ocean. All orogenies are associated with minimum metamorphic amphibolite-facies, bimodal volcanism, and clastic wedges (Hatcher, 2010).

The study area is in the Gander terrane (Figure 4). It is adjacent to the axis of the Central Maine Basin (CMB, also sometimes referred to as the Central Maine Terrane), which is comprised of Paleozoic metasedimentary and Paleozoic to Mesozoic units (Dorais, 2003). The Bronson Hill Anticlinorium, a belt of two Ordovician volcanic sequences, forms the boundary of the basin to the west and north, and the Massabesic Gneiss Complex and the Merrimack Trough form the boundary to the south and east. (Stewart, 1991; Moench and Aleinikoff, 2002; Eusden, 1996a). The Merrimack Trough is in fault contact with the Massabesic Gneiss Complex, and is composed of sequences of Devonian pelites and graywackes overlying Silurian turbidites (Dorais, 2009; Tremblay and Pinet, 2005). It has been proposed by Reusch and van Staal (2012) that the Massabesic Gneiss complex represents the basement of the Central Maine Trough. More specifically, the study area is immediately bounded by the Kearsage Central Maine Synclinorium to the west, and the Central New Hampshire Anticlinorium to the east.

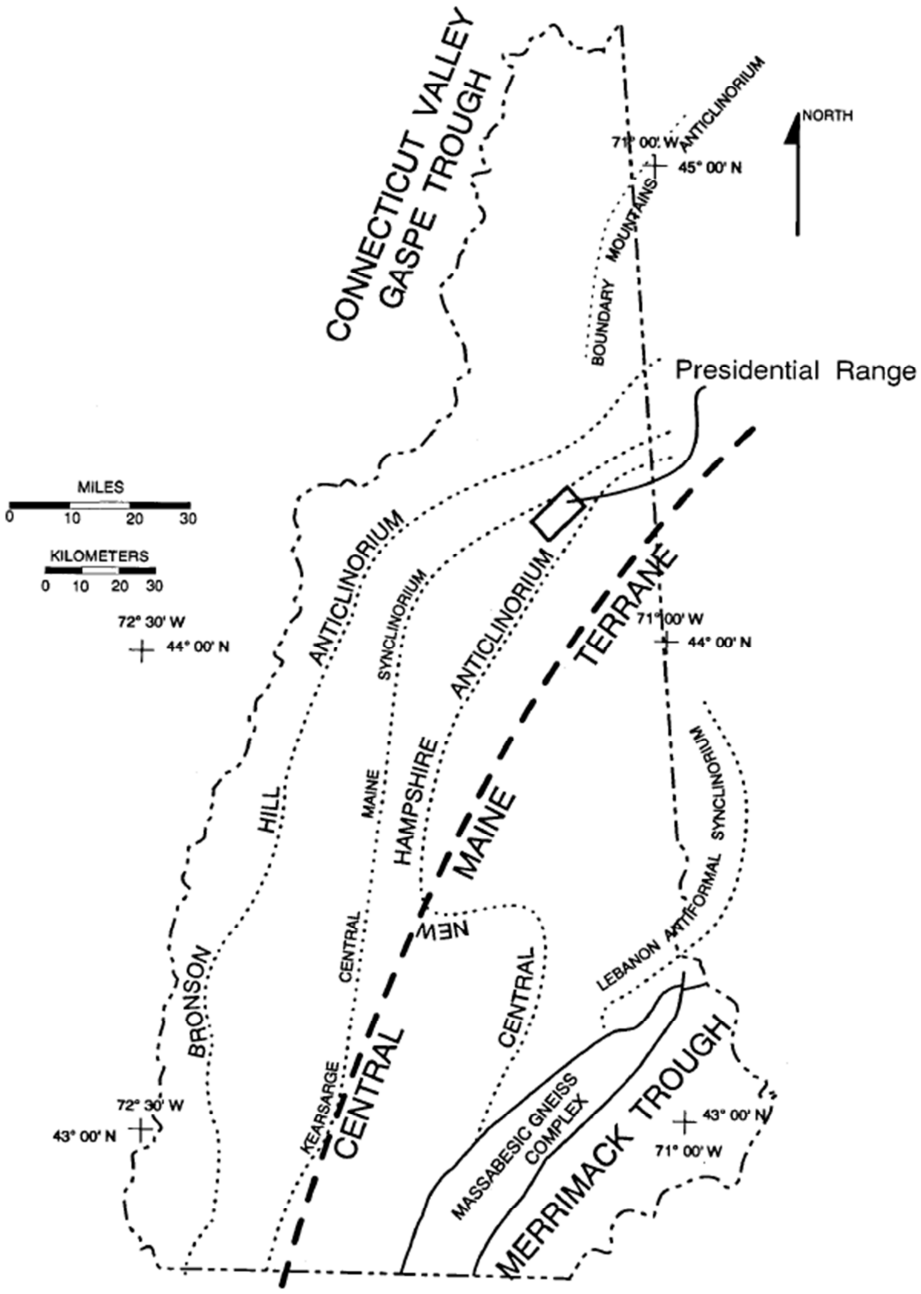

Figure 4: Structural map of New Hampshire. Approximate study location indicated by box labeled "Presidential Range." For the purposes of this work, the Central Maine Terrane is referred to as the Central Maine Basin (Eusden et al., 1996).

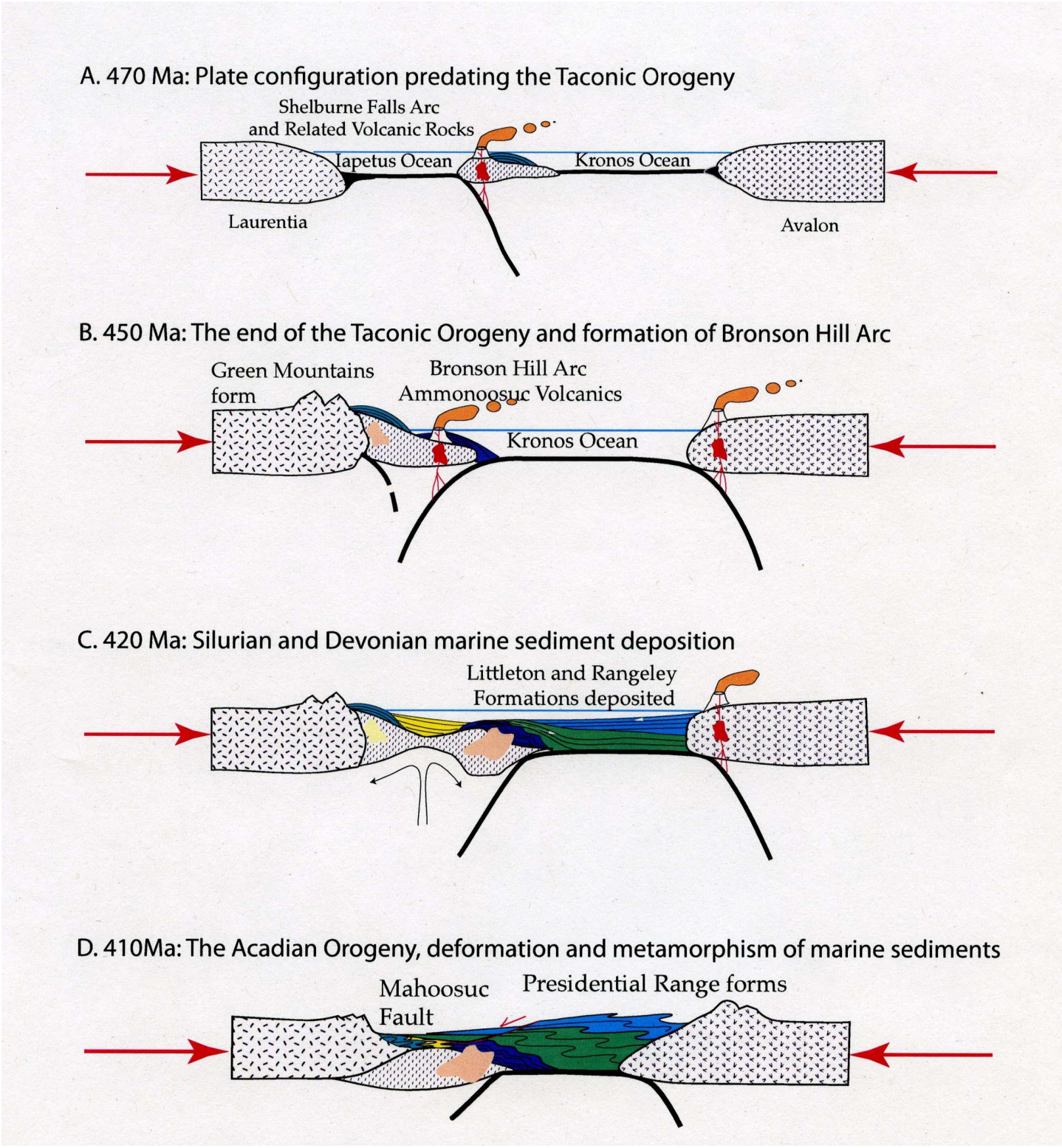

Figure 5: Four cross-sectional diagrams illustrating tectonic events from 470 Ma to 410 Ma. Particular attention is paid to the deformation and formation of the Presidential Range. (Modified from Eusden, 2010).

1.3 Collisional Tectonic History

An overview of the collisional tectonic history can be seen in Figure 5. Sediment derived from Laurentia was deposited in the middle Silurian, after closure of the Iapetus Ocean at the end of the Taconic Orogeny (Hibbard et al., 2007; Dorais, 2009). Part of these sediments became the marine turbidites now associated with the Central Maine Terrane (CMT), which formed in the Tetagouche-Exploits back-arc basin (Eusden, 2013; Reusch, 2012).

The Salinic orogeny began when back-arc basins subducted beneath Laurentia, and the associated volcanic arcs accreted to Laurentia. The closure of the Tetagouche-Exploits basin and subsequent beginning of the Taconic Orogen is marked by the St. Croix block as Gander moved towards Laurentia (Reusch, 2010). The Taconian suture, as proposed by Hatcher (2010), is represented by the Baie Verte-Brompton Line, which is in turn composed of various faults. Work by Reusch (2012) places the suture associated with the closure of the Tetagouche-Exploits basin at the Dog Bay line, marking the transition from accretion to collision.

During the Devonian Acadian orogeny, Avalon accreted to Gander, resulting in the majority of the metamorphism and deformation in New England and neighboring Canadian Appalachians (Hatcher, 2010). This metamorphism and deformation happened in several steps, with the majority of the deformation happening until 355 Ma, while metamorphism took place between 405-402 Ma (Eusden et al., 2000).

Following the Acadian orogeny in the Devonian and Carboniferous, intrusion of granites during melting of thickened continental crust caused mild metamorphism and deformation. This is associated with Neoacadian Orogeny (Eusden, 2013). Ultimately, during the Permian, the remainder of Gondwana collided with Laurentia to create Pangea in the Alleghanian Orogeny. This caused regional uplift, but no major deformation of the rocks in central New Hampshire (Hibbard et al., 2007).

1.4 Presidential Range Geology

The majority of the rocks that compose the Presidential Range fall in between the Silurian to Devonian ages. The rocks are of metasedimentary origins, with mafic dike intrusions scattered throughout. These rocks are considered part of the Central Maine Basin, and have experienced several episodes of metamorphism and ductile deformation at different points in time (Eusden, 2010; Eusden et al, 2006). They were deposited after the Taconic orogeny, during the Salinic, as well as during the Acadian (Bradley et al., 2000). The deposition and subsequent metamorphism of these formations over such a long stretch of time presents an opportunity to study the ductile deformation of the region.

The Presidential Range contains five metasedimentary rock formations which are, in order of oldest to youngest, the Silurian Rangeley, Perry Mountain, Small Falls, Madrid and Devonian Littleton Formation. Two of the rock units found in the Mount Washington quad stretch into the neighboring Mount Dartmouth quad. These are the Silurian Rangeley Formation, and the Devonian Littleton Formation (Eusden, 2010; Eusden et al, 2006).

1.5 Ductile Deformation

The understanding of the deformational history of the Presidential Range has undergone several revisions since the early 1900's, subject to the advent of new technology, such as GPS and apatite fission-track. The area was first extensively mapped by Billings et al (1946) and was later amplified by Hatch and Moench (1984), when they correlated rock units from across the border from Maine through the Presidential Range into New Hampshire. Recent efforts spearheaded by Eusden and others have yielded a much more detailed understanding of deformational history in the Presidential Range.

The Presidential Range is largely composed of the above-mentioned Silurian and Devonian metasedimentary formations. Eusden (2010) has proposed six deformational events, denoted by $D_{\#}$. Four of these deformation events include folding, denoted by $F_{\#}$. Fabrics associated with these deformational events are denoted by $S_{\#}$.

D_0 is characterized by pre-metamorphic faulting, creating the Moose River and Mahoosuc faults. Eusden et al. (2000) have constrained this event to pre-408 Ma as shown by

U-Pb zircon dating from the Wamsutta diorite in Great Gulf. Therefore, this D_0 event occurred before the collision of Avalon with the Laurentian Composite terrane. D_1 deformation occurred during the Acadian orogeny, as the orogenic front collided with the Bronson Hill arc (Eusden et al., 2006).This deformation event is characterized by reclined, isoclinal, cylindrical F_1 folds. The macroscopic folds are approximately 3 kilometers in wavelength, while the mesoscopic folds have wavelengths of 10 meters (Eusden et al., 1996). D_1 folds deform bedding, and the resulting fabric is termed S_0. This caused foliation to form sub-parallel to the folding, indicating that the deformation was syn-metamorphic (Eusden et al., 2006).

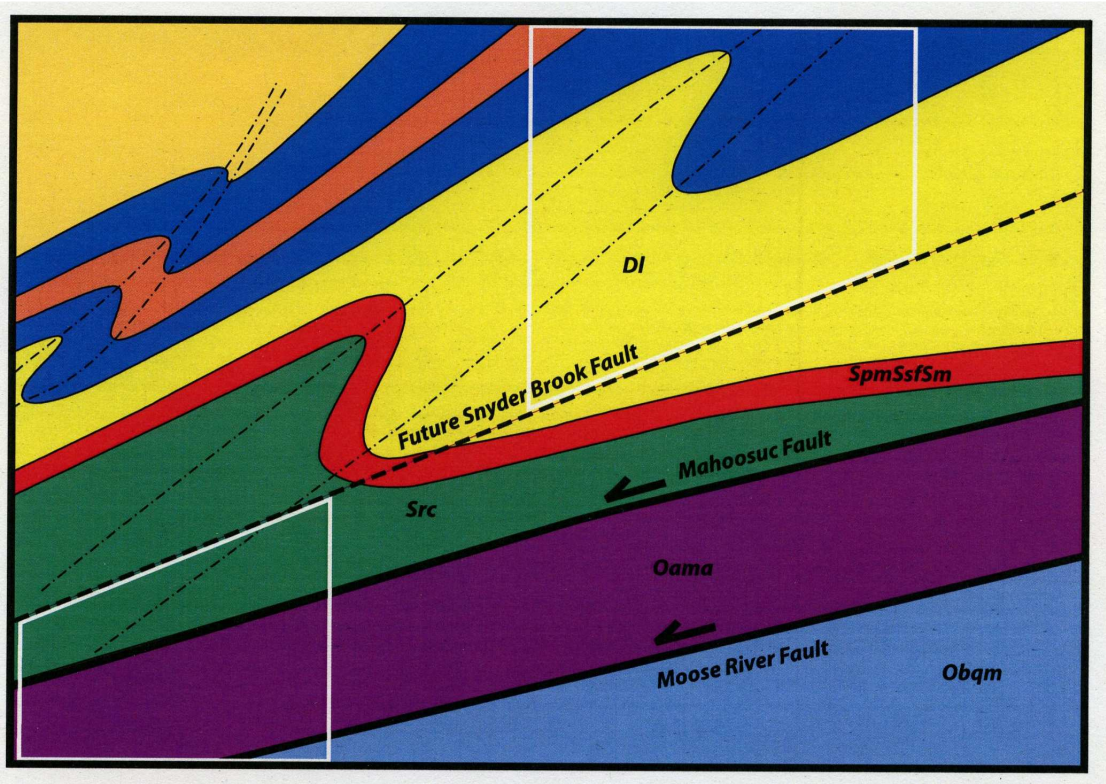

Figure 6: D_0 and S_1 formation, using the White Mountain range. Bold lines indicate brittle D_0 faulting, while the dashed lines indicate S_1 axial planes that lie along F_1 folding (Eusden, 2010).

D_2 deformational folding is quite different from D_1 folding, instead it is characterized by open, gently southwest-to-south plunging, moderate to steeply inclined folds. D_2 folds deform both S_0 and S_1 fabrics (Eusden et al., 1996). The most obvious example of D_2 deformation is the Snyder Brook fault, indicating that D_2 deformation was also characterized by thrust faulting. This thrust faulting along the Snyder Brook fault allowed the Rangeley formation to be juxtaposed next to the Littleton formation, thereby allowing metamorphic fluid to migmatize part of the Littleton.

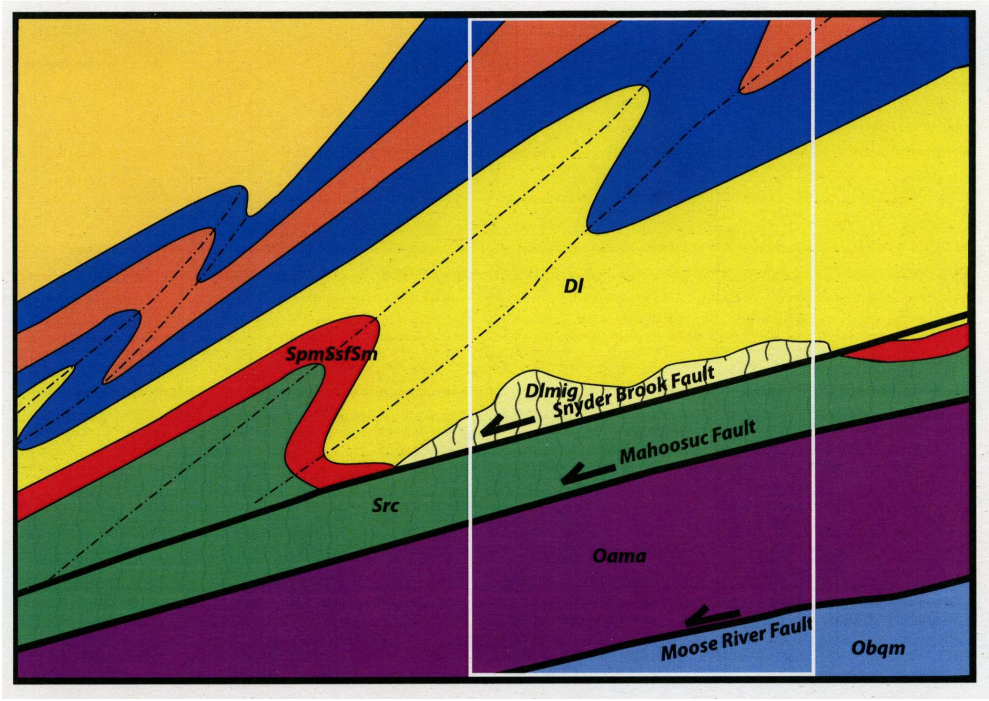

Figure 7: In the second stage of Presidential Range deformation, thrust faulting begins. This creates the Snyder Brook Fault. Later ductile deformation will alter these faults (Eusden, 2010).

D_3 folds are characterized by easterly dips of S_0 bedding and D_1 foliation (S_1), as well as macroscopic refolding of D_2 thrusts (Allen et al., 2001). F_3 folds are mesoscopic, moderately inclined to overturned, often moderately plunging and assymetric. These folds have no well-developed S_3 cleavage (Eusden et al., 1996). However, the S_3 fabric itself is consistent in orientation throughout the alpine zone in the Presidential Range (Eusden et al., 1996). These folds also define the Chandler Ridge Dome (Allen et al., 2001).

D_4 folds occurred post-peak metamorphism (Eusden et al., 2006). This deformation event is characterized by primarily mesoscopic folds in the Littleton Formation, and thereby fold all previous fabrics. They are the most common structural feature in the Presidential Range (Allen et al., 2001).

The last observed phase of deformation is D_5, characterized by crenulation restricted to the Pinkham Notch area (Allen et al., 2001). All previous F structures (F_0-F_5) are cross-cut by intrusives, such as the Bickford granite. There are several associated magmatic events associated with the Bickford granite, such as the Bretton Woods pluton. These record the last moments of the Acadian orogeny (Eusden et al., 2006).

1.6 Lithologic Units

1.6a Silurian Rangeley Formation

The Rangeley Formation is a gray migmatitic paragneiss, interbedded locally with biotite-schist (Figure 8). In some locations, the formation also contains ellipsoidal chunks of calc-silicate granofels. These lenses are often aligned parallel to schistosity, but there are a few locations where there is no alignment between schistosity and the calc-silicate pods. The pods are approximately 0.2 to 1 meter long.

Sediments composing the Rangeley are conjectured to be due to erosion of the Bronson Hill volcanic arcs, and subsequently deposited in the Kronos Ocean around 430 Ma (Eusden, 2010; Hanson and Bradley, 1989; Moench and Aleinikoff, 2002).

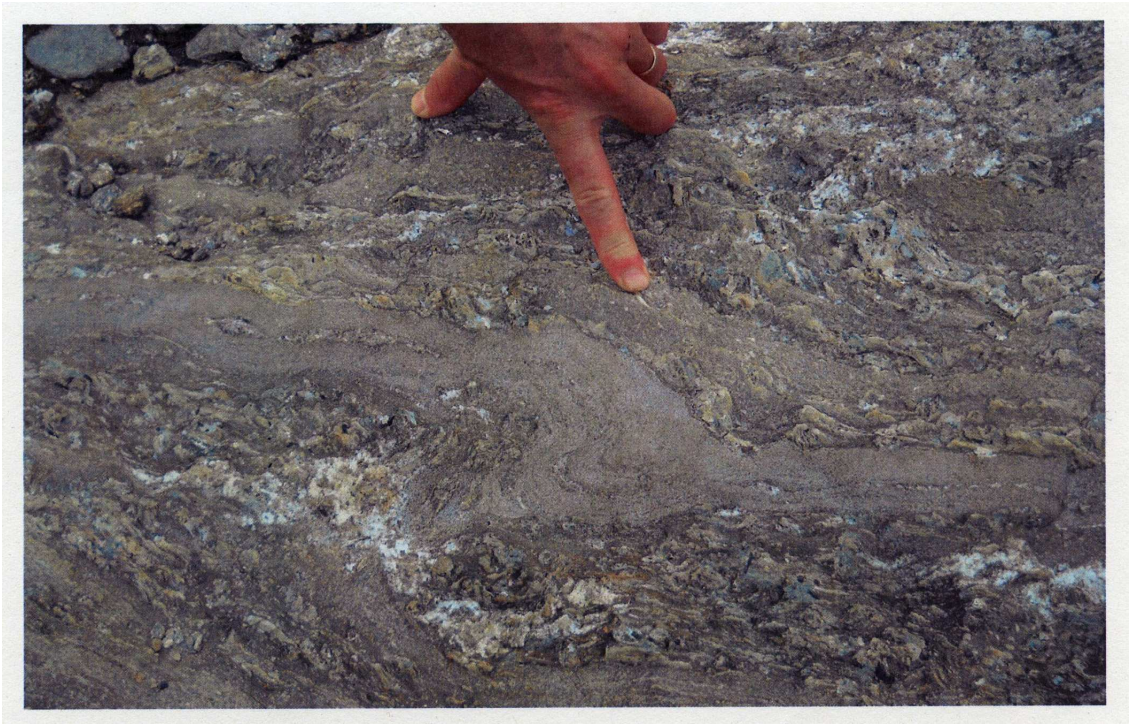

Figure 8: Rangeley Formation in Presidential Range. Note the migmatic textures, the banding present in the photos is a typical texture in the Presidential Range. Image from Eusden, 2010.

1.6b Devonian Littleton Formation

The Littleton Formation is composed of alternating bands of dark gray schist and interbedded, fine-grained, light gray quartzite layers (Figure 9). The schists are well foliated. Andalusite is present in the formation, in some areas it has been entirely pseudomorphed by muscovite, sillimanite and sericite. The lumpy crystals are 1-3 centimeters in diameter, while the elongate aggregates are 1-15 centimeters in length. The elongate aggregates contain cores of pink andalusite and chiastolite (Eusden et al., 1996). These rocks have been interpreted as marine turbidites, composed of alternating sand and mud. (Eusden, 2010). The Littleton Formation occurs throughout the Presidential Range, from Pinkham Notch to Pine Mountain, as well as from Glen House to Snyder Brook fault (Eusden, 2010).

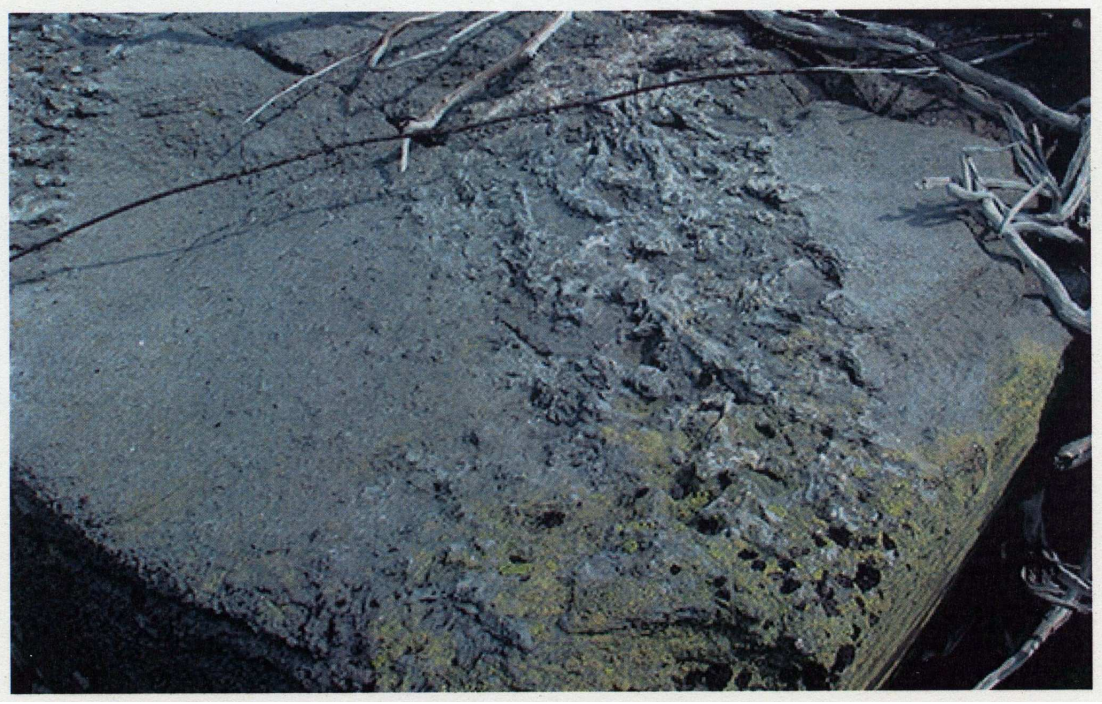

Figure 9: Devonian Littleton Formation. In particular, note the lumpy section of porphyroblastic andalusite schist and the smooth (by comparison) quartzite (Image from Eusden, 2010).

1.6c Ammonoosuc Volcanics

The Ammonoosuc Volcanics are subdivided into a further three lithologic units: amphibolite, rusty gneiss and gray gneiss (Dupee et al., 2002). The amphibolite is a dark-green actinolite biotite metavolcanic tuff (Eusden et al., 2006). The gray gneiss is a feldspathic biotite gneiss, and in some places is cut by two-mica pegmatites and granite sills (Eusden et al., 2006). The rusty gneiss is a bedded biotite muscovite gneiss with moderate foliation, with thin 0.5 to 1 meter amphibolite layers throughout (Eusden et al., 2006). All of the above-mentioned lithologic units also contain garnet (Eusden et al., 2006).

Dupee et al. (2002) also mapped two 1-2 meter zones of mylonite within the amphibolite volcanics. Additionally, Dupee et al. (2002) observed an augen gneiss that represents the contact between the Ammonoosucs and the Rangeley-Littleton units. The authors interpreted this to represent the Mahoosuc Fault. Eusden et al. (2006) indicate that kinematic indicators from this augen gneiss show early Acadian normal motion along the Mahoosuc Fault.

1.6d Bretton Woods Granite

The Bretton Woods granite is a pluton belonging to New Hampshire Magmatic Series. It is a two mica (biotite and muscovite), medium-to-fine grained granite. It is white to light-gray in color, and similar in composition overall to the nearby Concord granite (Billings, 1956). It has been determined by monazite microprobe analysis to be late Devonian in age (Larkin and Eusden, 2004).

1.6e Conway Granite

The Conway Granite is part of the White Mountain Magma Series. The rock is a biotite granite, it is pink in color and coarse-grained. The Conway Granite consists of perthitic microcline, quartz, as well as plagioclase and biotite (Henderson et al., 1977; Adams et al., 1962). Near contacts with other lithologic units, the Conway Granite can become porphyritic. In these cases the feldspars become phenocrystic, and maximum size is 0.7 centimeters

(Henderson et al., 1977). Locally, the granite contains vugs, roughly 1 to 3 inches across. These miarolitic cavities often contain quartz, feldspar and other minerals (Henderson et al., 1977). The Conway Granite has been dated several times, with K/Ar ages from 155 ± 4 to 183±5 Ma (Eby et al., 1992).

1.6f Cherry Mountain Syenite

Cherry Mountain rises to 2,500 feet along the western edge of the Mount Dartmouth Quadrangle and belongs to the White Mountain Magma Series (Chapman, 1937). It extends from north to south. The Cherry Mountain syenite intrudes into the Ordovician Oliverian Dome. Chapman (1937) divides the syenite into three lithologic units: main syenite, dark syenite and fine-grained hornblende-biotite syenite. The main syenite itself is sub-porphyritic, and composed of blue-green feldspar, black pyroxene and hornblende (Chapman, 1937). The dark syenite has more mafic minerals, with greater proportions of pyroxene and hornblende as compared to the main syenite unit. The hornblende-biotite syenite is composed of feldspar, hornblende and biotite, but no pyroxene is present (Chapman, 1937). This pluton has not been dated with current techniques, but has been relatively dated to the Jurassic.

1.6g Mafic Dikes

As rift basins formed through faulting and extension of the crust during the breakup of Pangea, the basalt dikes fed the flood basalts and fissure eruptions, filling the rift basins and creating the initial ocean crust (McHone, 2000). However, this hypothesis is still debated. The normal faulting due to Jurassic intraplate deformation have been extended as far as 400 kilometers in towards the North American plate. This deformation is also associated with the observed trends of the basalt dikes (Faure et al., 2006).

The dikes continue for distances of 700 kilometers or more, and maintain their chemical composition along their length (McHone, 2000). McHone (2000) has divided the observed basalt dikes into three major quartz-normative tholeiite subtypes.

The proposed origin of this basaltic magmatism is still controversial, there have been advocates for a single plume-style source, and as many proponents of non-plume magmatism (McHone, 2000, McHone et al., 2005; Beutel et al., 2002; Storey et al., 2001; Puffer, 2001;

Callegaro et al., 2013). Those who oppose plume-style magmatism instead present arguments for a reactivated back-arc source, as a result of eutectic melting due to decompression (Puffer, 2003). McHone (2000) proposed two alternative options, that there was a single, local mantle source for each independent dike or swarm. Alternatively, the mantle source was composed of horizontal layers, which were then individually expressed at the surface by vertically moving magmas to create the dikes (McHone, 2000).

1.7 Extensional Tectonic History

Pangea formed approximately 300 million years ago, and remained in a relatively stable configuration for roughly 100 million years. The supercontinent is hypothesized to have rifted in three major phases, from 210 Ma to 150 Ma. The observed effects of the rifting increase in intensity moving out from the craton towards the ocean (Stewart et al., 1997). The effects of Pangean rifting are most visible in the upper crust, and consist of normal faults, oriented dike swarms, as well as small plutonic complexes (Stewart et al., 1997). Places where extension was localized to the upper crust formed rift basins, which filled with sediment and lava flows (Stewart et al., 1991; Eusden et al., 2010; Olsen, 1997). In particular, Pangean rifting was characterized by regional intraplate deformation and normal faulting (Faure et al., 2006).

The first phase happened around 210 Ma (Early Jurassic), resulting in North America separating from Africa (Figure 2). This created a series of northeast-trending rift basins, the so-called central Atlantic margin (CAM) system (LeTourneau and Olsen, 2003). In some cases, the rifting reactivated previously existing thrust faults from previous orogenies and subsequent crustal thickening during the Paleozoic (LeTourneau and Olsen, 2003). At this point, the young Atlantic Ocean was narrow in some spots due to the non-uniform separation of North America from Africa.

The second phase occurred during the Early Cretaceous (140 Ma), when Gondwana separated into four pieces, again zippering open. This created Africa, South America, India, and Antarctica/Australia (Sears, 2007). The rifting opened the South Atlantic Ocean as South America moved westward from Africa. The third phase began in the Early Cenozoic (65 Ma). During this phase, North America and Greenland separated from Eurasia. At this time, India also collided with Eurasia, causing the Himalayan orogeny.

The extensional features of Pangean rifting most germane to this project are the regional mafic dikes and flood basalts. These are all categorized as part of the Central Atlantic Magmatic Province (CAMP). CAMP is distributed over four continents, on both sides of the Atlantic Ocean (Merle et al., 2014). The age of the basalt dikes have been determined by argon-argon dating to the Triassic-Jurassic boundary, around 200 Ma (Blackburn et al., 2013). However, there is geographic variation in age from Morocco to North America (McHone et al., 2014; Jourdan et al., 2008). These dikes are invaluable as their orientations are indicative of regional trends that directly reflect the paleostress of regional rifting events (McHone, 2000;

McHone and Butler, 1984; Faure et al., 2006; Faure et al., 1996a, Faure et al., 1996b).

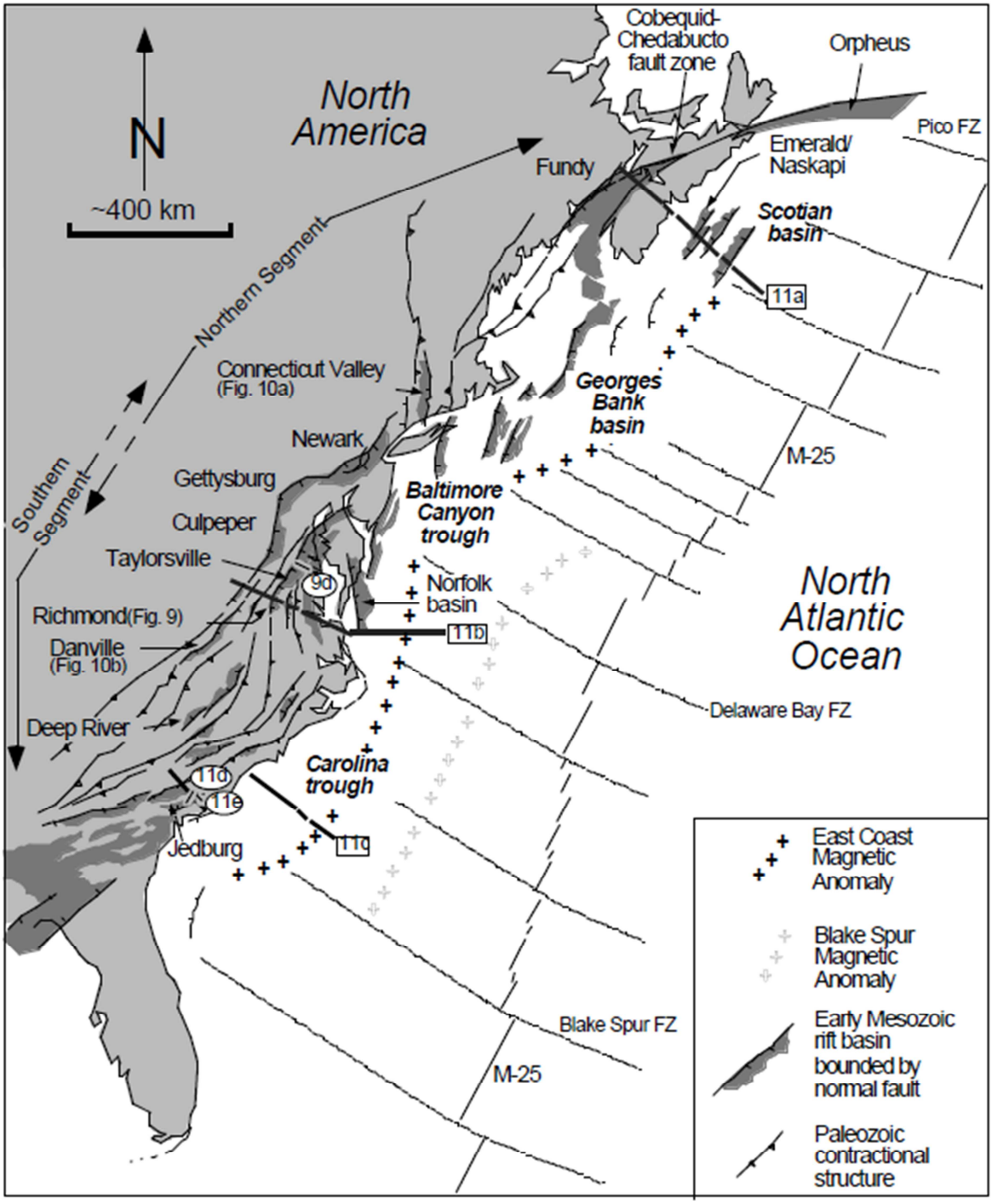

Figure 10: Early Mesozoic rift basins along the coast of eastern North America, along with major tectonic features of the Atlantic Ocean. (Schlische et al., 2004).

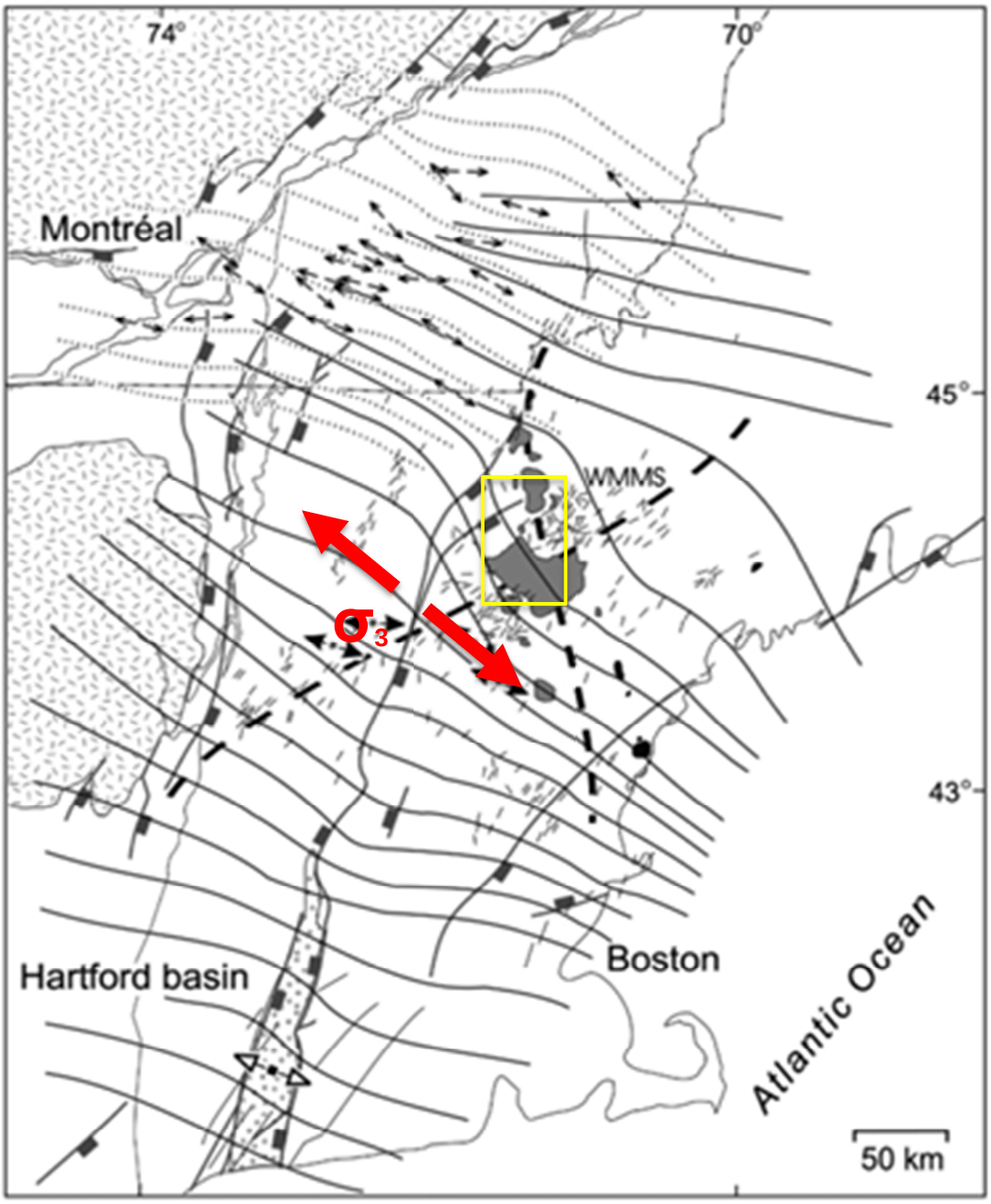

Figure 11: The Early Jurassic paleostress in New England was oriented roughly NW-SE. The red arrows indicate the orientation of least compressive stress. Yellow box indicates rough extent of study area. (Modified from Faure et al., 2006).

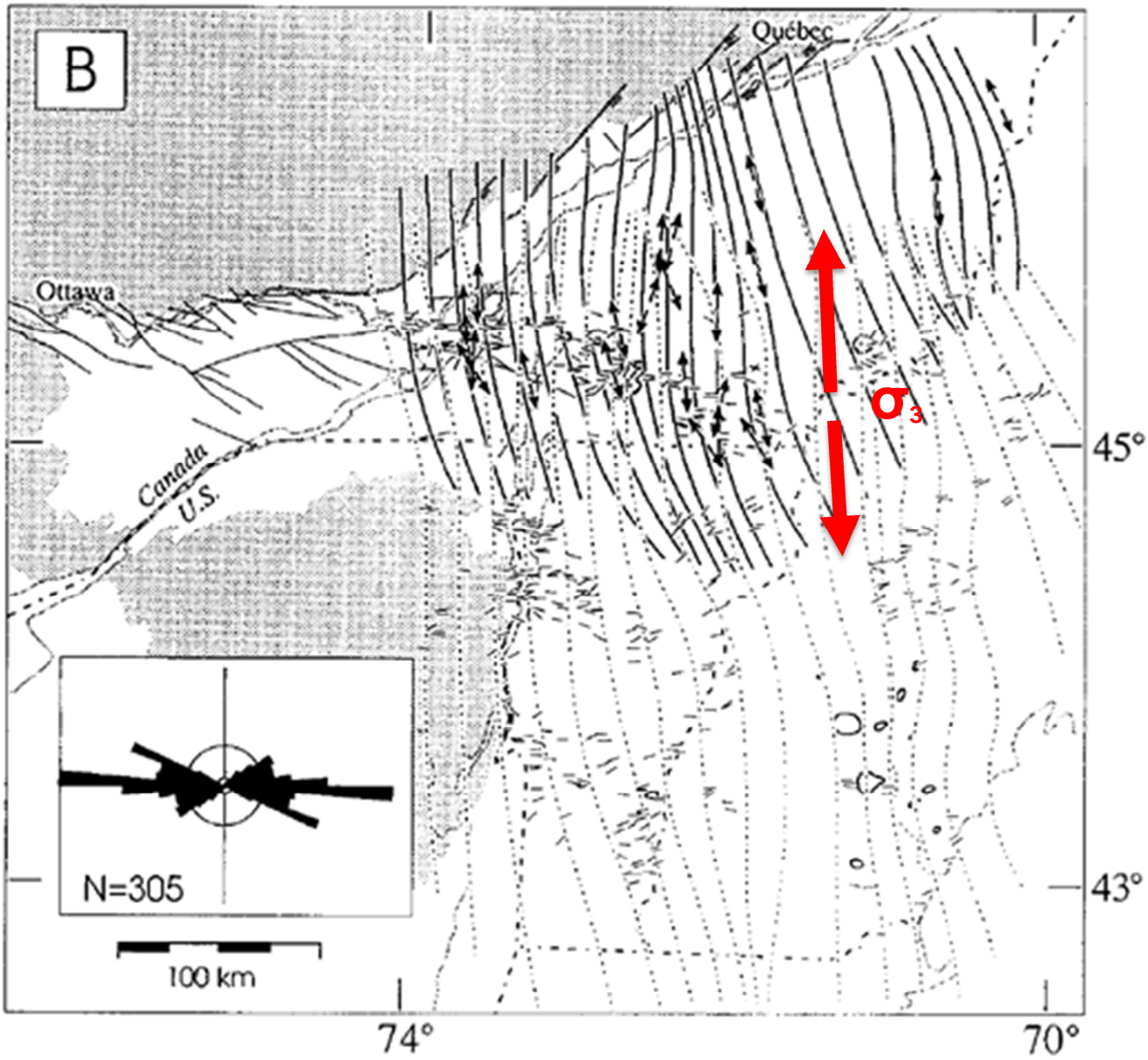

Figure 12: In the mid-Cretaceous, the paleostress shifted to an N-S orientation. Again, the red arrows indicate the approximate orientation of least compressive stress. (Modfifed from Faure et al., 1996b).

1.8 Mesozoic Igneous Provinces

1.8a Central New England Province

The Central New England Province (CNE) extends through New Brunswick to Boston out to the oceanic basin (Figure 4). The majority of the plutons belonging to the Central New England Province are predominantly alkaline in composition, with ages around the Permian-Triassic boundary, approximately 252 Ma (McHone and Butler, 1984; Shen et al., 2011). McHone and Butler (1984) created a map delineating the location of the various igneous provinces within New England (Figure 13).

CNE dolerite dikes are alkaline in composition (McHone et al., 1987; Dorais et al., 2005). The dikes associated with this province are different in composition than the nearby Eastern North American province (ENA) dikes, indicating a unique mantle source for each of these two provinces (Dorais et al., 2005). The ENA and CNE provinces have similar orientations, however the CNE are far more enriched in incompatible elements than the ENA; which has been attributed to the beginnings of the plume-head mantle (McHone et al., 1987; Dorais et al., 2005). Dorais et al. (2005) extrapolated from their major elemental data that the CNE dikes were formed from deeper sources than the ENA dikes. It has been conjectured that the CNE dikes predate CAMP, however no conclusive age dating has been performed to date (Dorais et al., 2005). Figure 14 shows the timeline of the intrusion of these igneous provinces as based on work done by McHone and Butler (1984).

1.8b White Mountain Magma Series

The White Mountain Magma Series (WMMS) is geographically restricted to northern New Hampshire, with a north-south alignment and contains the White Mountain batholith (Figure 8). The WMMS is dominated by syenite and granite, (Eby et al., 1992). These plutons are largely Early Jurassic in age, from approximately 235 Ma (McHone, 1992; Foland and Faul, 1977). The origin of these plutons has been ascribed to melting of the lower crust, as indicated by the contact aureoles surrounding the plutons (McHone, 1992; Eusden et al., 1996b). Other workers proposed that the WMMS is due to the North American plate moving over a hot spot (McHone and Butler, 1984). The Conway Granite and Cherry Mountain Syenite, which are both attributed to the WMMS, are both present in the study area.

1.8c New England-Quebec Province

The New England-Quebec (NEQ) Province begins at the Monteregian Hills in Quebec, and extends southward through Massachusetts, forming an area 300 kilometers by 400 kilometers (Figure 8). These plutons and associated dikes are Early Cretaceous (100-130 Ma) in age, and are bimodal and alkalic, and composed primarily of syenite-gabbro (McHone, 1992; McHone and Butler, 1984). The dikes associated with the NEQ are primarily lamprophyres, with similar compositions to camptonites and monchiquites found in other locations (McHone, 1992). Additionally, they all share chemical similarities, most notably $^{87}Sr/^{86}Sr$ (McHone and Butler, 1984).

The NEQ dikes primarily have an east-west orientation, while the plutons have both an east-west trend as well as a northwest-southwest trend. Both of these orientations reflect the reactivation of east-west rifts, specifically the Ottawa graben and the eastern Adirondack fault system (Faure et al., 1996b; McHone and Butler, 1984). Faure et al. (1996b) attribute these dikes to the rifting of Greenland and Labrador. This presents stronger evidence in favor of magmatic reactivation of basement faults, rather than hot spot related magmatism (Faure et al., 1996b).

1.8d Eastern North American Province

The Eastern North American (ENA) Province are diabase dikes, basalt flows and sills primarily found along the eastern Appalachians (Figure 8). These dikes are quartz-orthopyroxene tholeiitic dikes from the Early Jurassic, around 190 Ma (Dorais et al., 2005; McHone, 1992). Dolerite dikes of this age group have been linked to the basalt flows and sills of the Newark Group, i.e. the Palisades Sill of New Jersey (McHone, 1992).

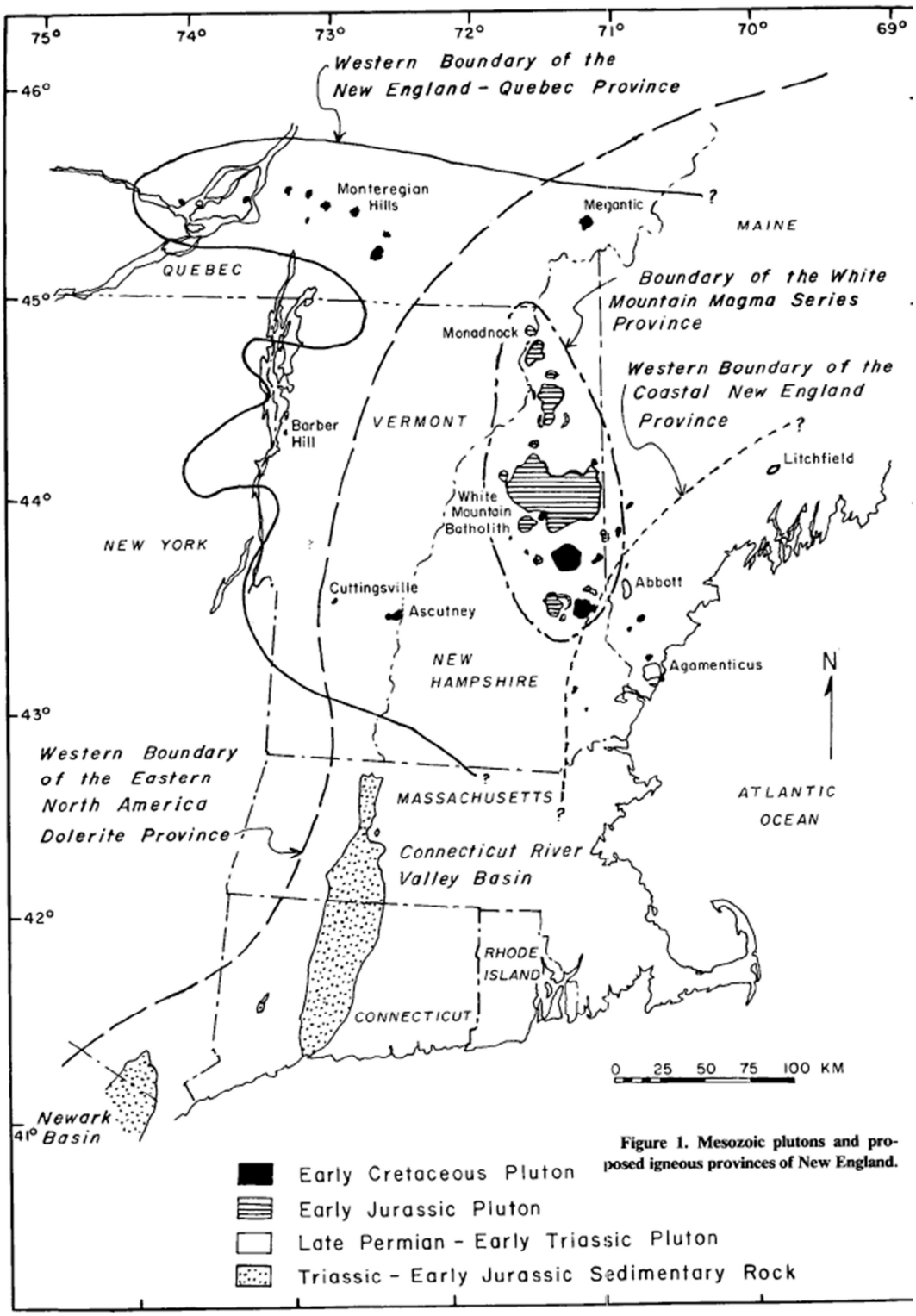

Figure 1. Mesozoic plutons and proposed igneous provinces of New England.

Figure 13: Proposed geographic bounds of the four major igneous provinces in the New England area (McHone and Butler, 1984).

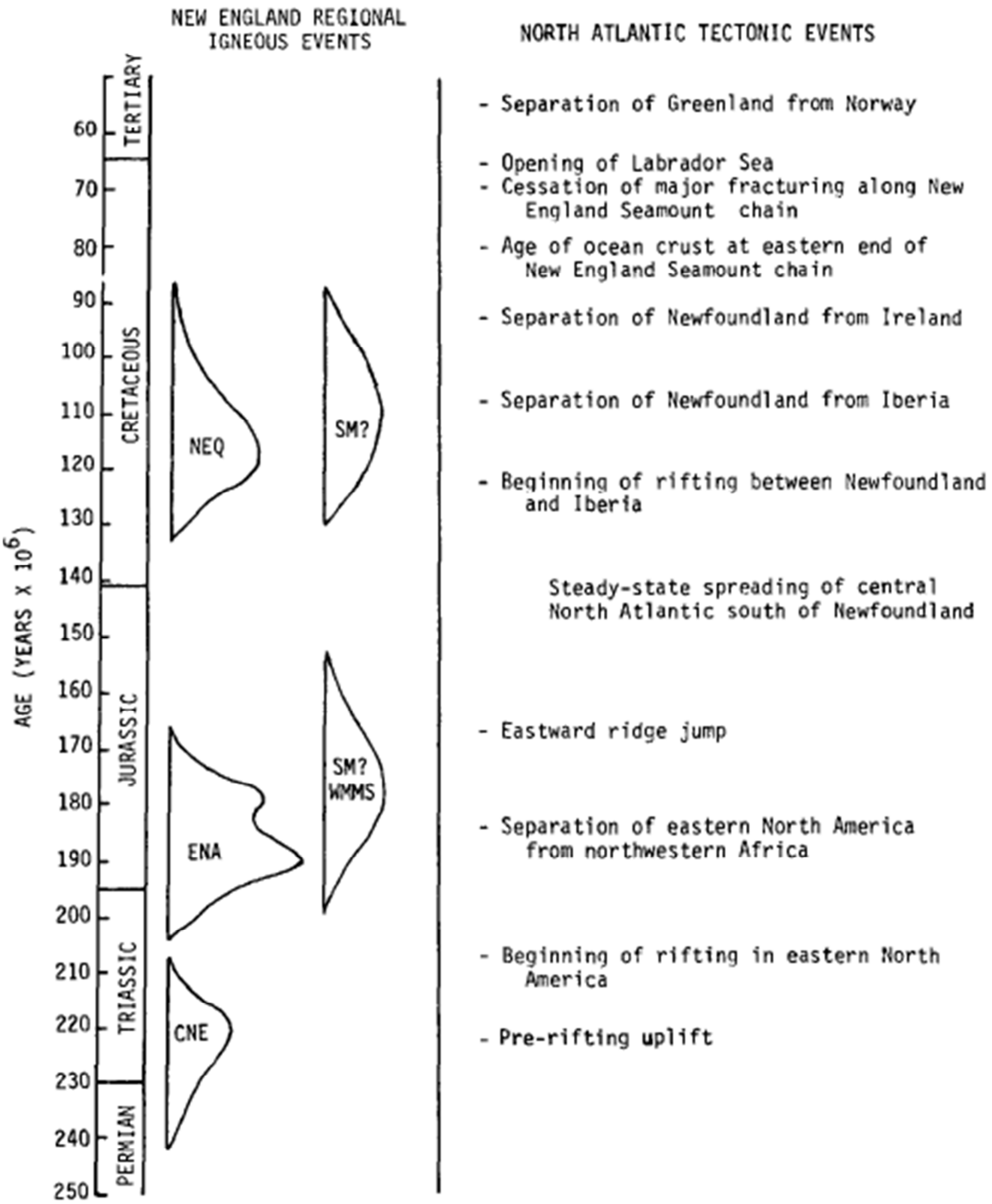

Figure 14: Timeline of formation of igneous provinces with North Atlantic tectonic events (McHone and Butler, 1984).

1.8e Central Atlantic Magmatic Province

The Central Atlantic Magmatic Province (CAMP) extends over several continents: Africa, North America, South America, and parts of Eurasia (Figure 15). The CAMP's age has been shown to be between 202 Ma and 195 Ma (Hames et al., 2000). The CAMP is also dominated by tholeiitic basalts; this uniformity and extent of magmatism hint at "passive" models that concern upper mantle geodynamics (Hames et al., 2003). It has been suggested that CAMP was partially responsible for the Triassic-Jurassic boundary mass extinction (Whiteside et al., 2006; Hames et al., 2003; Palfy and Kocsis, 2014).

Puffer (2003) postulates that the negative Nb anomaly of CAMP basalts indicates a reactivated back-arc source, i.e. that CAMP basalt is from decompression melting of said back arc source. The overall uniform composition of CAMP basalts indicates that the CAMP was efficient in generation and extrusion (Puffer, 2003). The Ordovician Ammonoosuc and Silurian Newbury Formations are also chemically similar to CAMP (Puffer, 2003).

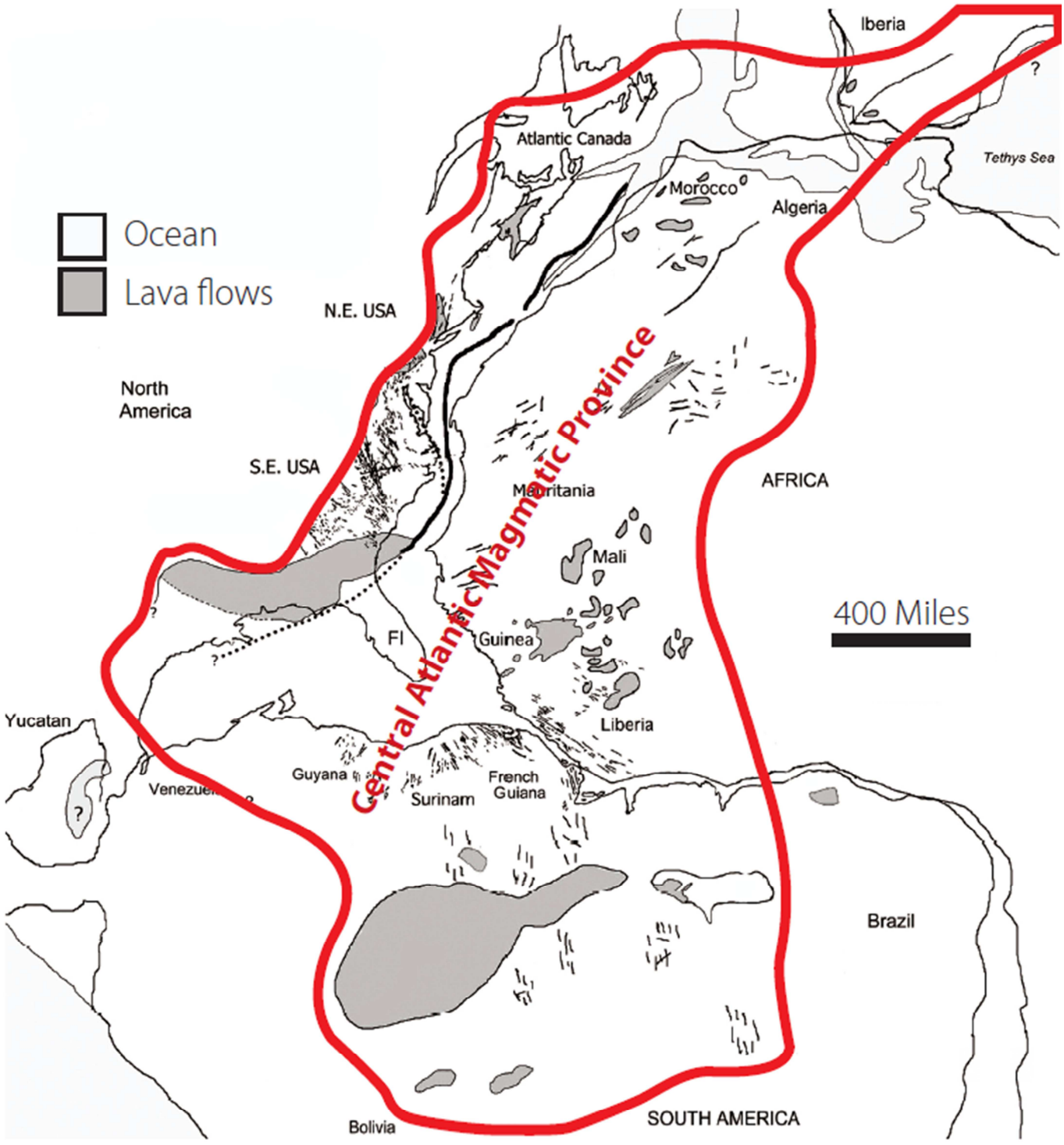

Figure 15: The paleo-extent of the Central Atlantic Magmatic Province as highlighted in red. The CAMP is hypothesized to have been responsible for the Triassic-Jurassic extinction event that paved the way for the rise of the dinosaurs (Eusden et al., 2013).

1.9 Cooling History

Exhumation and cooling history analysis has been done on the Presidential Range. Eusden and Lux (1994) showed late Paleozoic exhumation in the Presidential Range of 0.04 millimeters per year, using $^{40}Ar/^{39}Ar$ mineral ages. As such, the data indicate slow exhumation during the Middle Pennsylvanian through the Early Permian, as well as termination of Acadian uplift circa 305 Ma (Eusden and Lux, 1994). More recent work by Roden-Tice et al. (2011) show a far more variable cooling history using apatite fission-track analysis (Figure 16). More specifically, the data indicated three stages of cooling, from 170-130 Ma, 130-65 Ma, and 65 Ma to present (Roden-Tice et al., 2011). This work was done with the purpose of constraining the timing of the Mesozoic unroofing of the Northern Appalachians. From 152-137 Ma, the exhumation rate was approximately 0.03 millimeters per year, and changed to 0.01 millimeters per year in the window of 137-110 Ma (Roden-Tice et al., 2011). From 110-101 Ma, the unroofing changed to 0.04 millimeters per year.

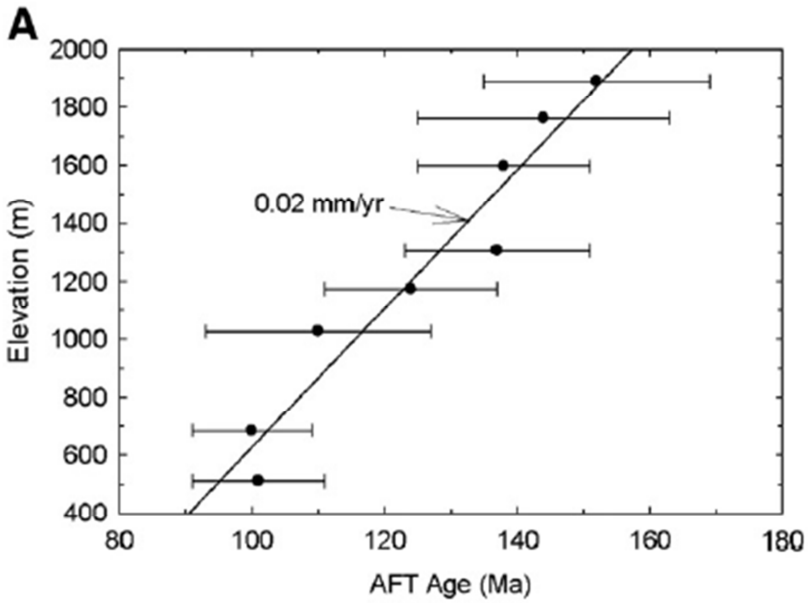

Figure 16: Apatite fission-track (AFT) age plotted against elevation. The samples are from summit to base of Mount Washington. The data presented in this graph show unroofing rates. The data suggest a ~40 °C/k, geothermal gradient (Roden-Tice et al., 2012).

1.10 Mount Dartmouth Quadrangle Study Area

The Mount Dartmouth Quadrangle (part of the White Mountain National Forest) was last mapped in the 1940's by Marland Billings and Katharine Fowler-Billings. The quadrangle itself is immediately to the west of the Presidential Range, but does not benefit from the extensive and well-maintained trail system surrounding the larger mountains of the Presidential Range. The Dartmouth Range stretches east-west in the southeast corner of the quadrangle (Figure 10). The highest peak in the quadrangle is Mount Dartmouth, at 3700 feet (1127 meters). Till blankets most of the area, with few areas of exposed bedrock. Bedrock is primarily exposed where streams and rivers cut down through the till. There is a spectacular exposure of basalt dikes at Mill Brook, beneath Route 115. Occasionally, large outcrops are found in the forest, but there is no particular topographic point at which outcrop is guaranteed to be found.

2. Methods

2.1 Field Methods

Field work was performed over seven weeks from July to August of 2014. The majority of the field work involved bushwhacking, as there are few trails in the Mount Dartmouth quadrangle. Once an outcrop was found, strike and dip were measured, and observations were made depending on presence of certain characteristics, such as foliation, veins, or alignment of mineral grains. All data were recorded twice, once in handheld GPS units made by Trimble Navigation Ltd., and in a standard Rite-in-the-Rain notebook. The Trimbles were pre-loaded with both orthographic and topographic base maps, as well as a data dictionary to record structural measurements and comments on the rock type. The data were later downloaded to a Panasonic Toughbook to archive the data, as well as to analyze in ArcGIS.

2.2 ArcGIS and Digital Mapping

Before use of ArcGIS, the structural data of the basalts were plotted on Mylar using a Brunton baseplate compass. The hand-plotted data included field work data collected by the author and colleagues over the summer in addition to the data previously collected by Fowler-Billings (1944).

The data were imported from the Trimbles and processed through ArcCatalog and ArcMap 10.1. This was done in order to have uniform identifiers so that similar rock types could be selected for ArcMap analysis. The master shapefile was copied and used repeatedly to create the unique rock units, as with field observations and past work done by the Billings. In particular for this study, the structural data of the relevant mafic intrusions were plotted in ArcMap to show the spatial and structural orientation of the dikes in the quadrangle. Using the Properties tab, the basalt locations and orientations were symbolized using strike and dip symbols. The data collected by Fowler-Billings (1944) were also incorporated into the ArcMap, by scanning in the Mylar map.

2.3 Sample Preparation

Eight samples were selected for thin section preparation based on location, mineralogy and orientation of the dikes. These samples were then sliced into thin section size using a template. Because of the size of a few of the samples, the large Diamond Pacific TR-18 Slab saw was used first to reduce the samples to a more manageable size. The smaller Lortone Inc Lapidary Trim Saw Model FS2 (Figure 18) was then used to trim the remaining rock piece to standard thin section dimensions. The samples were sent to Spectrum Petrographics in Vancouver, WA to be made into thin sections. These thin sections are 27x46mm in size. Figure 19 shows the location of the sample sites, along with their sample number.

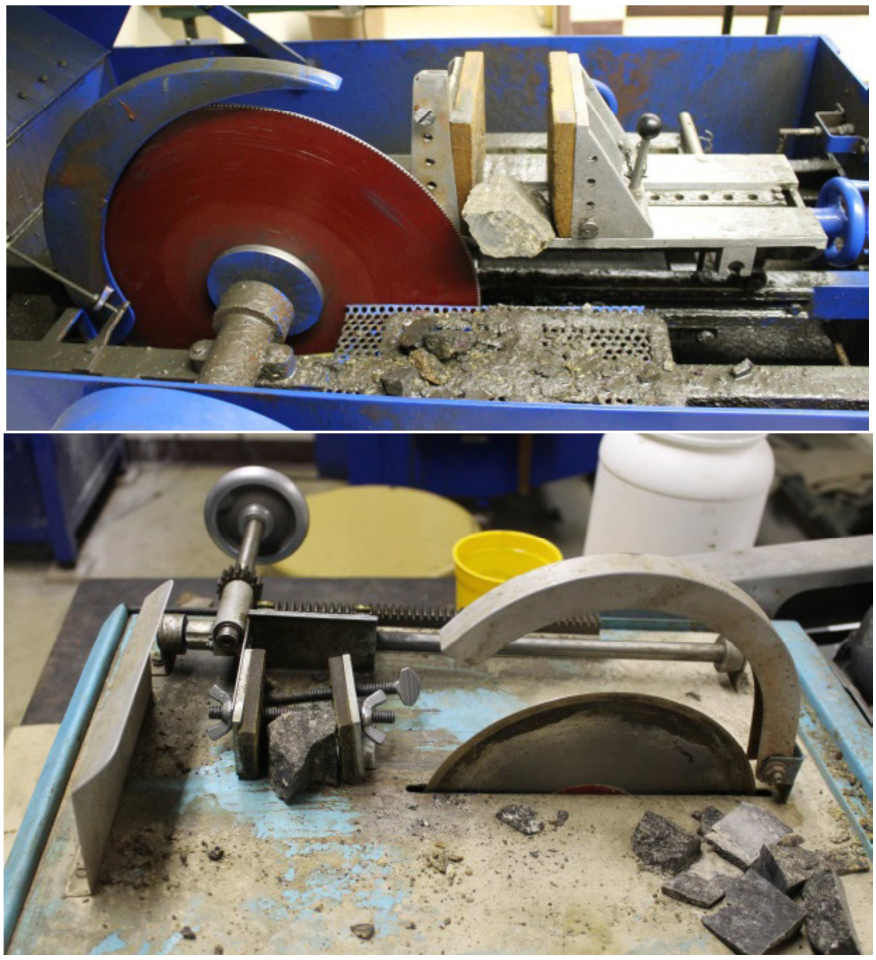

Figure 17: The two rock saws used in preparation of thin sections. The saw on top is the Diamond Pacific TR-18, and the lower picture shows the Lapidary Trim saw. (Images from Choe, 2013).

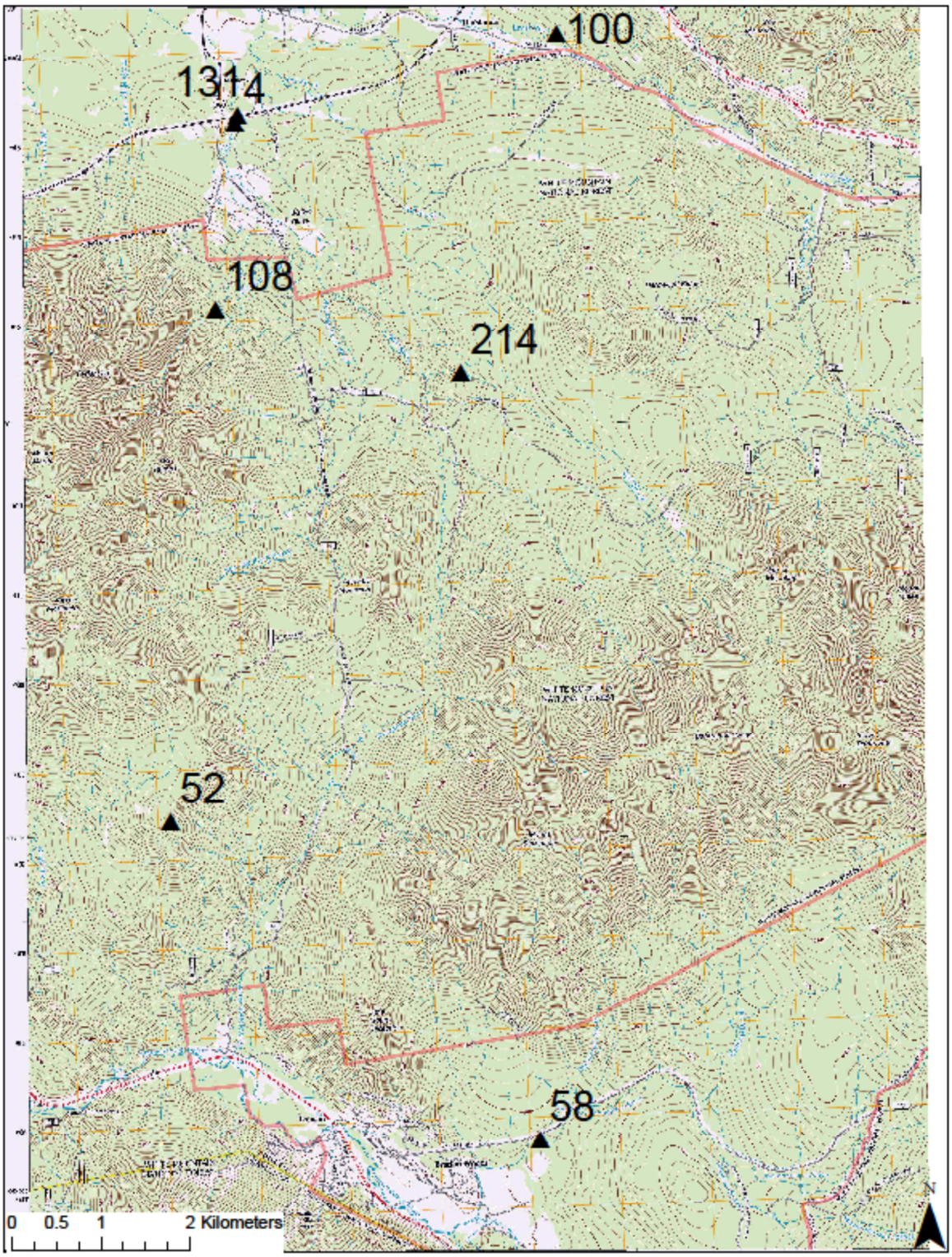

Figure 18: Sample locations shown throughout quadrangle. Samples G4a and G4b are marked by one number. (Topographic basemap from USGS).

2.4 Equal Area Projections

Stereonets were made by exporting data from the ArcGIS file into Excel. The Excel data were then converted into a tab-delimited format to be imported into OSXStereonet, a program written by Nelson Cardozo. This created equal area projections of the planar data. The planes were then plotted as poles to planes in order to make contoured diagrams to make it easier to visually analyze trends in the data.

In cases where there were fewer than 250 data points, the data points were statistically contoured using the 1% area contour method. In the 1% area contour method, the counting circle is constrained to be 1% of the total net area. If there were more than 250 data points, the Kamb method was used. In the Kamb method, the counting circle is variable. It also calculates the number of standard deviations from the uniform distribution of points (Kamb, 1959).

2.5 Rose Plots

Rose plots show only the strike, not the dip, which makes them useful for examining large-scale orientation trends. The data were put into ten-degree bins, and these will be then overlaid on a map of the area. The above-mentioned OSXStereonet program made by Nelson Cardozo was used.

2.6 Transmitted Light Microscopy

Transmitted light microscopy was used to analyze the bulk mineral composition of the samples and textures of the sample. The physics behind cross polarized light are as follows: Light travels isotropically and without polarization from the source, but it is possible to transform non-polarized light into polarized light, which is oriented in a single plane. To be seen by the human eye, a dichroic medium must be used to allow the color or intensity of the light to become visible. In a polarized light microscope, there are two filters, which are oriented perpendicularly to each other (Bradbury et al., 2012). This allows the minerals present in the sample to be identified via differences in the observed birefringence.

2.7 Scanning Electron Microscope/Energy-Dispersive X-Ray Spectroscopy (SEM/EDS)

Bates' JEOL JSM-7100 FLV field emission SEM equipped with Energy Dispersive Spectroscopy (EDS) was used in instances when the identification of the mineral could be done with the polarized light microscope, and to analyze the elemental distribution in the sample. Thin section samples are prepared by first coating them with vaporized carbon, and then the sample edges are taped with aluminum tape to collect excess electrons away from the slide. The thin section is mounted on the stage, which is then inserted into the vacuum lock, which is the chamber immediately before the inner chamber. The vacuum lock, when closed, allows the sample to move into the inner chamber, where the analysis takes place. The electron beam accelerates 20 keV electrons towards the thin section. Three main outcomes occur when the electron beam hits the sample (Dunlap and Adaskaveg, 2001):

1. The beam can go through sample, mass is mostly empty space
2. The beam hits electrons of atoms in sample, creating secondary electrons
3. The beam bounces off nucleus, creating backscatter electrons

When the beam hits electrons present in the sample, the beam knocks an electron out of its shell. This is a secondary electron, is fairly weak in energy (~100 volts). When the electron falls back to its original orbital position, it emits an x-ray characteristic of its element. In the case of backscatter electrons, the incident beam hits the nucleus of the sample atom and "bounces" back. Backscatter electrons have much higher energies. Samples with higher densities will have more of them, so often this can be used to determine the difference in sample densities (Dunlap and Adaskaveg, 2001).

The EDS portion is composed of an electron detector, which has a 10keV positive potential on its face that attracts the secondary electrons. There is another detector that picks up the backscatter electrons. The "counts" of the element are recorded based on how many X-rays are detected crossing the potential. The computer then identifies the correct elements based on the well-known differences in orbitals.

Figure 19: Bates' JEOL JSM-7100FLV Field Emission Scanning Microscope in the Carnegie Science Hall Basement (Image from Bates Biology Website: http://www.bates.edu/biology/).

2.8 X-Ray Fluorescence (XRF)

Nine samples for XRF were prepared to be analyzed with the XRF machine at University of Maine at Farmington, which is run by Professor David Gibson. Before samples can be run through the XRF, they must be crushed to a uniform grain size. This was done at Bates using a Spex-Mill table-top grinder. The container was pre-contaminated with sample before each use, and rinsed with ethanol after each use. The sample fusion requires 5.5g (+/- 0.0002) of lithium meta-tetrabarate flux mixed with 0.5g (+/- 0.0002) of sample, which is then mixed and put into platinum-gold crucibles. The Automated Fusion Technology Phoenix machine heats these crucibles to 1030°C. Before the melt is poured onto pre-heated molds, the melt is mixed with ammonium iodide tablets to prevent sticking. The crucibles are acid washed in between fusions.

The rare earth element sample preparation was done with the pellet method. 7.4 grams of sample was mixed with 1.4 grams of a paraffin-based binder. These mixtures were then

placed into a metal die set consisting of a base plate, polished pellet dies, and a plunger. This is then placed in the hydraulic press for five minutes under 11 tons of pressure.

The samples were analyzed for major, minor, trace, and rare earth elements using the Bruker S4 Pioneer XRFS. The rare earths analyzed are lanthanum, cesium, neodymium, samarium, and europium. The Bruker S4 Pioneer uses WD-XRF methodology with SpectraPlus software.

Figure 20: The Bruker Automated Fusion Phoenix machine in action (Image from Oxman, 2014).

Though in principle XRF works similarly to the SEM, XRF returns bulk rock chemistry as opposed to the small area analyses that the SEM can return. In XRF, the sample is bombarded with short wavelength radiation (x-rays), and the electrons become ionized. The

radiation elevates an inner electron to a higher energy state, which then eventually decays back to its original state. When this decay happens, energy in the form of radiation is emitted, which is termed fluorescent radiation. This energy is characteristic of specific electron orbitals in a specific element, and can therefore be used to determine the abundance of the elements in the sample.

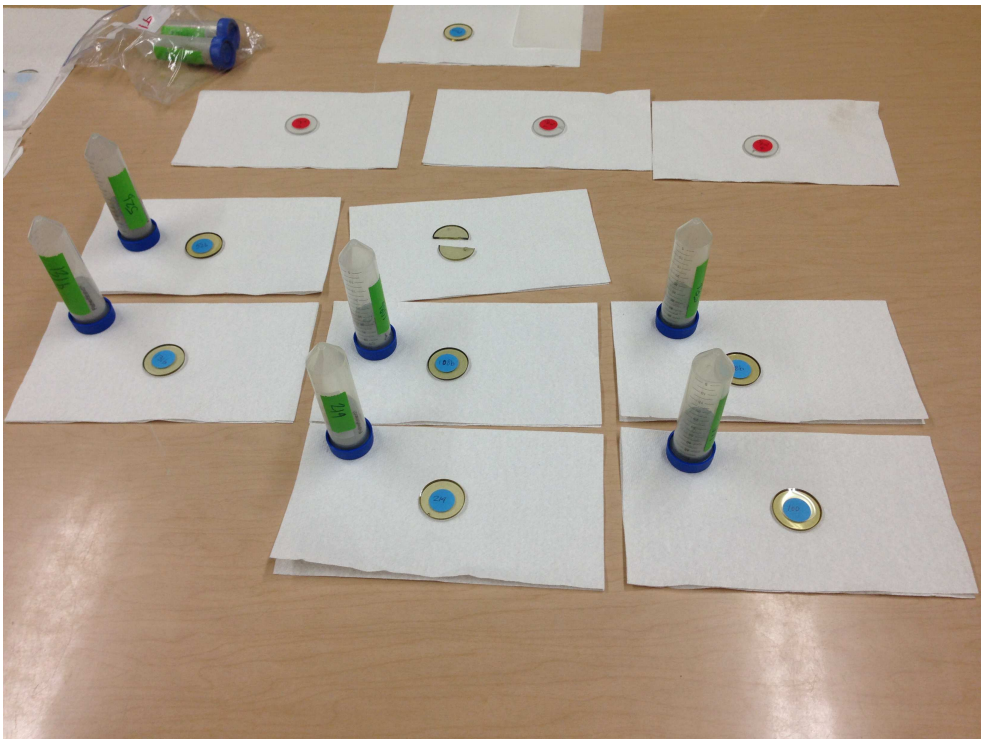

Figure 21: Fused samples prior to use in XRF machine. The broken sample in the back row was discarded. (Image by Oxman, 2014).

3. Results

A combination of field work, brittle structural analysis, optical/scanning electron microscopy (SEM), and X-ray fluorescence (XRF) analysis was performed on samples gathered from the Mount Dartmouth Quadrangle. Field work revealed a 100 meter wide, 7.8 kilometer long dike zone containing multiple mafic dikes that are exceptionally well exposed in Mill Brook at the junction of NH Rt. 115 and the Cherry Mountain road. Brittle structural analysis indicates the presence of four systematic fracture sets found throughout the quadrangle. In particular, brittle structural analysis was focused on two areas in the study quad that had the greatest exposure, at Upper Falls along the Ammonoosuc River, and underneath the Mill Brook Bridge. Thin sections were made of collected mafic samples, and analyzed using both optical and scanning electron microscopy, equipped with energy dispersive spectrophotometry. XRF analyses were also performed on all samples.

3.1 Field Work and GIS Maps

The average orientation of the newly named Mill Brook Dike Zone (MBDZ) is N-S and steeply dipping (Figure 23). Within the zone, the strike and dip of dikes ranges from: 207, 63°SE, to 178, 79°W, to 5, 69°E. In the quadrangle, there are two areas that have excellent outcrop exposure, one at the aforementioned brook, and the second at the Upper Falls of the Ammonoosuc River just off the Base Station road near Bretton Woods. At the field location beneath the Mill Brook Bridge, the outcrop shows dike-within-dike injections.

The largest observed dike in the zone (sample 133) is approximately 25 meters in width, comparable in size to the largest dikes mapped in the Northeast, for example the Christmas Cove dike or the Higganum dike (McHone, 2014). The observed chilled margins were approximately 3-5 centimeters in width, while the core of the dike contained 1-3 centimeter subhedral plagioclase grains, creating a porphyritic texture (Figures 26 and 27). The Mill Brook Dike Zone cuts through the Jurassic Cherry Mountain syenite pluton along the western edge of the quadrangle, but was not observed to crosscut the Jurassic Conway granite in the south of the quadrangle (Figure 23).

Three other large dikes were found at the intersection of the Cherry Mountain highway and Rt. 115. All three had similar textures to the 25-meter dike mentioned above. The second largest one, sample 131, was 20 meters wide and strikes NE-SW. The third largest is sample 273, and it is 15 meters wide striking NW-SE. The last dike is sample 134, and it is 10 meters wide and strikes to the NE-SW. Figure 24 shows the spatial relationship of these four dikes found at Mill Brook. All show chill margins, and coarse, phenocrystic plagioclase cores.

Two other large dikes were found in the quad. A 20-meter wide dike was found in Streator Brook, on the northwestern flank of Cherry Mountain. Another 15 meter wide dike was found along the ridge, near the Humps of Cherry Mountain (Figure 23). The southerly connection of the MBDZ was found along the foothills of Cherry Mountain (Figure 23; Figure 28).

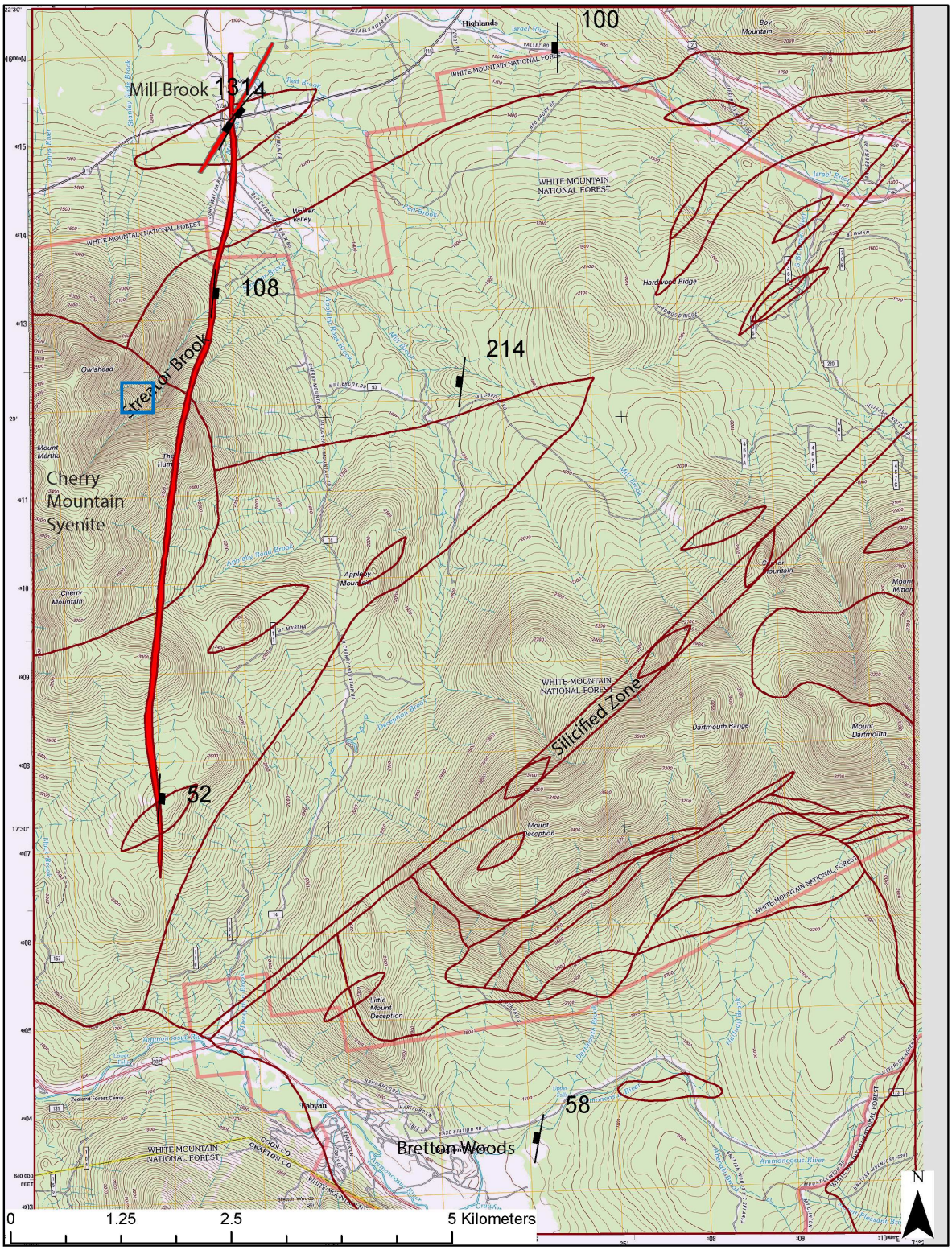
Mill Brook
314
100
108
214
52
58
Streator Brook
Cherry
Mountain
Syenite
Silicified Zone
Bretton Woods
Highlands
WHITE MOUNTAIN NATIONAL FOREST
Hardwood Ridge
Dartmouth Range
Mount Deception
Mount Dartmouth
Mount Martha
Owlshead
Cherry Mountain
Appleby Mountain
Boy Mountain
Mount Mitten
Little Mount Deception
Jefferson Notch Road
Base Station Road
Bretton Woods
Crawford Path
Ammonoosuc River
Israel River
Mill Brook
Red Brook
Dartmouth Brook
Halfway Brook
Appleby Road Brook
Darby Field
Mount Clinton
Mount Pleasant
Mount Eisenhower
Mount Monroe
Mount Washington
Mount Jefferson
Mount Adams
Mount Madison
Mount Isolation
Mount Resolution
Mount Parnassus
Mount Hope
Mount Cabot
Mount Waumbek
Mount Starr King
Mount Weeks
Mount Cleveland
Mount Moosilauke
Mount Lafayette
Mount Lincoln
Mount Liberty
Mount Flume
Mount Osceola
Mount Tecumseh
Mount Kinsman
Mount Wolf
Mount Field
Mount Willard
Mount Avalon
Mount Crawford

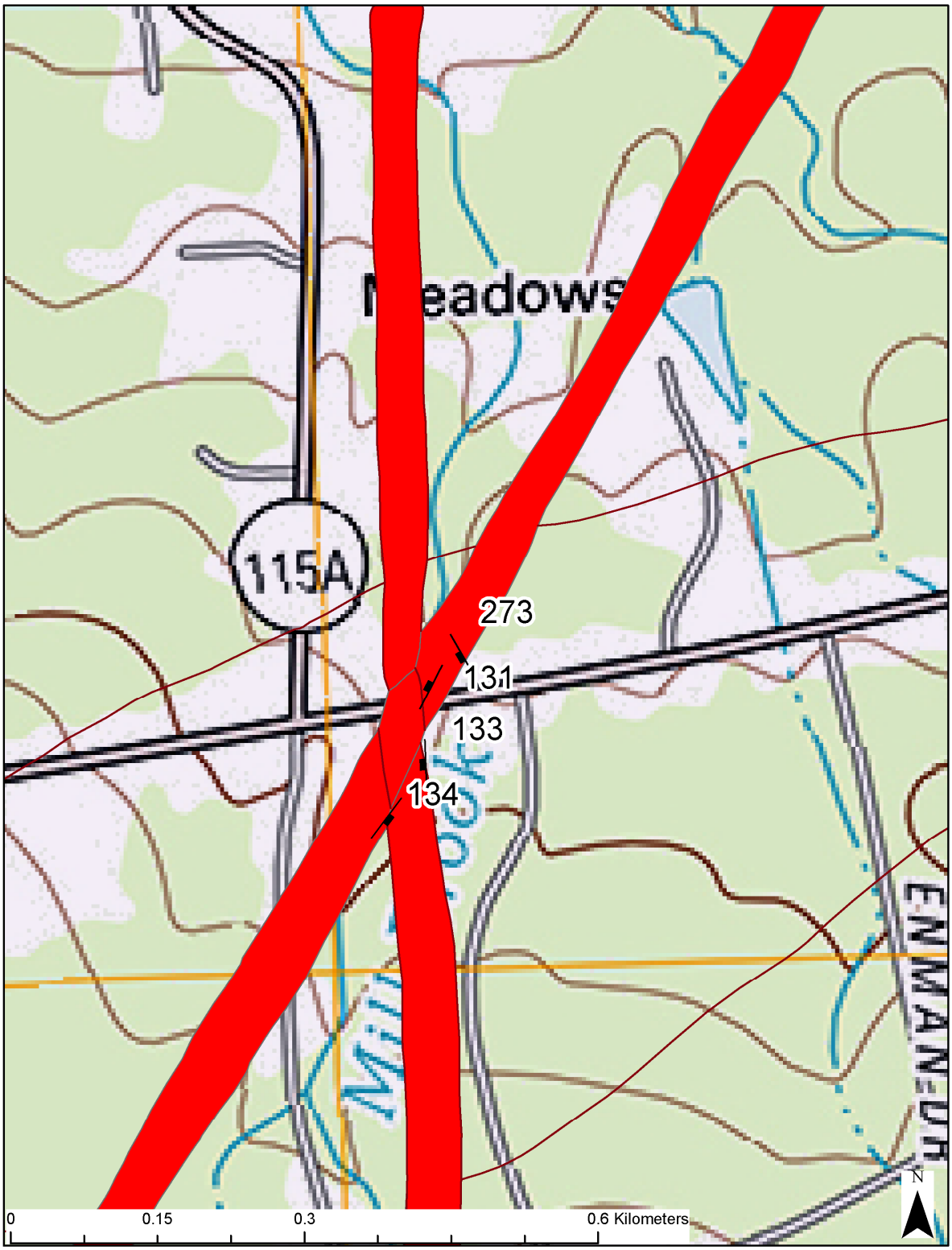

Figure 23: Detail of Millbrook area, showing geometric relationship between the four major dikes underneath the Millbrook Bridge. In order from largest to smallest, sample 133 is 25 meters wide, sample 131 is 20 meters wide, sample 273 is 15 meters wide and the smallest is sample 134 at 10 meters wide. The thickness of the red line corresponds to the width of the dike, these thicknesses are to scale with the rest of the map. (Topographic basemap from USGS).

Figure 24: Area beneath Millbrook Bridge, looking downstream (south). The large dike visible is sample 133, the extent of the width is indicated by the red lines. The dotted white lines show dike injection. (Image by Oxman, 2014).

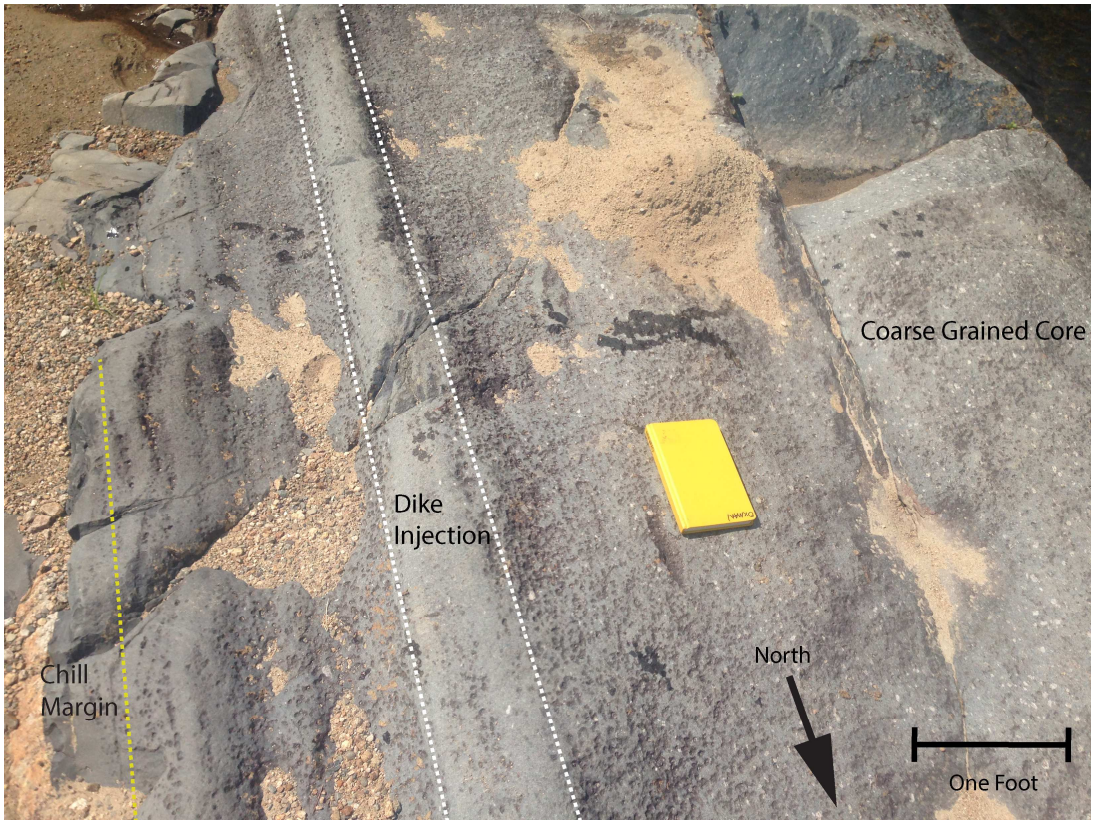

Figure 25: Eastern side of dike observed downstream of Mill Brook Bridge. Dike injection as seen in above Figure is highlighted in white. The chilled margin is distinct, on the left, and grades into the coarse grained core to the right. (Image from Oxman, 2014).

Figure 26: Coarse-grained core of dike. Rock hammer for scale. (Image from Eusden, 2014).

Figure 27: Outcrop (sample 52) that forms southern connection of Mill Brook Dike Zone. (Image from Eusden, 2014).

3.2 Synoptic Equal Area Projections of Joints and Dikes

A study of the joints was performed to evaluate the relationships between the basalts and observed fractures. This was done in order to subsequently place this data in its paleostress context. Regional joint data was collected from the entire quadrangle, while two detailed joint data sets were collected from the Mill Brook area and the Upper Falls of the Ammonoosuc River.

The regional data set shows four systematic joints sets observed throughout the quadrangle, though some areas are more dominated by a particular joint set than others. The relative ages of the sets were determined by cross-cutting relationships seen in the field. The oldest set, which strikes NE-SW (57°, 85°SE), is the dominant set in the quadrangle. The next youngest set is NW-SE striking (130°, 67°SW), and older in age than the third N-S striking set (163°, 85°W). There is also a sub-horizontal sheeted joint set (224°, 0-15°), which was found throughout the quadrangle. The sheeted joints were not measured as part of the regional study but were measured for the two detailed studies.

Synoptic plots for the regional data set, when divided into two groups by joint strike and dip, and dike strike and dip, show separate trends. These equal area projections do not include the strike and dip data collected at Upper Falls or Mill Brook. This was done so that the synoptic plots were not overwhelmed and unduly influenced by these data.

The dike plot (Figure 29) shows N-S, NE-SW and NW-SE strikes. The joint plot (Figure 30) shows a NE-SW strike as well as an approximately NNW-SSE strike. When this data is plotted together (Figure 31), the most visible strikes are those of the dike set, N-S, NE-SW and NW-SE.

The combined dike and joint synoptic plots show the strikes observed in the synoptic dike plot, with the N-S, NE-SW and NW-SE strikes. The strikes visible in the synoptic joint plot are not visible in the combined synoptic plot. The synoptic plot (Figure 31) shows the NE-SW oriented fractures overwhelming the signal of the NW-SE oriented dikes.

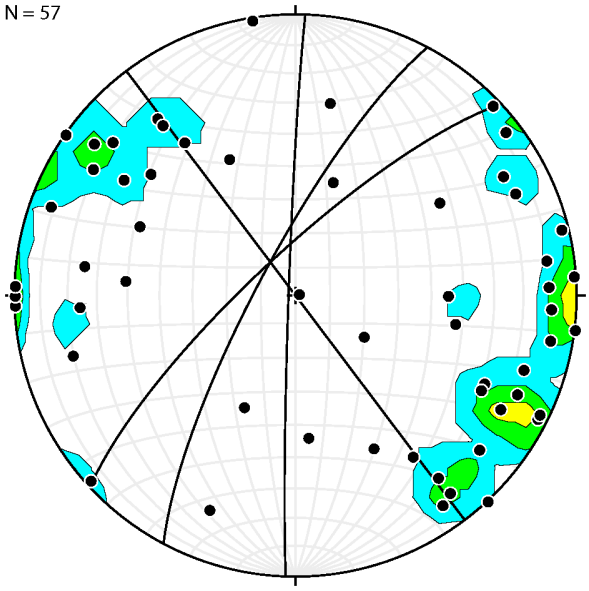

Figure 28: Synoptic plot of dike data in quad.

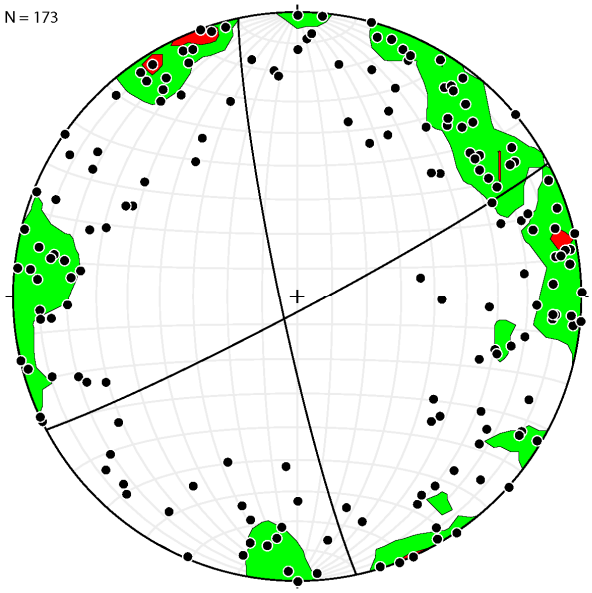

Figure 29: Synoptic plot of joints in quad.

Cross cutting relationships were determined using observations from the field. Figures 32 and 34 show the area in Mill Brook north of (i.e. downstream from) the intersection of Rt. 115 and the Cherry Mountain highway. As shown on the Figures, the N-S striking fractures (shown by yellow lines) are cut by E-W striking fractures (shown by orange lines). The NW-SE

fractures (shown by blue lines) are cut by NE-SW fractures (shown by red lines). In one spot in the photograph, it appears that the NE-SW fractures cut across the N-S fractures.

This indicates that the NE-SW fractures are youngest of all the observed fractures. However, it is not possible to determine from the field photos the age relationship between the

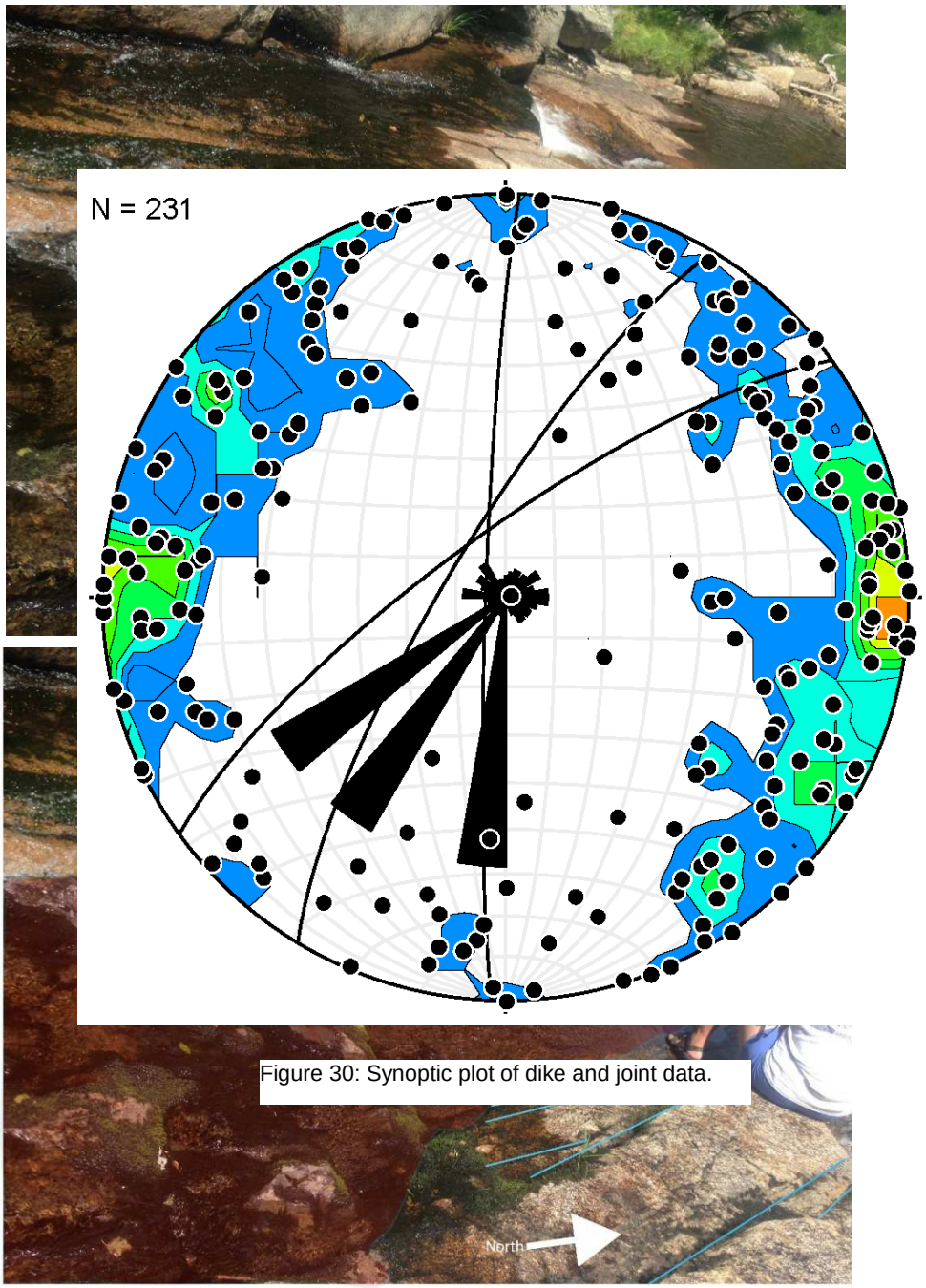

Figure 30: Synoptic plot of dike and joint data.

E-W fractures and NW-SE fractures. The E-W fractures are younger than the N-S fractures, while the NE-SW fractures are younger than the NW-SE fractures, as observed from field photos.

Figure 31: The upper photo shows the field image of the area below the Mill Brook Bridge. The second image shows the annotations indicating crosscutting relationships. The red polygon shows the extent of the mafic dike, which is the NW-SE oriented arm of the intrusion located downstream of the Mill Brook bridge. The orange line shows the E-W fractures, yellow line shows N-S fractures, blue line shows NW-SE fractures and red line shows NE-SW fractures. Geologist in corner is Sarah Xiao, for scale. (Image from Oxman, 2014).

At the Upper Falls of the Ammonoosuc River, N-S striking fractures are cut by sheeted joints, showing that the sheet joints are younger than the N-S striking fractures (Figure 34).

Figure 32: Slickenlines observed at Upper Falls, north arrow is oriented. (Image from Oxman, 2014).

Figure 33: Photograph of the Upper Falls of the Ammonoosuc River looking south across the river. The N-S fractures are shown by yellow lines and are cut by the sheeted joints shown by purple lines. This region had one exposure of dip-slip slickelines on the sheeted joints shown by purple lines. This region had one exposure of dip-slip slickelines on the steeply dipping joint surfaces, see Figure 33 above. (Image from Oxman, 2014).

3.3 Upper Falls and Mill Brook Equal Area Projections

The equal area projection for Upper Falls (Figure 36) shows three joint sets, NW-SE, NE-SW and sheeted joints. The Mill Brook equal area projection (Figure 35) has two joint sets, NE-SW, and approximately N-S. The rose plots indicate a significant preponderance of the NE-SW joints, as well as the approximately N-S joints.

The NE-SW set is ubiquitous throughout the study area, and represents the youngest fracture set in the study area. In the field, these joints showed no offset and only rare slickenlines (Figure 33). The NW-SE set is also ubiquitous throughout the quadrangle, and predates the NE-SW set. The orientation of these joints differs between Mill Brook and Upper Falls. At Upper Falls, the joint set is oriented 130°, 67°SW. The Mill Brook joint set is oriented 333°, 80°NE.

A regional, dike-parallel N-S, steeply dipping joint set was also discovered in the regional data and the Mill Brook data but not in the Upper Falls data. Sub-horizontal joints were observed throughout the quadrangle, with a dip of approximately 0-15°. The best exposure of these joints is at Upper Falls (Figure 34). The E-W fractures are younger than the N-S fractures.

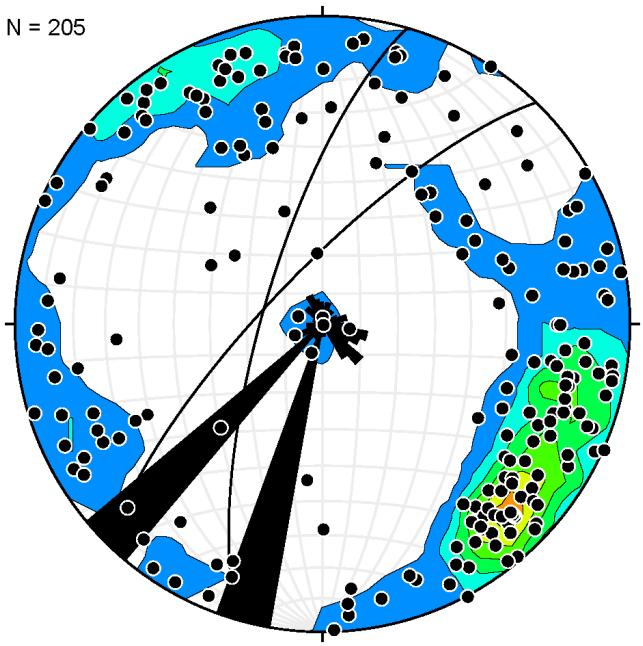

Figure 35: Mill Brook equal area plot showing dike and joint data. Left hand NE-SE striking average is 196, dipping 74. Right hand NE-SW striking average is 224, dipping 76. The rose plots show that the preponderance of joints have NE and NS orientations.

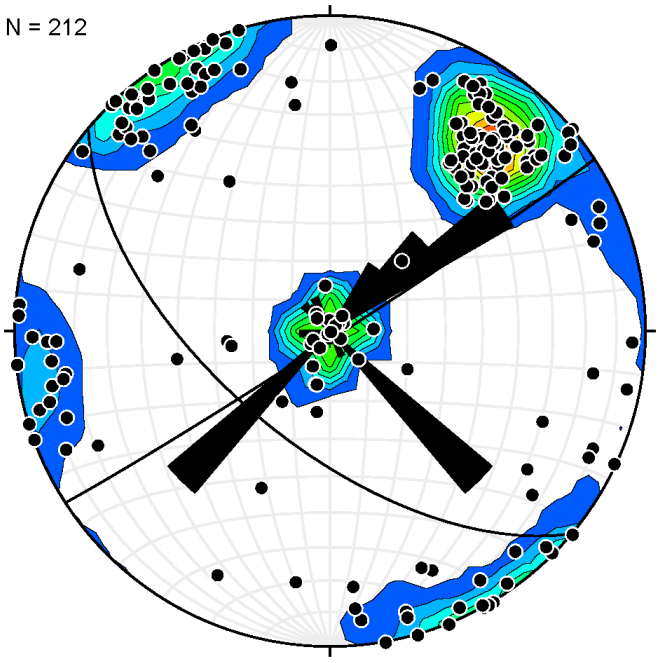

Figure 34: Upper Falls equal area plot showing dike and joint data. NW-SE striking average is 130, dipping 61. NE-SW striking average is 58, dipping 88. Rose plot diagram shows the NW trend of individual fractures.

3.4 Thin Section Results

Hand Sample and Optical Microscopy Observations

A thin section analysis was performed on eight samples from throughout the quadrangle to better understand the petrologic history of the dikes in the quad. Samples G4A, G4B, 131B and 214 are from the Mill Brook location. Sample 52B is from the south end of the Cherry Mountain, while sample 58B is from the Ammonoosuc River, nearby to Deadman's Gorge. Sample 108B is from Streator Brook, which runs off the northeastern flank of Cherry Mountain. See Figure 19 in the Methods chapter for locations of the samples.

Overview of the Thin Sections

The mineralogy of the basalts is typical, with lath-like plagioclase feldspars, often of two different sizes (groundmass and phenocrysts), sub-to-euhedral pyroxene phenocrysts, and opaques such as magnetite, ilmenite, and wurtzite (as determined by thin section work and SEM/EDS). There is notable alteration of the primary pyroxene and plagioclase mineral phases in the basalts throughout all of the samples. This is manifest by sericite, chlorite, and amphibole alteration products. In the majority of the samples, the plagioclase crystals are less altered than the other grains. In samples 131B, G4A, and G4B, there is a significant evidence of cataclasis of the grains manifested by broken grains along through going fractures.

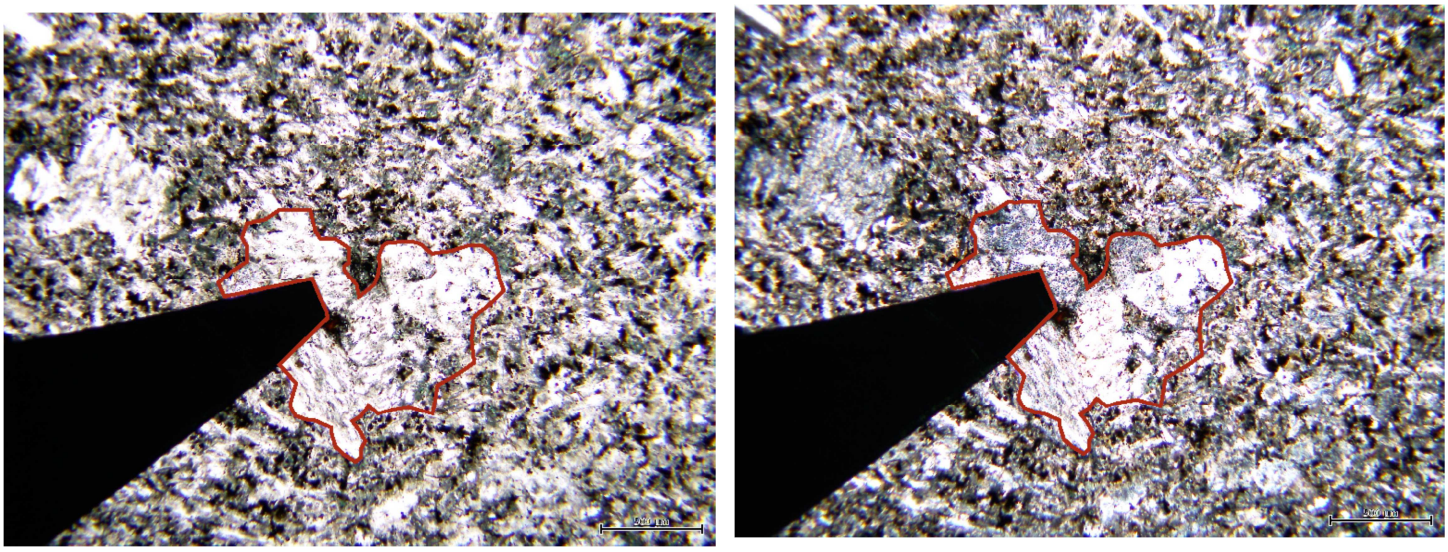

Figure 37: Optical photo showing sample 214. The microphotograph on the left shows the sample in plane polarized light, while the one on the right is in cross polarized light. The red line highlights the altered area of interest that was examined with the SEM/EDS. In particular, the analysis focused on the opaque grain to the right of the arrow.

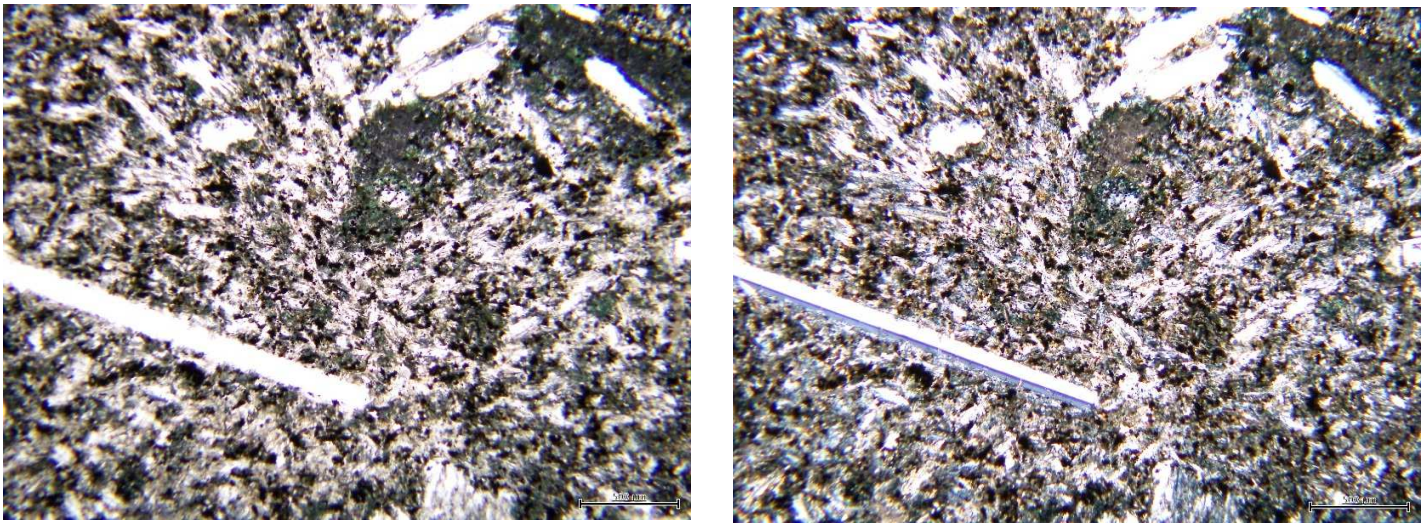

Figure 36: Sample 214. The microphotograph on the left is PPL, the right is XPL. The overall texture is shown, along with an unaltered phenocrystic, plagioclase lath in the lower left.

Sample 214 in hand sample is fine grained, and dark brown to dark gray/black. Feldspar grains were visible in hand sample, roughly 1 centimeter across in width. In thin section, the feldspars show plagioclase-type twinning and the grains are lath shaped (Figure 38). There is alteration of the grains throughout the sample, primarily sericite and chlorite (green) alteration. The areas of alteration of the larger grains are small, relative to the other samples from the study site. The plagioclase grains appear to not be as altered, however, throughout the

sample. Plagioclase composes 50% of the sample, chlorite composes 30%, and opaque minerals compose 20% of the sample. The opaques are small and angular. No fabric is visible in the sample. The red outlined area in Figure 31 shows the area analyzed with the SEM/EDS.

Sample 108B, in hand sample, is fine grained and dark gray to black. This sample is from approximately the middle of the 30-meter wide dike in Streator Brook. Small feldspar

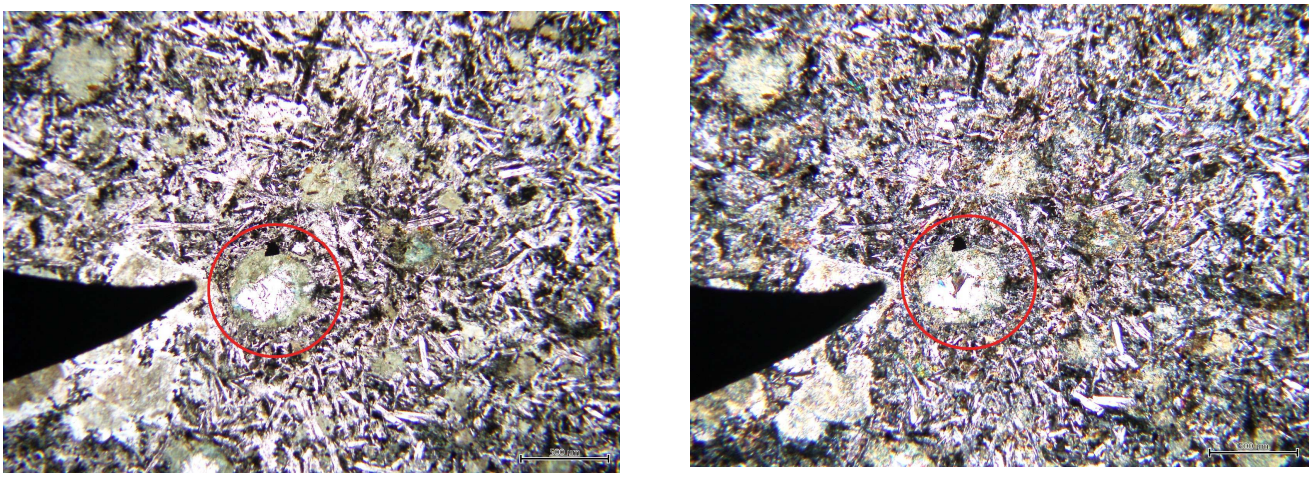

crystals are visible in hand sample, approximately 0.25 centimeters long. In thin section, the

Figure 38: 10x magnified image of altered grain shown above in Figure 39. Sample 108B, image on left is PPL, the image on right is XPL. The red circle highlights an altered grain of pyroxene, surrounded by a rim of amphibole. The overall texture of the samples is similar to what is seen above, with altered grains interspersed throughout a matrix composed of opaques and plagioclase laths.

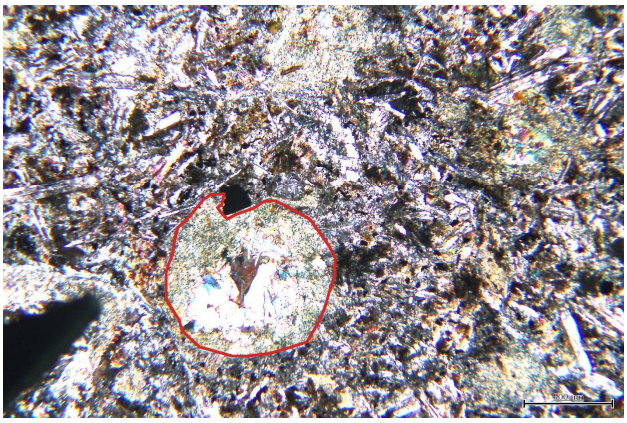

feldspars appear as laths, and show plagioclase-type twinning (Figure 39). The plagioclase in

Figure 39: 10x magnified image of altered grain shown above in Figure 39.

this sample is also less altered. The opaque minerals are small and angular. Altered grains in the sample show pyroxene in the core, surrounded by a rim of amphibole. The sample is

composed of 60% plagioclase, 30% altered grains, and the remaining 10% are opaques. There is no visible fabric in the thin section.

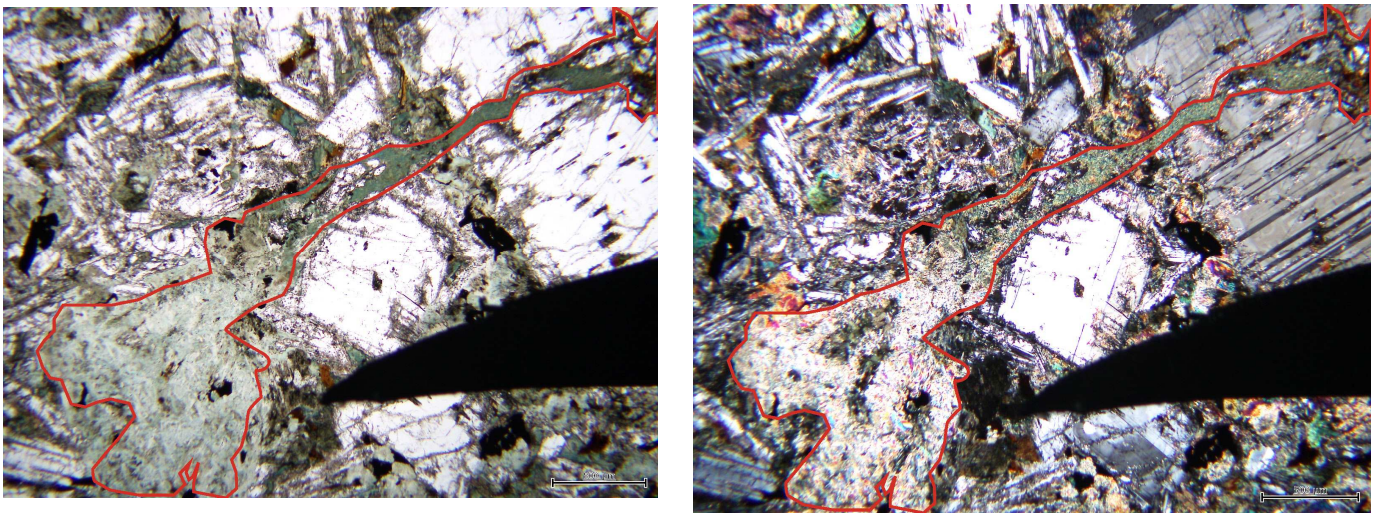

Figure 40: Sample 131B, image on left is PPL, image on right is XPL. The red line shows the extent of one area of cataclasis, as well as the extensive alteration present throughout the sample.

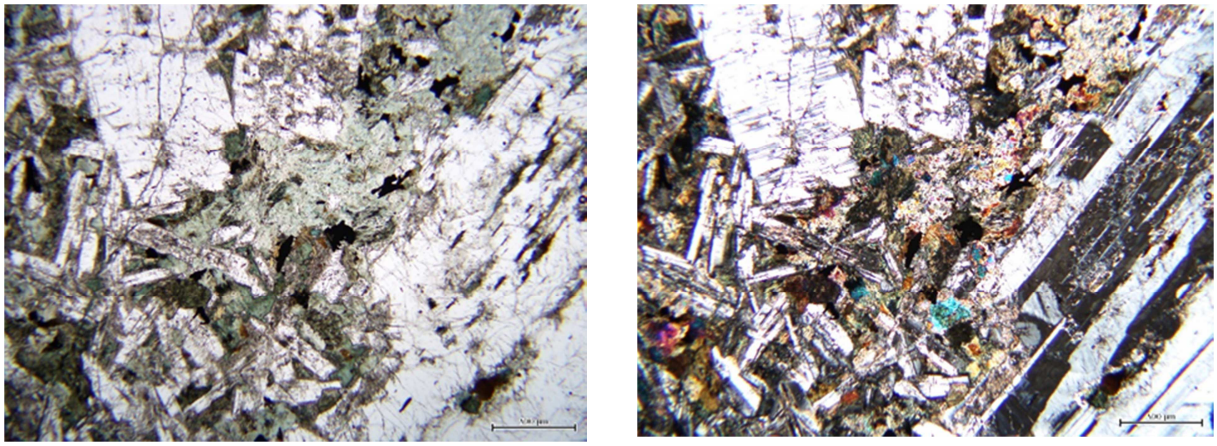

Figure 41: Sample 131b, showing overall texture of samples in PPL (left) and XPL (right).

Sample 131B had a porphyritic texture in hand sample from the core of the Mill Brook exposure of the dike. Large subhedral feldspar crystals in a dark gray groundmass composed of finer-grained plagioclase laths, opaques, and alteration products are apparent. The

feldspars show polysynthetic twinning in thin section, along with medium-sized, anhedral ilmenite grains. There are inclusions within the plagioclase crystals. The plagioclase crystals also show zoning. The grains in this sample show extensive cataclasis (Fig 41, red outlined region). Throughout the sample there is pronounced alteration of all the grains, including the plagioclase. Primarily plagioclase has been altered to sericite, and pyroxene has been altered to amphibole and biotite. Plagioclase composes 70% of the sample, with the remainder composed of 10% opaques and 20% hornblende/biotite altered pyroxene grains.

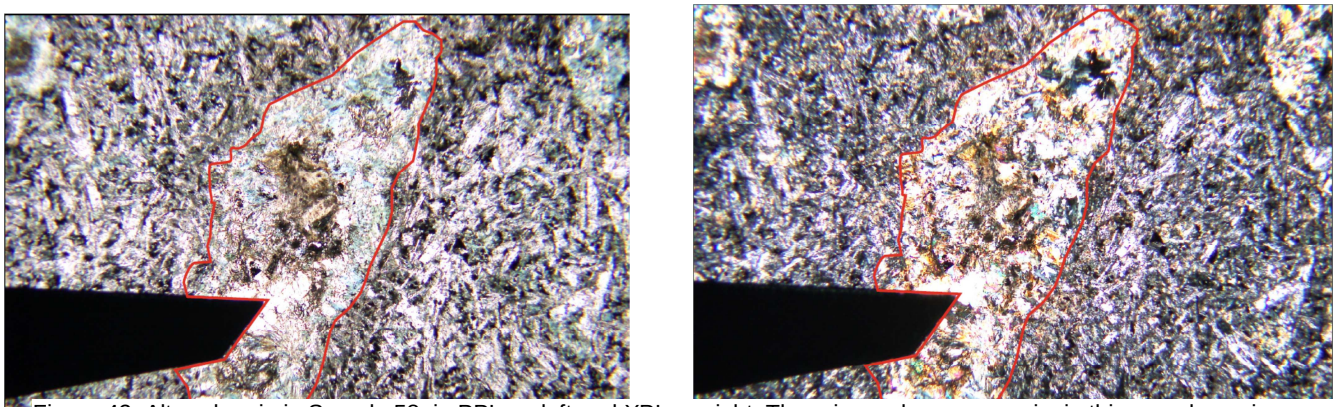

Figure 42: Altered grain in Sample 58, in PPL on left and XPL on right. There is no clear core or rim in this sample, as in sample 108B. Rather, the core and rim blend into each other. However, there appears to be some relict pyroxene in the core, based on the birefringence color.

Sample 58B in hand sample appeared spotted, with 1 millimeter-across black dots visible in the dark gray groundmass. A pyrite crystal was found on one edge, a few feldspars

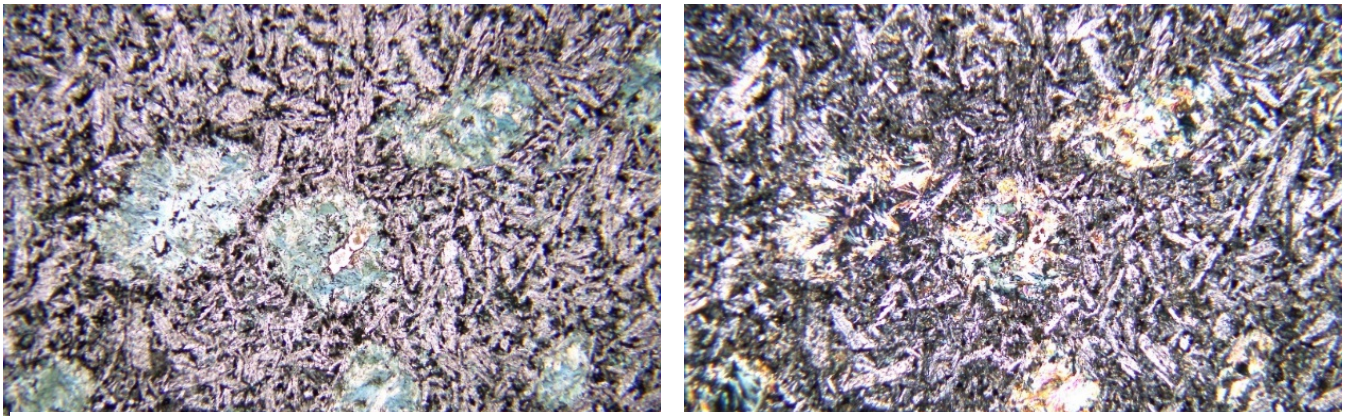

Figure 43: Sample 58, showing texture in PPL on the left, and XPL on the right. Altered grains as shown above in Figure 37 are distributed throughout the sample, with the approximate frequency as shown in the image on the left, with plagioclase laths and opaques making up the matrix.

were also visible, approximately 0.7 centimeters long and 1 millimeter across. In thin section, altered pyroxene was present (Figures 43 and 44). Plagioclase, as determined by the

distinctive twinning, is distributed throughout as laths. The alteration appears to be pyroxene altering to amphibole, as the grains appear greenish in plane polarized light. The sample is composed of 50% plagioclase, 40% amphibole/pyroxene, and 10% opaques.

Sample G4A had vugs in the hand sample, with small angular plagioclase grains approximately 0.5 centimeters long. The hand sample was light brown in color. In thin section, alteration was apparent as green minerals visible in both plane-polarized and cross-polarized light, indicating the presence of amphibole (Figure 46). Biotite grains were apparent as well as hornblende grains (Figure 45). Additionally, throughout the sample there was a bimodal distribution of plagioclase laths. Opaque minerals appear small and anhedral. The sample is composed of 65% plagioclase, 15% amphibole/pyroxene, 10% biotite, and 10% opaques.

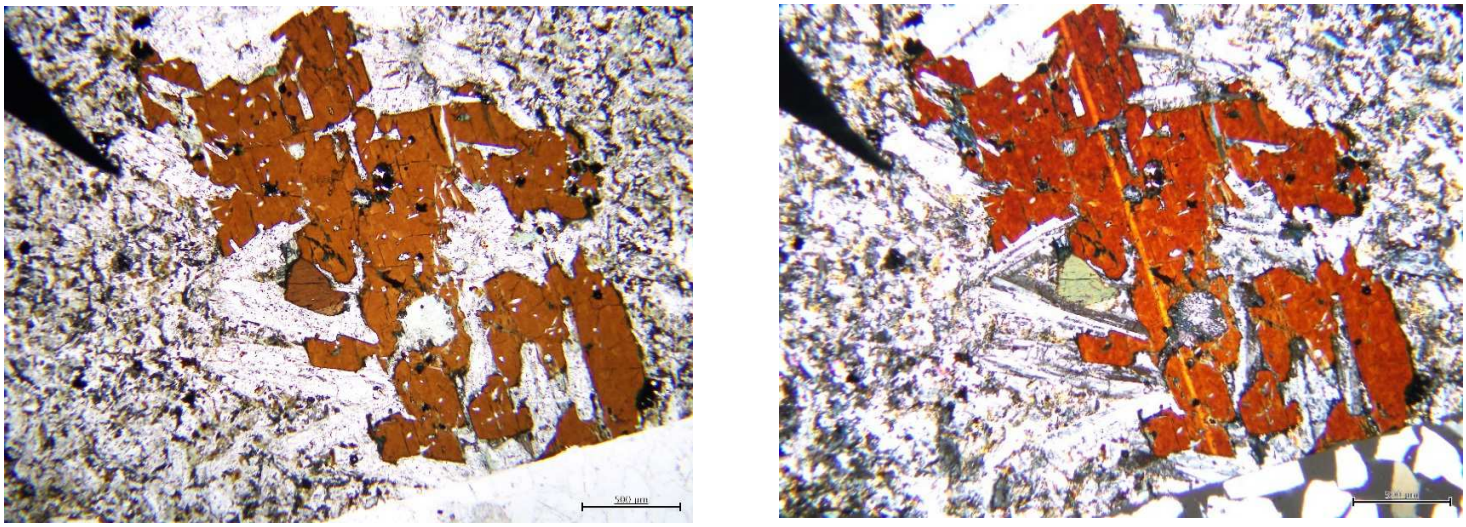

Figure 44: Sample G4A, showing large biotite grain in Sample G4A, PPL on left and XPL on right.

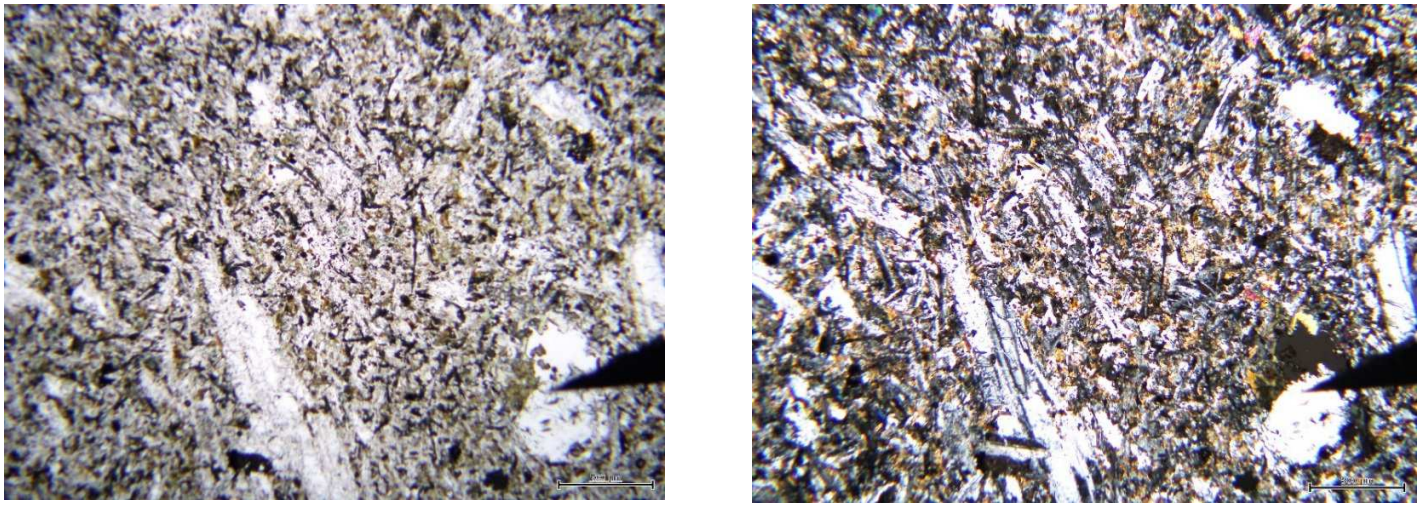

Figure 45: Sample G4A. PPL on left, XPL on right. Photograph shows texture of sample, as well as the bimodal distribution of plagioclase crystals.

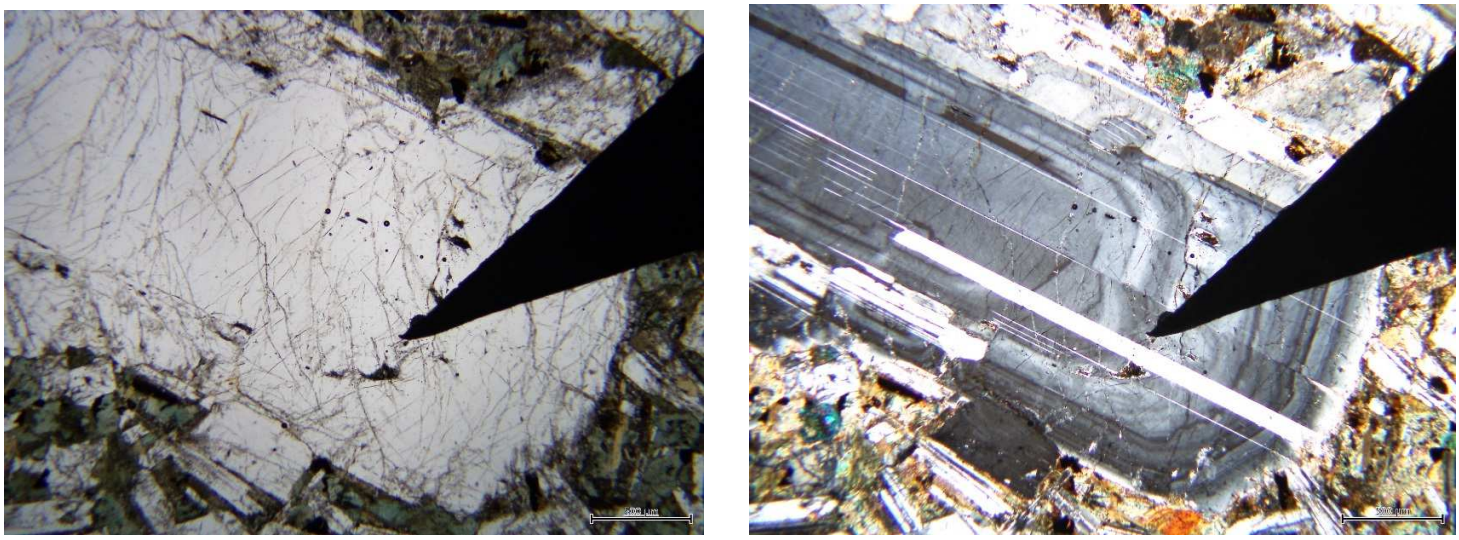

Figure 46: Large zoned plagioclase crystal showing oscillatory zoning overprinted by plagioclase twinning in Sample G4B. Image on right is in XPL, while image on left is in PPL. Large black arrow is aluminum tape used in SEM/EDS analysis to point out sampling site.

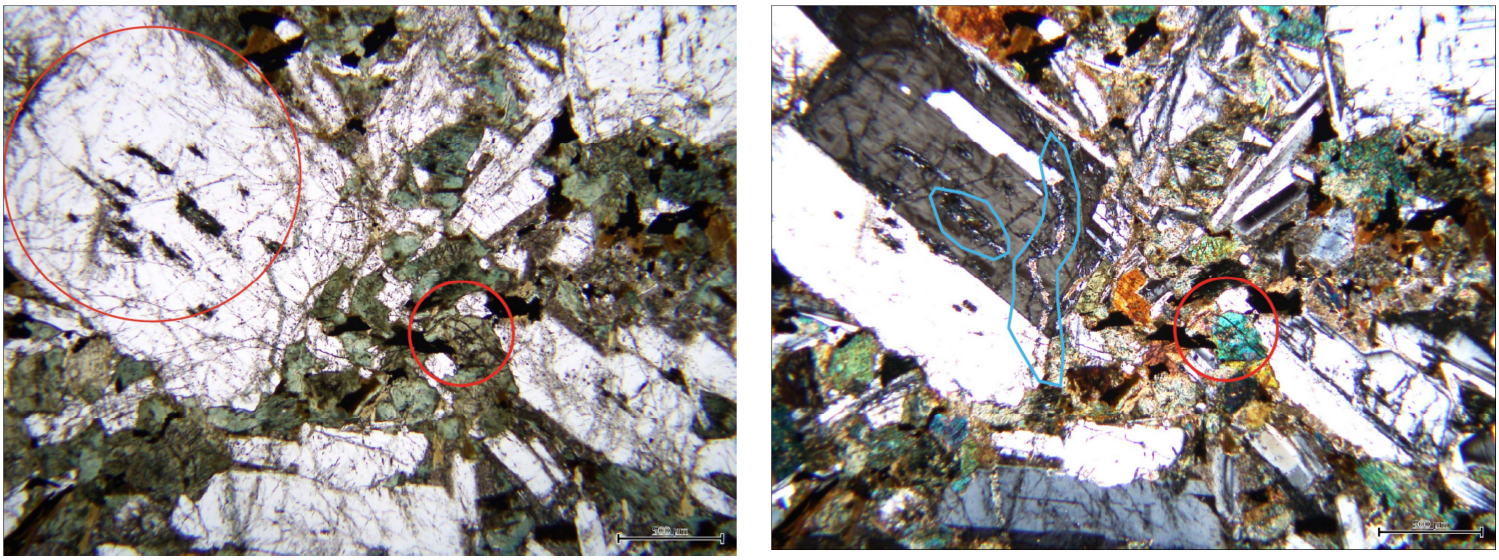

Figure 47: Sample G4B. Red circle on left-hand side image (PPL) shows areas of cataclasis. Red circle on right hand side image (XPL) shows the same area of cataclasis. Blue polygons on right hand side image show areas of alteration within the cataclasis, as well as inclusions within the larger plagioclase grain. Additionally, the bimodal plagioclase distribution is displayed. A biotite grain is visible in the center of the field of view.

Sample G4B, from the core of the large dike downstream from the Mill Brook Bridge, had a porphyritic texture in hand sample, with large subhedral plagioclase grains. The groundmass appeared dark gray in color. In thin section, there was significant alteration of the grains, pyroxene had altered to a green mineral, likely an amphibole (Figure 48). There was also bimodal distribution of plagioclase crystals throughout. Biotite was also found in the

sample, along with amphibole. Opaques in the sample are anhedral. In this sample, as in sample 108B, there were inclusions within some of the grains. This sample also shows cataclasis of the grains, as shown in Figure 48 outlined in blue. Large zoned plagioclase gains are found throughout the sample (Figure 47). Plagioclase accounts for 65% of the sample, with biotite composing 10%, amphibole composing 15%, and the opaque minerals accounting for 15%. There is no fabric apparent in the sample.

Sample 52B was dark brown to black in hand sample, with feldspar crystals visible. In thin section, the rock has an aphanitic texture, with twinned plagioclase laths throughout (Figure 50). Altered grains are present throughout the sample, consisting of green cores surrounded by brown rims. This indicates alteration of pyroxene to amphibole. The

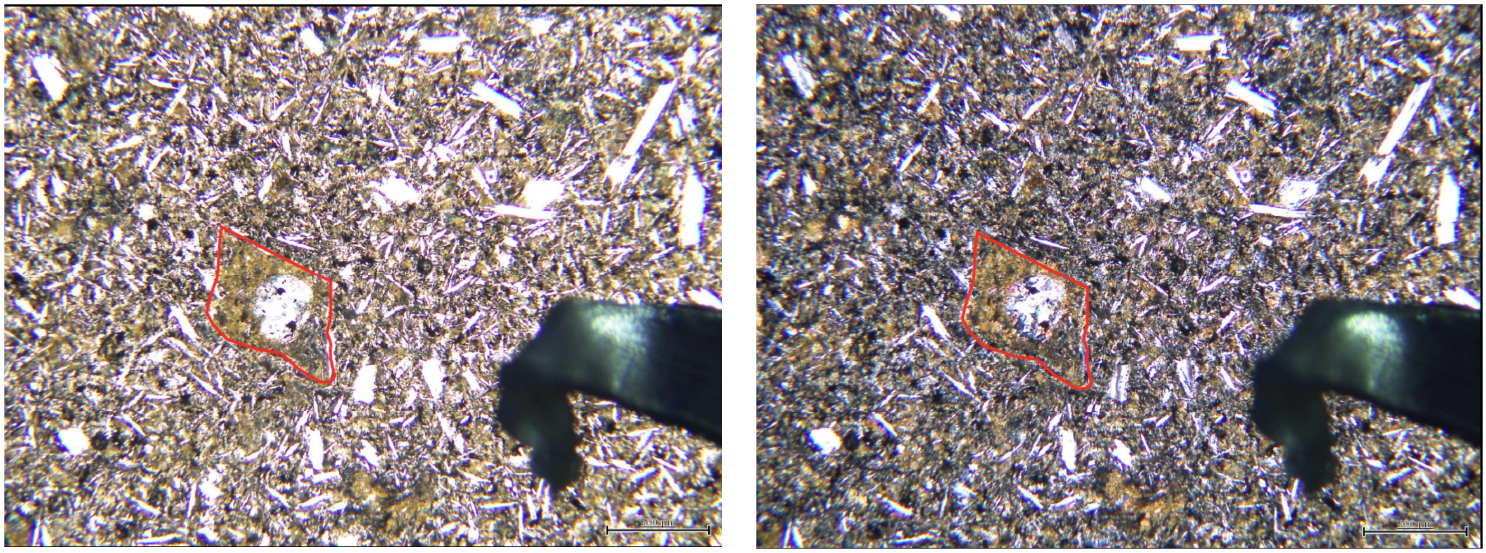

Figure 49: Sample 52B, red polygon shows location of an altered grain. Image on left is in PPL, image on right is in XPL.

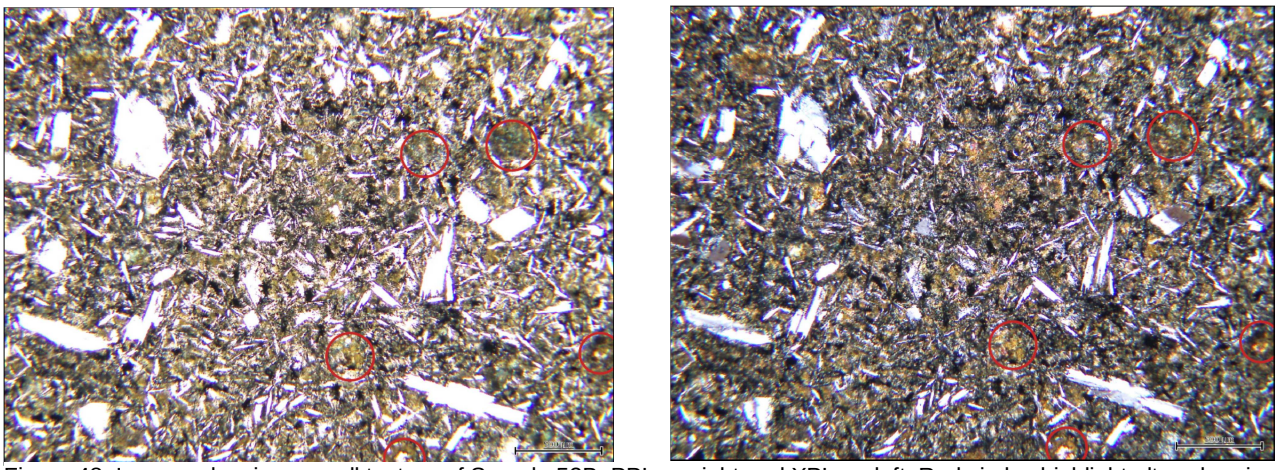

Figure 48: Images showing overall texture of Sample 52B, PPL on right and XPL on left. Red circles highlight altered grains in both samples.

groundmass also shows alteration itself, as visible from the brown color. Opaque minerals were needle shaped. There is no fabric apparent in the sample. The sample is composed of 40% plagioclase, 30% amphibole, 20% pyroxene, and 10% opaque minerals.

3.5 SEM/EDS Observations

EDS analyses were performed to identify unknown minerals in order to further understand the basalt mineralogy, mineral chemistry and ultimately their petrogenesis. Point analyses were performed on all but sample G4B, on which an X-ray linescan was performed on an oscillatory zoned plagioclase crystal. All spectra can be found in the Appendix at the end of the document.

The SEM was used to analyze an altered grain in Sample 108B (Figure 51). Three points were analyzed in this grain. The points chosen were the inside of the grain, the rim of the grain, and an opaque that was present near the grain. Based on the element analyses returned by the EDS, the interior of the grain appears to be pyroxene, while the rim is

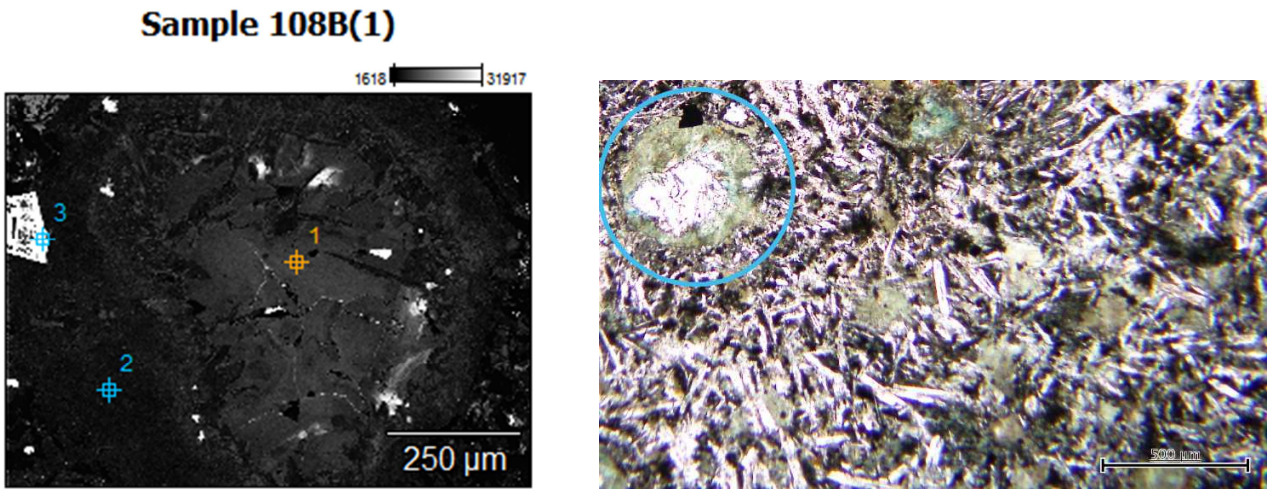

Figure 50: SEM image of Sample 108B on left, showing points of beam analysis. Image on right is PPL, showing location of altered grain slightly rotated about 45° from the left image. Number one is a pyroxene, number two is an amphibole, and number three is a pyrite. The pyrite grain in the right hand image corresponds to the white grain on the left hand image, where the number 3 is.

composed of amphibole. Analysis of the opaque grain along the rim of the grain returns as pyrite.

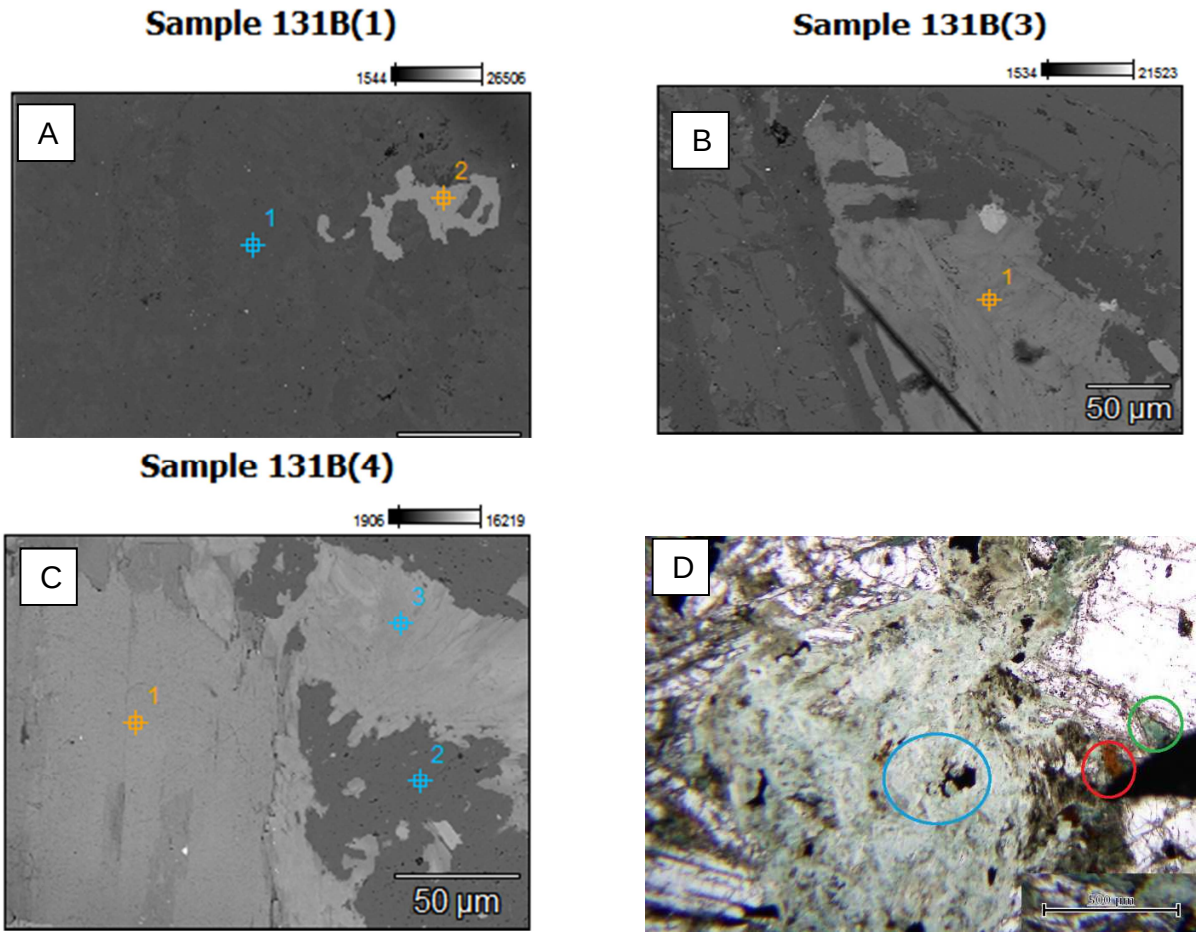

Figure 51: SEM images of Sample 131B showing location of point analyses. The locations of each are marked on the PPL image on the lower right. Image A corresponds to the blue circle, image B corresponds to the green circle, and image C corresponds to the red circle. In image A, number one is an amphibole, number two is an ilmenite grain. Image B shows an amphibole grain. Image C: point 1 is a biotite grain, point 2 is an albite grain, point 3 is a chlorite grain.

Sample 131B was analyzed a total of six times. The first analysis was of the green area and EDS results showed it to have an amphibole composition. The opaque shown in Figure 52a was determined to be ilmenite. Analysis of the grain in Figure 52b indicated the presence of amphibole. The last area analyzed in this sample represents three adjacent grains (Figure 52c), the largest of which is the brown grain evident in Figure 46d, and corresponds to point 1 in Figure 52c. The first point analysis revealed the brown grain to be a biotite, point 2 to be an albite. Point three is a chlorite grain.

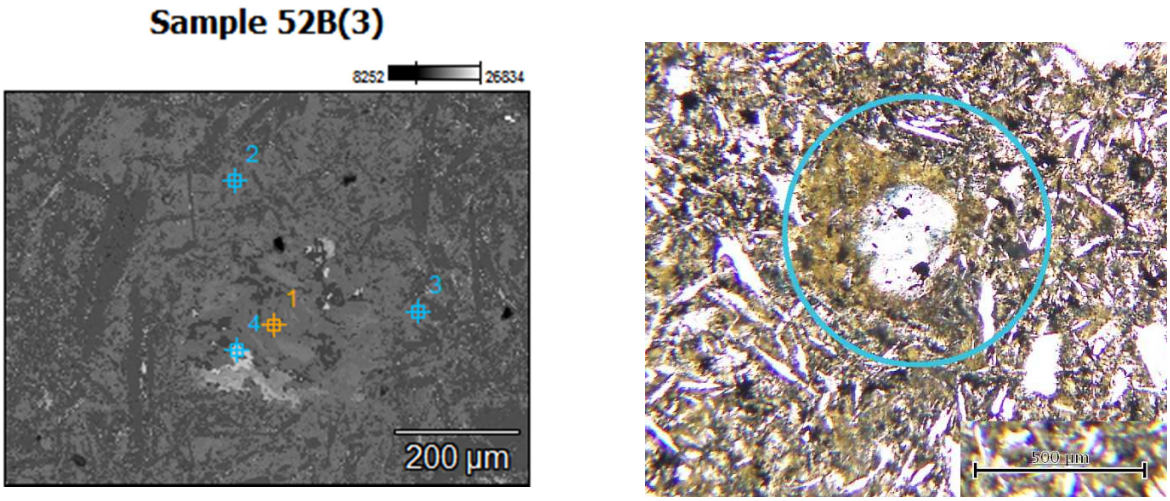

Figure 52: SEM image of Sample 52B showing points of analysis, PPL image on right shows location of grain in sample. The red arrow indicates the location of the same opaque inclusion. Point one is a diopside grain, points 2 and 3 are biotite, and point 4 is a pyrite grain.

Sample 52B was analyzed in four separate spots, though point 2 and 3 were both done on the rim of the altered grain to determine if there was any spatial chemical variation in the mineral. The interior of the grain was determined to be a diopside based on the presence of Mg, Ca, Fe (Figure 53, point 1). Points 2 and 3, present in the rim around the diopside grain, indicate a biotite composition. Point 4 is a pyrite grain, as determined from the presence of Fe and S.

Sample 58B was sampled a total of four times. Through the EDS spectrum, it was possible to identify wurzite (Figure 54a), as well as micas (Figure 54b). Sample spots 1 and 3 in Figure 54b were both found to have calcium present, while sample spot 2 had both sodium and calcium. Mineral formulas for the three mica spots were determined from the EDS data.

Sample G4A had a large biotite grain (Figure 56). An altered grain present in the sample was also analyzed, it appeared to be composed of three separate grains (Figure 57). The first grain was determined to be a plagioclase feldspar. The second point was identified as a biotite grain. The third point sample was identified as quartz (Figure 57).

Sample 214 had one altered grain of interest. Four points on and around the grain were analyzed (Figure 55). The grain in the center, which appears reddish in the PPL image in Figure 55, was determined to be mica. Point 2, which is the plagioclase around it, confirmed the presence of a potassium feldspar. The opaque (point 3) has elemental values for Zr, Si, and O, potentially making it an altered zircon. The final area of analysis, point 4, was revealed to be another potassium feldspar.

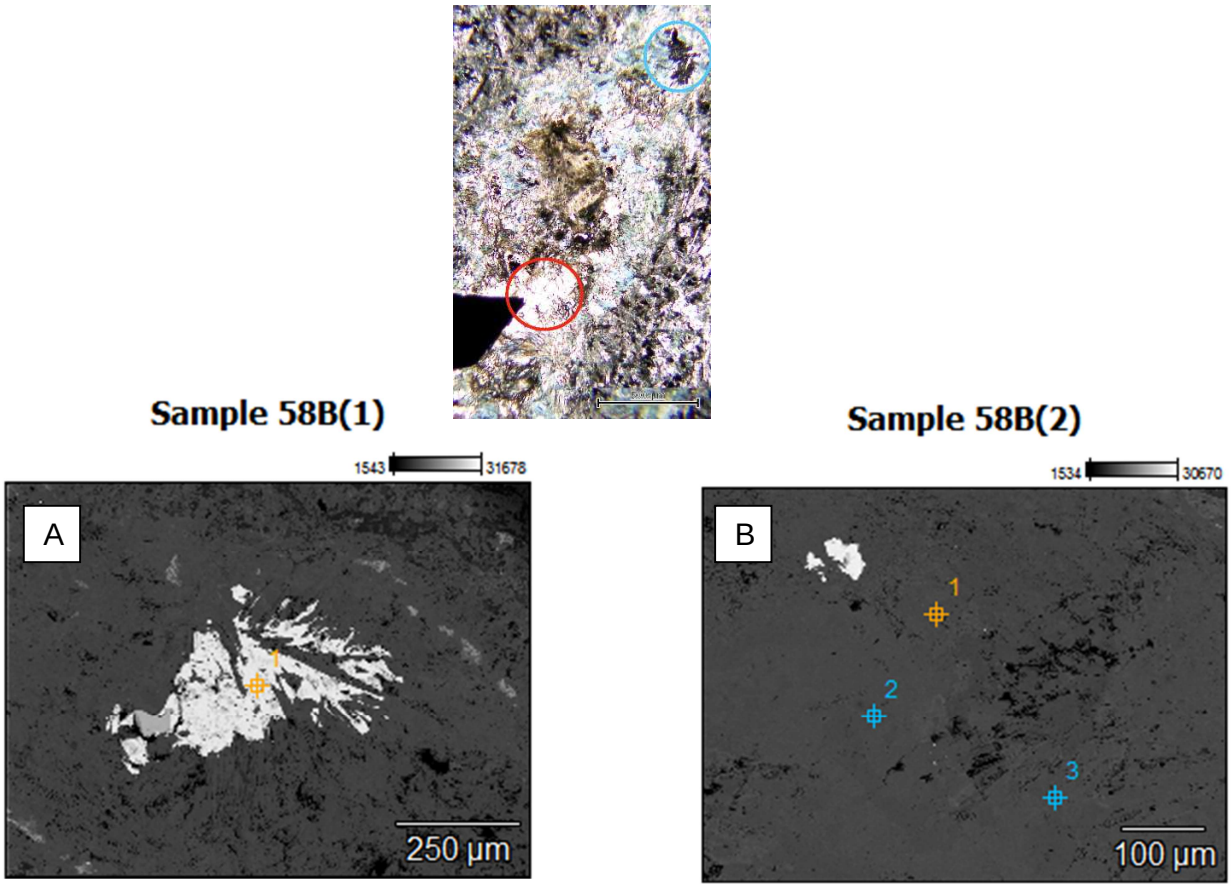

Figure 53: SEM images of Sample 58B showing location of probe points. PPL image on top shows location of sample points. Image A corresponds to the blue circled area, while Image B corresponds to the red circled area. Point one in image A is a wurtzite grain. In Image B, points 1, 2 and 3 are micas.

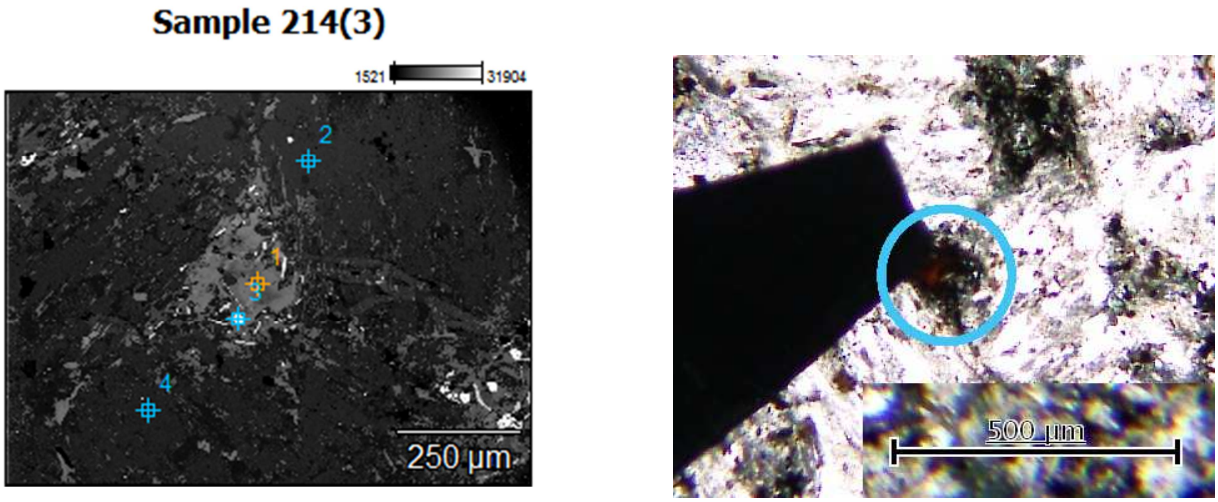

Figure 54: SEM image of Sample 214, showing altered grain. PPL image on right shows location of analysis relative to overall slide.

Sample G4B contains a large-zoned feldspar. This was analyzed with the X-ray linescan tool in the NSS software (Figure 58). In particular, the elements of interest were calcium, iron, sodium and potassium. The graph along the transect arrow shows iron and potassium staying mostly constant throughout. However, as expected in an oscillatory-zoned plagioclase, sodium and calcium do show variations. Overall the Ca increases towards the rim while the Na decreases.

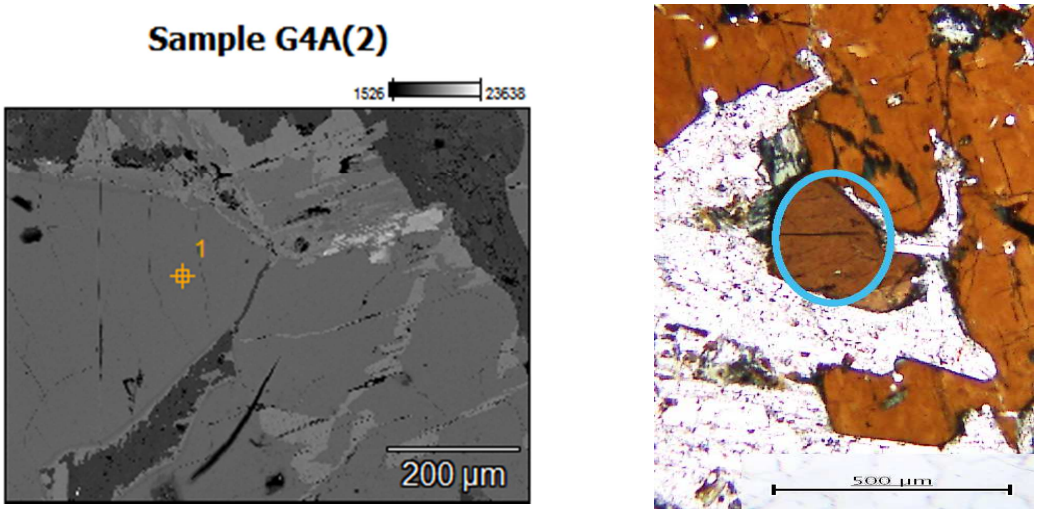

Figure 55: Sample G4A showing sample sites from SEM/EDS analysis. PPL image on right shows location of sample site, the blue circle corresponds to the analyzed grain in the left hand image. Point 1 is a biotite grain.

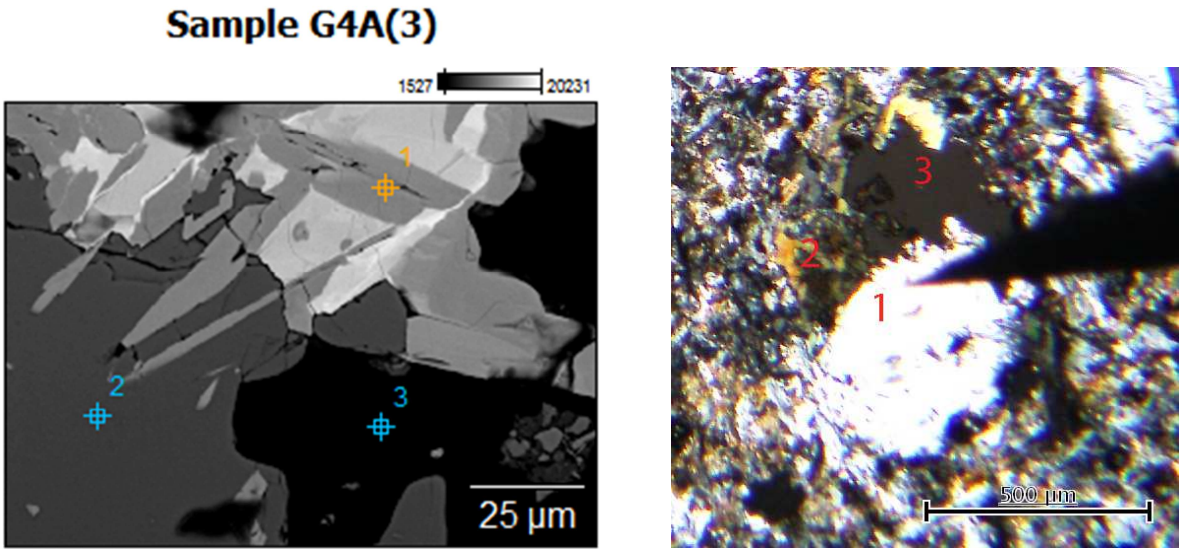

Figure 56: Sample G4A showing SEM sample sites. The numbers on the PPL image on left correspond to the numbers on the SEM image, showing the location of the point analyses. Point 1 is a biotite grain, point 2 is a plagioclase feldspar grain, and point 3 is a quartz grain.

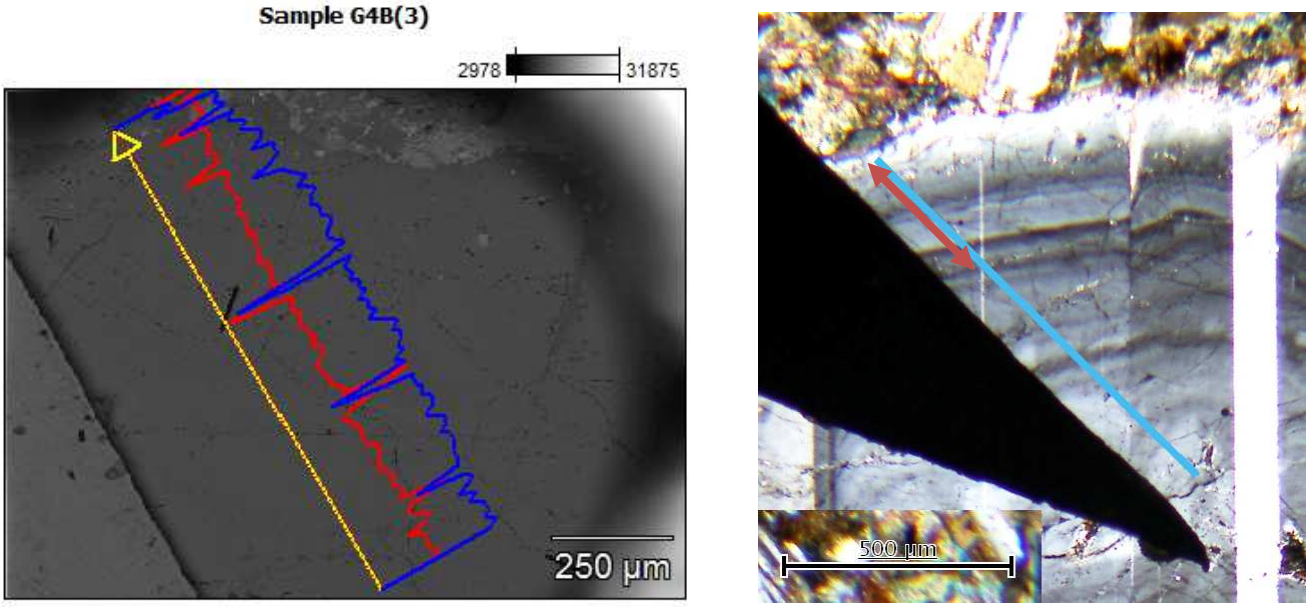

Figure 57: Sample G4B image from X-ray linescan analysis. The counts of the elements of interest are plotted along the extent of the arrow. The counts end at the arrowhead. Blue corresponds to sodium and red to calcium. Image on right shows location of sample area in PPL, orange arrow shows extent of linescan.

3.6 X-Ray Fluorescence Results

XRF analyses were completed on eight samples from throughout the quad. Of these eight, only one (sample 100) was not made into a thin section. XRF analysis was performed to ascertain the petrogenetic connections between the dikes and the tectonic setting.

The X-ray fluorescence data was separated into three groups, the Dike Zone group, the Mill Brook group, and the North-South group (Table 1). Each group was created to test the hypothesis that, individually, they are of the same geochemical origin. Group selection was determined by the strike of the dikes, as well as the geographic locations.

The Dike Zone samples extend through the northwestern side of the quadrangle, from the upper left corner through the middle of the northwestern edge (Figure 59). Because of the linear relationship of the Dike Zone samples, they were grouped together to explore the hypothesis that the samples represent one geochemical origin. The North-South was selected to test the hypothesis that the N-S striking dikes throughout the quadrangle are indeed of one geochemical origin. The Mill Brook samples are from the same geographic area, directly below the bridge at the intersection of Rt. 115 and the Cherry Mountain highway.

Group	Sample Number	Strike	Dip
Dike Zone	131B	207	63
	G4A	95	70
	G4B	30	70
	108	180	45
	52	2	90
Mill Brook	131B	207	63
	G4A	95	70
	G4B	30	70
North-South	58B	190	81
	52B	2	90
	214	5	69
	100	187	90
	108	180	45

Table 1: Table showing samples assigned by geographic locations and strike orientation.

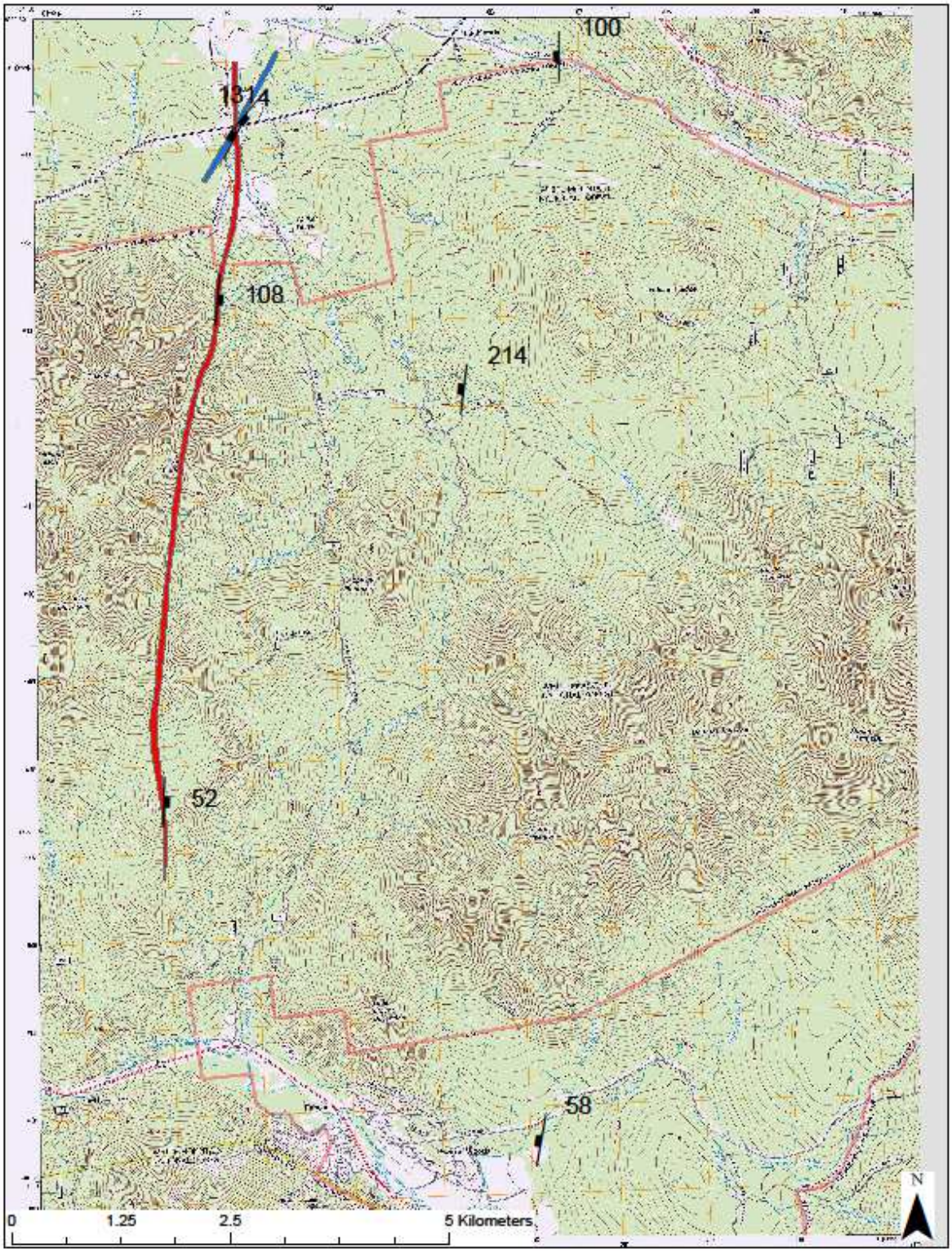

Figure 58: Sample locations are marked, and show dike strike and dip. The long red polygon shows rough outline of the Mill Brook Dike Zone. The blue section that cuts obliquely is colored only to show the change in orientation. (Topographic base map from USGS).

Sample	Al2O3 (wt%)	CaO (wt%)	Fe2O3 (wt%)	K2O (wt%)	MgO (wt%)	MnO (wt%)	Na2O (wt%)	P2O5 (wt%)	SiO2 (wt%)	TiO2 (wt%)
G 4a	17.3	6.41	8.51	2.34	2.96	0.181	4.45	1.329	52.57	2.276
G 4a	17.37	6.42	8.52	2.36	2.95	0.18	4.43	1.333	52.6	2.286
G 4a	17.12	6.42	8.53	2.34	2.96	0.181	4.45	1.326	52.3	2.269
G 4b	19.56	9.8	9.78	1.36	4.71	0.305	2.95	0.344	49.07	1.894
G 4b	19.45	9.8	9.79	1.36	4.71	0.307	2.93	0.34	49.15	1.897
G 4b	19.24	9.77	9.8	1.36	4.71	0.304	2.93	0.343	48.84	1.888
G 52b	15.11	5.62	13.44	3.28	3.5	0.409	2.12	0.589	51.85	3.098
G 52b	15.12	5.62	13.46	3.29	3.51	0.41	2.1	0.593	51.97	3.113
G 52b	14.85	5.62	13.46	3.3	3.51	0.407	2.12	0.588	51.64	3.096
G 58b	16.47	7.31	13.1	1.47	5.16	0.252	3.77	0.597	47.13	3.058
G 58b	16.63	7.32	13.09	1.47	5.16	0.252	3.78	0.608	47.13	3.072
G 58b	16.38	7.29	13.11	1.46	5.18	0.253	3.75	0.597	46.91	3.053
G 100	15.85	6.78	13.29	0.86	5.1	0.234	4.13	0.49	45.67	2.953
G 100	15.89	6.8	13.3	0.87	5.08	0.235	4.1	0.491	45.53	2.956
G 100	15.77	6.78	13.3	0.86	5.1	0.234	4.13	0.493	45.49	2.94
G 108b	15.36	9.21	11.98	1.6	8.5	0.262	1.97	0.289	46.38	1.897
G 108b	15.4	9.24	11.98	1.6	8.5	0.264	1.98	0.297	46.67	1.895
G 108b	15.28	9.24	12.01	1.6	8.49	0.261	1.99	0.292	46.31	1.897
G 131b	19.76	9.91	9.42	1.01	4.89	0.205	3.18	0.306	48.85	1.691
G 131b	19.81	9.91	9.44	1.01	4.91	0.202	3.19	0.303	48.68	1.705
G 131b	19.68	9.9	9.45	1	4.88	0.204	3.2	0.295	48.68	1.704
G 214	15.85	4.92	11.65	3.18	2.26	0.205	3.82	1.037	51.56	1.546
G 214	15.88	4.95	11.63	3.18	2.25	0.205	3.83	1.045	51.5	1.543
G 214	15.78	4.92	11.66	3.18	2.25	0.205	3.84	1.039	51.45	1.537

Table 2: Raw XRF data for the bulk chemistry of the major elements. Each fused disc was run three times, the data presented in the following graphs represent averages of the three runs.

Sample	Ba (PPM)	Cr (PPM)	Zn (PPM)	Sr (PPM)	Y (PPM)	Zr (PPM)	Rb (PPM)	Nb (PPM)
G 4a	1009	101	319	1044	54	491	60	99
G 4a	1013	101	315	1034	51	488	54	96
G 4a	935	98	322	1039	49	495	57	98
G 4b	296	175	105	713	22	180	41	27
G 4b	330	192	110	714	22	183	43	29
G 4b	318	178	107	714	21	186	42	28
G 52b	709	57	255	433	40	412	226	57
G 52b	701	55	253	432	36	412	228	56
G 52b	696	49	252	431	40	419	229	57
G 58b	282	81	114	679	29	323	114	51
G 58b	216	82	106	685	33	319	113	51
G 58b	285	70	104	684	30	323	115	52
G 100	409	72	196	623	31	295	16	45
G 100	403	72	196	625	29	293	15	47
G 100	438	66	194	623	31	298	11	47
G 108b	521	348	172	563	22	149	39	27
G 108b	499	344	171	567	25	150	36	28
G 108b	529	351	168	564	22	148	35	28
G 131b	351	117	215	716	18	159	19	24
G 131b	383	109	214	716	19	155	24	25
G 131b	357	120	216	720	20	161	21	23
G 214	1054	47	63	685	47	539	90	97
G 214	1050	42	67	687	41	536	92	95
G 214	1091	44	62	686	46	542	91	98

Table 3: Raw data for the minor elements run on the eight samples.

Sample	La (PPM)	Ce (PPM)	Nd (PPM)	Sm (PPM)	Eu (PPM)	Th (PPM)	U (PPM)
G 4a	76.9	195.7	102.8	20.3	6.2	10.9	2
G 4a	71.1	204.5	104.8	19.1	6.4	11	1.7
G 4a	76	192	105.2	24.9	5.8	10.8	1.9
G 4b	24.1	53.6	26.9	8.4	6.2	4.4	2
G 4b	20.8	52.7	28.1	8.4	6.8	4.1	2.4
G 4b	20.2	61.7	29.5	3.9	7.8	3.8	2
G 52b	34.2	95.9	63.9	9.5	10.7	6.6	1.4
G 52b	31.9	93	57.4	14.2	11.3	6.7	0.9
G 52b	32.6	92.4	59.2	12.7	10	7	0.9
G 58b	28.3	78.6	56.2	19.8	6	3.6	1.1
G 58b	31.4	79.1	57.5	13.7	4.5	3.4	1.7
G 58b	28.1	79.2	57.8	14.5	5.9	3.5	0.9
G 100	27.3	70.1	55	9.8	3.6	3.5	1.8
G 100	27.7	75.9	55.8	13.1	4.1	4.4	1.3
G 100	27	67.1	55.3	10.5	4.1	4	1.1
G 108b	13.5	38.9	35.3	2.7	5.9	1.9	1.3
G 108b	13	38.8	36.8	3.3	5.2	1.7	1.1
G 108b	11.6	42.1	37.4	5.8	7.1	1.8	1
G 131b	17	45.9	26.2	2.6	4	3.5	1.3
G 131b	18.8	42.8	26.1	7.9	3.7	3	1.4
G 131b	16.9	45.8	26.6	9.7	3.7	3.1	1.6
G 214	89.3	215.2	116.7	28.2	6.7	14.1	2
G 214	86.2	225.7	117.8	25.3	6.5	14	2.1
G 214	89.6	220.1	119.3	24.1	6.4	13.5	1.9

Table 4: Raw data for the rare earth elements run on the eight samples.

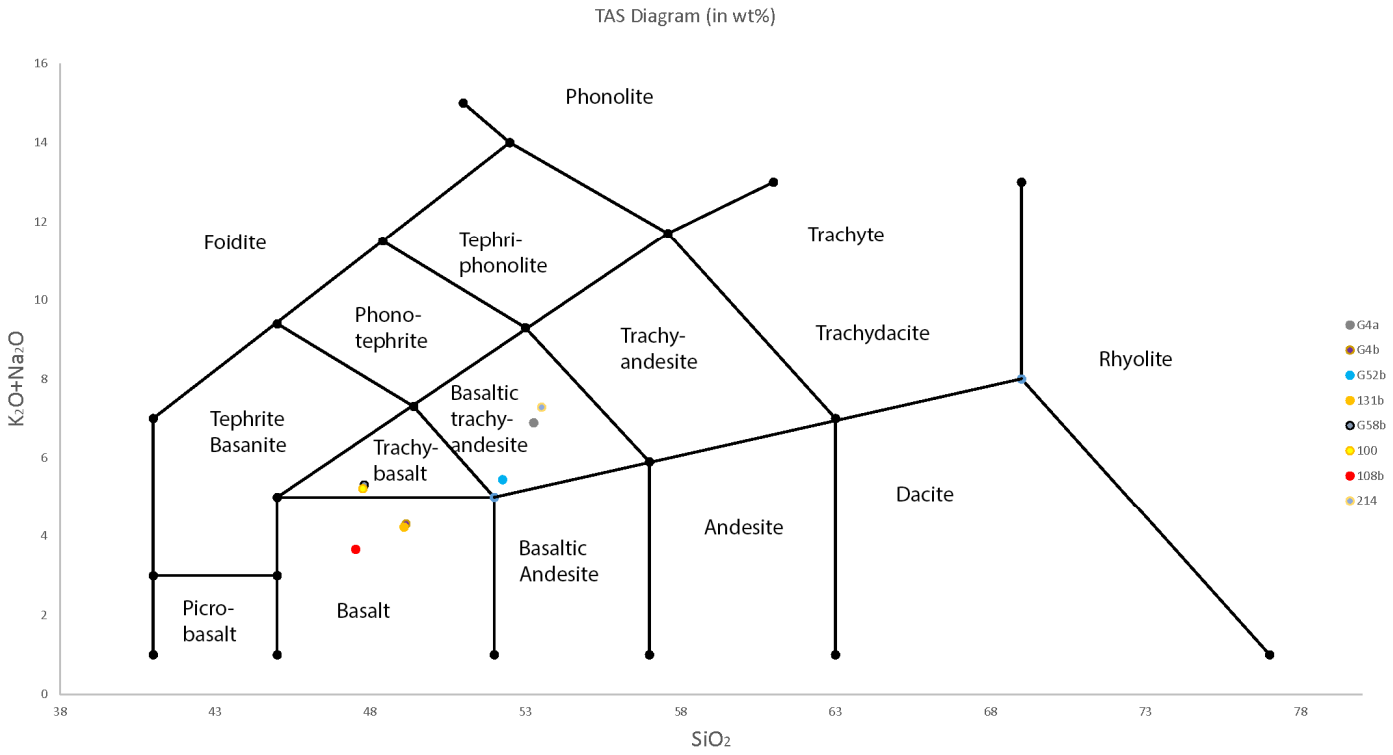

Figure 59: Total alkali silica plot. Samples are shown individually, refer back to Table 1 for group assignments.

X-ray fluorescence results were plotted in a total alkali silica plot to help determine each sample's formal rock name (Figure 60). The Dike Zone samples do not occupy the same category, with sample 100 plotting as a trachy-basalt, sample 108b plotting as a basalt, and sample 214 plotting as a basaltic trachy-andesite. Of the Mill Brook group, samples G4A and 52b plot as basaltic trachy-andesites, and samples G4B and 131b plot as basalts. The North-South group dikes also show geochemical variation. Samples 100 and G58B plot on top of each other in the trachy-basalt category, sample 108B plots in the basalt category, and samples 214 and G52B plot in the basaltic trachy-andesite category. The overall trend of the data moves from the basalt category diagonally through the trachy basalt category to the basaltic trachy andesite category.

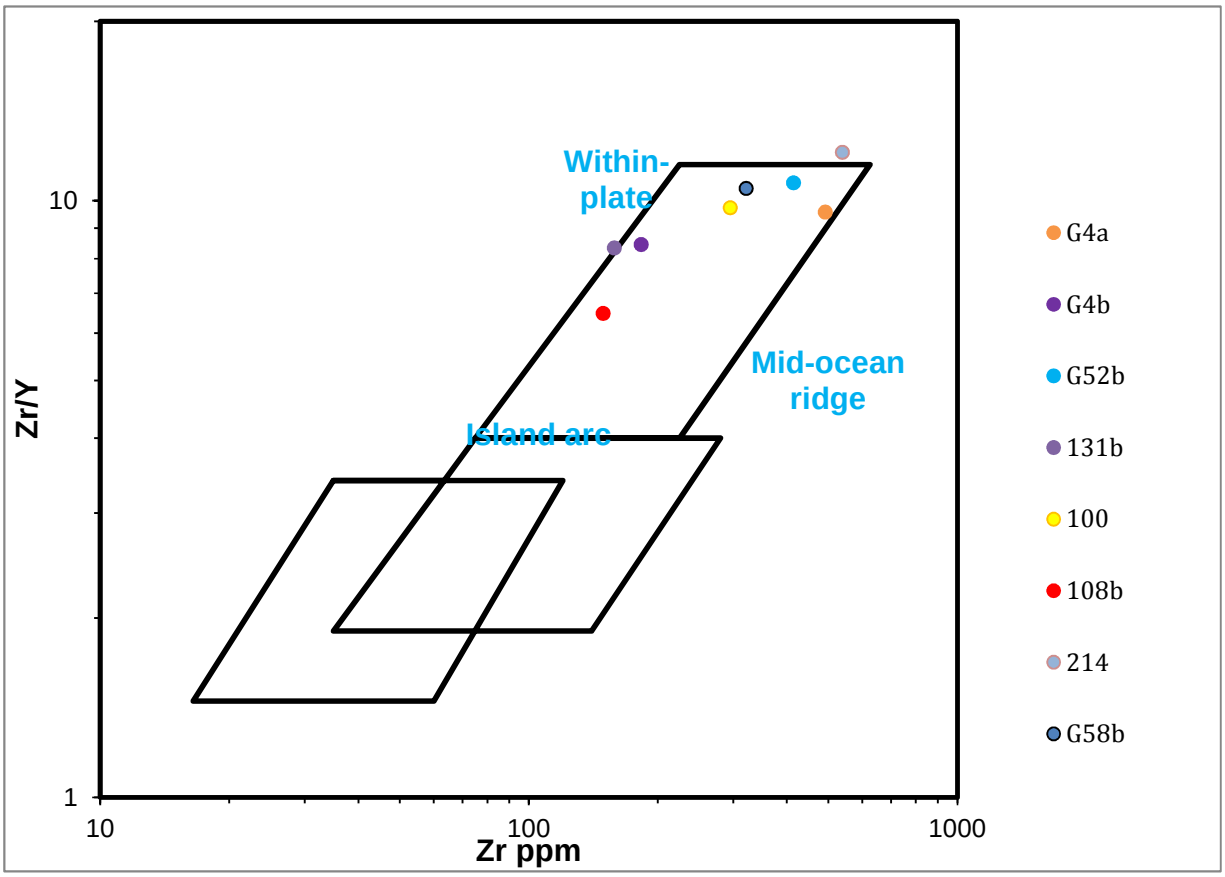

Figure 61: Tectonic classification graph. Classification data from Pearce and Norry (1979).

X-ray fluorescence data were also plotted on the Zr/Y vs Zr (ppm) tectonic discrimination diagram of Pearce and Norry (1979) (Figure 61). All of the samples plot in the “Within-plate” field. Sample 214 is significantly enriched in Zr, even relative to the other samples. Due to this, it plots outside the “Within-plate” field. Based on the indications of the tectonic classification diagram, the samples were then normalized both to chondrite and to mid-ocean ridge basalt. Normalizing the data to chondrite will allow comparison to “within plate” composition. Similarly, normalizing the data to MORB will allow it to be compared it to the composition of the mid-ocean ridge environment.

By normalizing the data to mid ocean ridge basalt, the MORB REE graph shows reasonable conformity, with only small amounts of variation, between samples (Figure 62). The values for Rb show the most variation, with the tightest cluster for Sr. There is a fair amount of variation in the Ce, Y, and Sm values. There is a sharp increase in Ba for all samples followed by a sharp drop to Th.

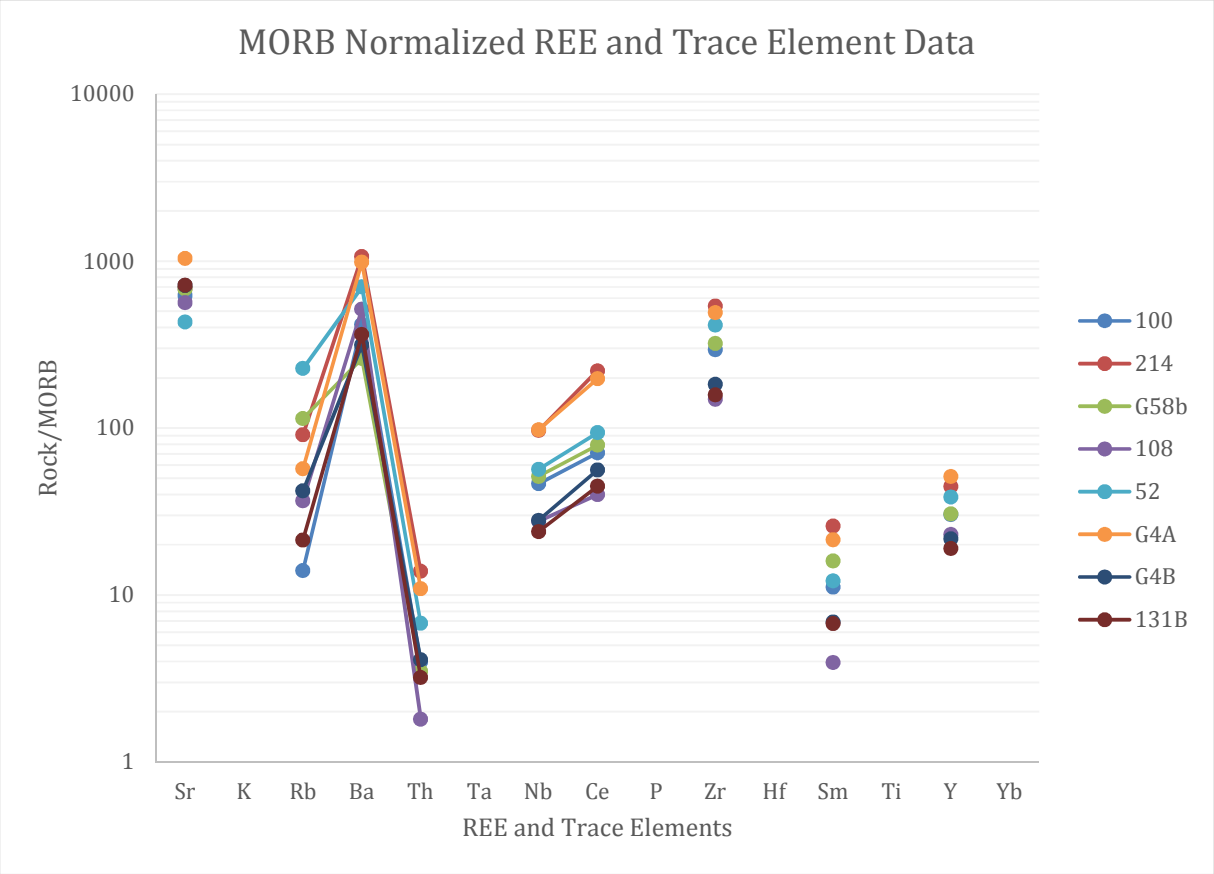

Figure 64: MORB normalization values from Pearce (1983).

Figure 63 shows the available REE values normalized to chondrite, all data are enriched relative to chondrite. The data for all samples from La and Ce appear to parallel each other in value. The lowest Eu values belong to sample 131B. The tightest grouping for all data points is for Ce. Samples 214, G4A, G58B all have a consistent negative slope from Nd to Eu, while all other samples show a change in slope at Sm. Additionally, samples G4A and 214 have very similar values for each REE, and appear to parallel each other. All data points are enriched relative to MORB.

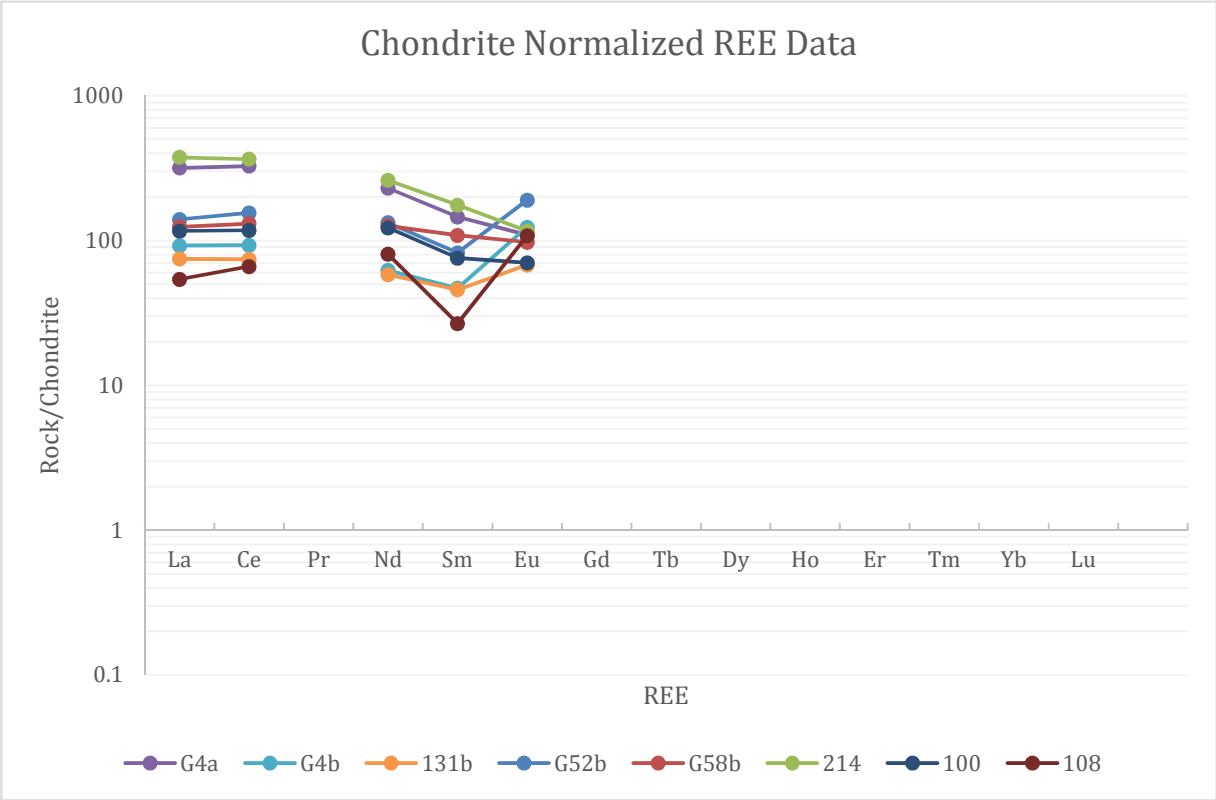

Figure 67: All dike data. Chondrite normalizing data from McDonough and Sun (1995).

4. Discussion

The main import of this study is to explore several questions, namely: 1) the relationship between the Mill Brook Dike Zone (MBDZ) and the tectonic history of the region; 2) whether the N-S striking dikes are of similar magmatic origin to each other; and 3) the relationship between the MBDZ and other regional mafic intrusions. The discussion aims to answer these questions by comparing the MBDZ data to published data for regional dikes of similar size (i.e. Christmas Cove, Caraquet, Higganum dikes) and geographic and tectonic setting.

The findings presented in this study indicate that the MBDZ did not form as part of CAMP, unlike other regional mafic intrusions. Instead, the MBDZ appears to be among the younger mafic intrusions in the northeast. It is geochemically distinct from other dikes of similar size. The XRF data suggest a few interpretations: that the MBDZ samples form a possible fractionation or crustal contamination trend, or alteration due to hydrothermal fluid. Figure 64 shows the location of the MBDZ relative to other macro-scale mafic dikes.

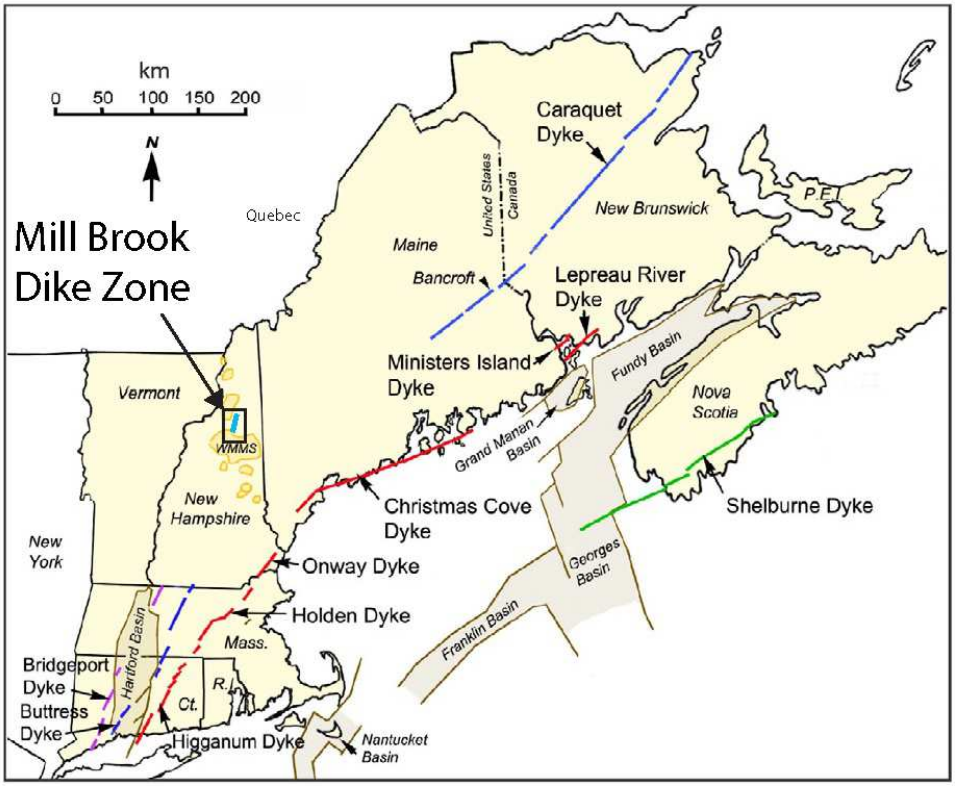

Figure 70: Geographic location of Mill Brook Dike Zone relative to other large mafic intrusions. (Modified from McHone et al., 2014).

4.1 Comparison to Other Regional Mafic Intrusions

The Mill Brook Dike Zone can be readily compared to other large mafic intrusions in the northeast. The Christmas Cove, Caraquet and Higganum dikes are some of the larger ones in the New England-Brunswick area, and significant research has been done on them (McHone et al., 2014; Burke et al., 1973; Dunn et al., 1998; Philpotts and Asher, 1993). Comparing the MBDZ to these large intrusions gives insights into formation history and chemistry of the MBDZ. The majority of these large regional intrusions are attributed to CAMP volcanism, but based on the data returned from this study of the MBDZ, it seems unlikely that the Mill Brook

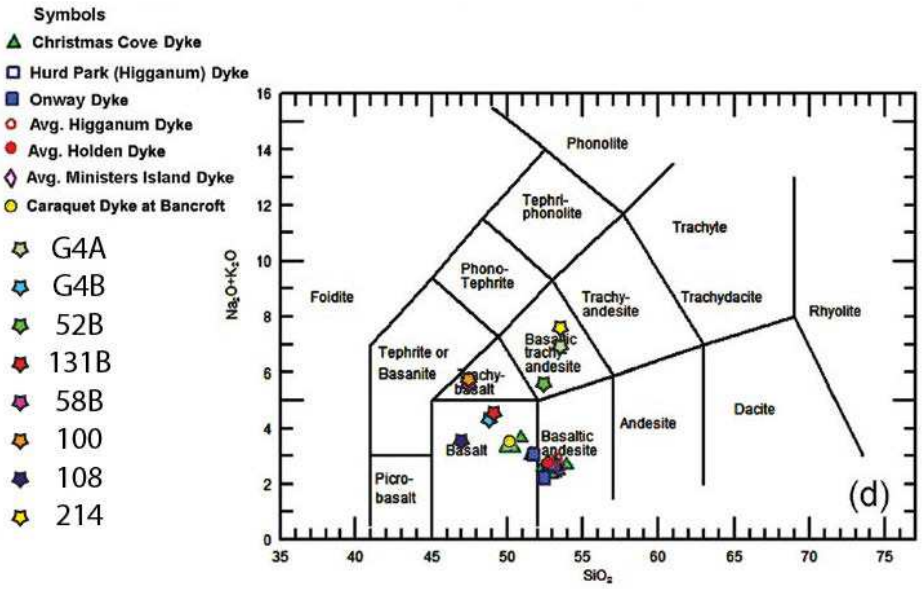

Figure 71: TAS diagram showing comparison of Mill Brook Dike Zone data to CAMP data. Samples are numbered. (Modified from McHone et al., 2014).

Dike Zone formed in relation to CAMP volcanism.

Figure 64 shows the labeled samples from the MBDZ plotted alongside data from CAMP dikes as determined by McHone et al. (2014). Comparison of MDBZ XRF data to recently published data from McHone et al. (2014) indicates that the MBDZ was composed of geochemically distinct magma from other large regional dikes (Figure 65). Data from the other large mafic intrusions cluster around the basalt and basaltic andesite field, indicating lower Na_2O and K_2O values than those of the MBDZ. Figure 65 also plots data from the Pinnacle, Escape Hatch and Upper Trail dikes in the nearby Huntington Ravine region of the Presidential

Range (Gardner, 2010). Certainly the data from the Escape Hatch and Pinnacle dike fit within the geochemical “envelope”. However, the orientation of these dikes are different from the

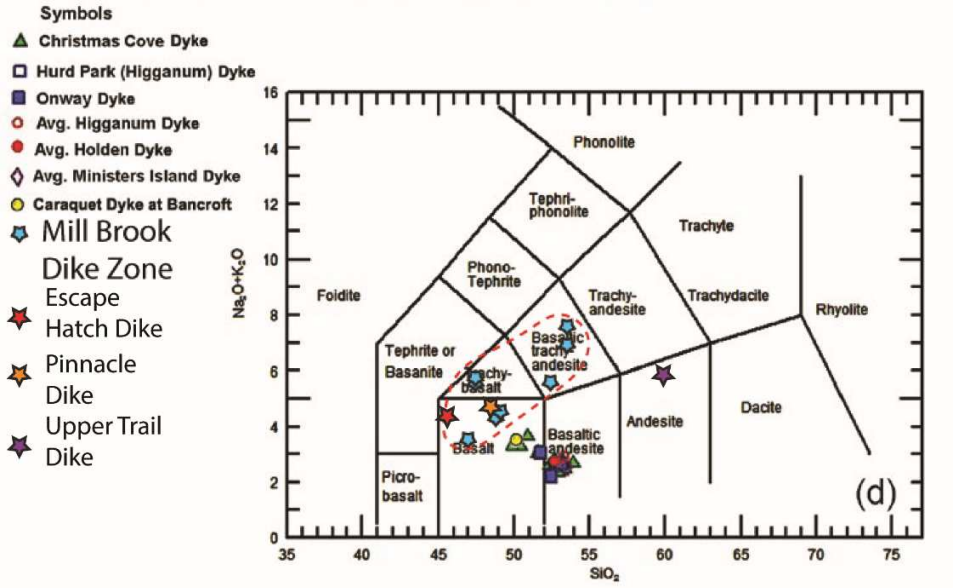

Figure 72: Comparison of mafic intrusion data from the Mill Brook Dike Zone and Huntington Ravine to data from large regional mafic intrusions in the New England - Quebec area. The red dotted line indicates the envelope of MBDZ data. All MBDZ data has been plotted as blue stars to illustrate the trend more clearly. (Modified from McHone et al., 2014; Gardner, 2010).

orientation of the MBDZ, with the Pinnacle dike striking NE-, and the Upper Trail and Escape Hatch dike striking E-. Gardner (2010) attributes the formation of the Pinnacle and Escape Hatch dike to the Jurassic ENA province and the Upper Trail dike to the Cretaceous NEQ province based on correlations to paleostress fields presented by Faure et al. (2006 and 1996b). In light of this new data, it seems geochemically possible that the dikes observed in Huntington Ravine belong to the same magmatic system as the MBDZ. However, cross cutting relationships presented by Gardner (2010) suggest that N-S joints are younger than these dikes. The correlation of the MBDZ to the ENA or NEQ provinces would be questioned if Gardner's (2010) N-S joint sets correlate to the N-S striking MBDZ.

4.2 Explanation for the Geochemical Variation in the Mill Brook Dike Zone

The tectonic classification diagram (Figure 66) indicates within-plate formation for the majority of samples. This would seem to lend validity to the hotspot hypothesis or a rifted continental crust source, as the magma would erupt within-plate. Basalts that erupt in within-plate settings have high Zr/Y ratios relative to mafic intrusions from other tectonic environments, such as a MORB setting, where the basalts will have lower absolute values of Ti

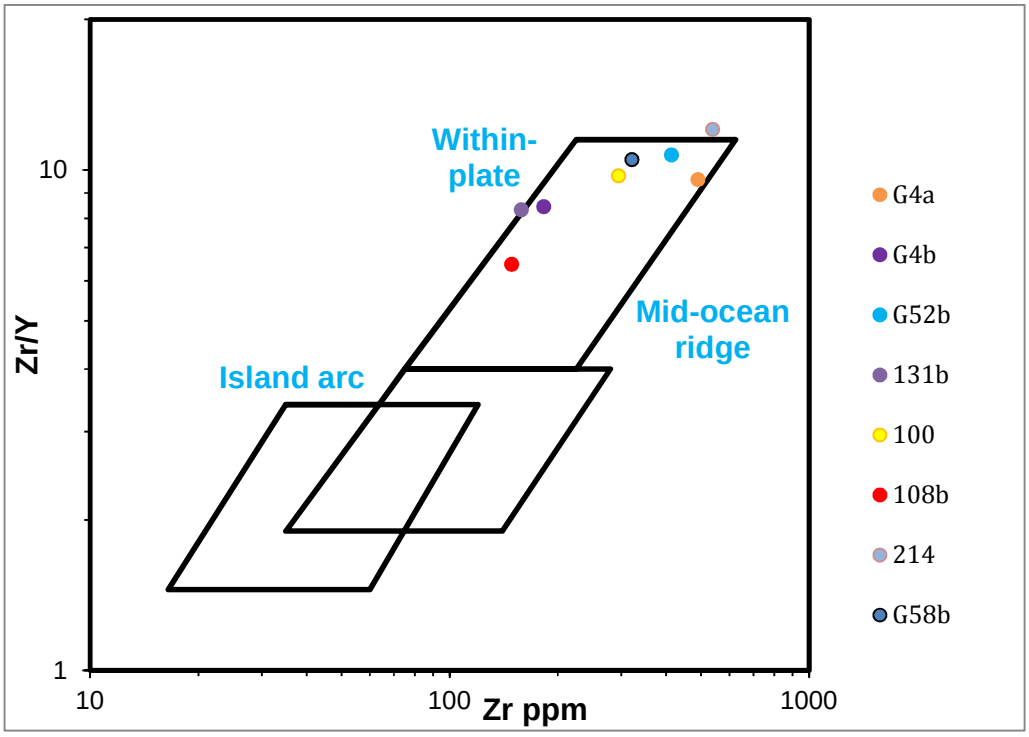

Figure 73: Tectonic classification diagram for MBDZ samples (Data from Pearce and Norry, 1979).

or Zr relative to samples from a within-plate setting (Pearce and Cann, 1973; Pearce and Norry, 1979). The Alkalies-Iron-Magnesium ternary diagram (Figure 68), plots the MBDZ data as well as data from McHone et al. (2014). This again shows the distinction between the MBDZ and CAMP data and may shows an iron enrichment followed by an iron depletion suggestive of a tholeiitic trend (Zimmer et al., 2010) though more data is needed to verify (Figure 68).

The TAS diagram (Figure 65) shows a geochemical trend (red dashed oval) of the dikes in the MBDZ. One possible explanation of this is a fractionation trend. Fractionation trends

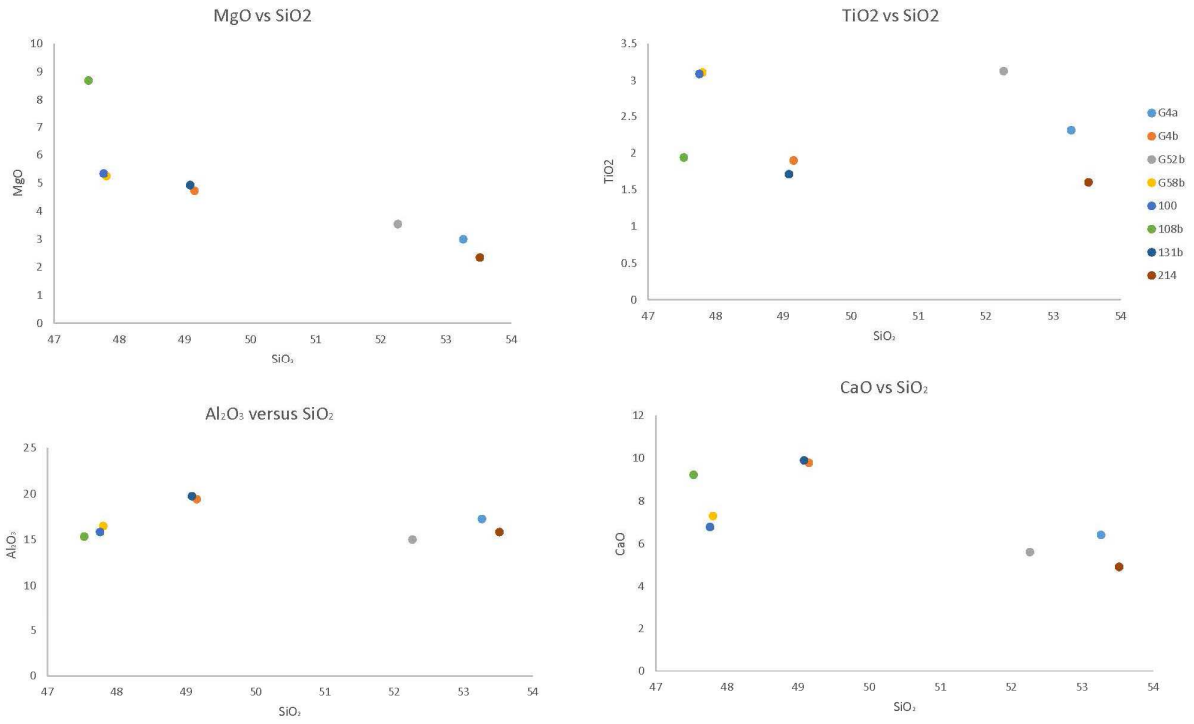

Figure 76: Variation diagrams showing concentrations of various oxides plotted against SiO2. No linear trend is immediately visible, except in the MgO plot in the upper left hand corner. This could be due to the process of fractionation, rather than assimilation wall-rock.

have been observed in areas with hotspot attributed volcanism, i.e. Iceland (Haase et al, 1997). An alternative explanation would be assimilation of the wall-rock into the magma. If assimilation were responsible, it would be expected that the composition of the rock would change along a mixing line when plotted on variation diagrams (Figure 67; Winter, 2010; Best, 1982). Such variation diagrams plotted with MBDZ data do not show a linear relationship. The MgO graph shows what could be interpreted as a linear trend, but since the other graphs do not indicate a linear relationship, this can be explained by fractionation. To confirm this, more

samples from the MBDZ should be collected to extend the range of data. $^{87}Sr/^{86}Sr$ analysis should be performed. Continental crust becomes enriched over time in $^{87}Sr/^{86}Sr$, therefore magmas that are higher in $^{87}Sr/^{86}Sr$ are likely contaminated by continental material (Winter, 2010). Finding an $^{87}Sr/^{86}Sr$ ratio higher than 0.706 would strongly indicate crustal contamination, and vice versa (Winter, 2010). The third explanation may be that the significant alteration of the rocks by hydrothermal fluid introduced inconclusive or difficult to explain trends.

The pattern that the Zr/Y data (Figure 66) may also show an evolving magma composition, which corroborates the similar evolutionary magmatic trend seen in the TAS diagram (Ray et al., 2011). An increase in zirconium generally indicates increasingly evolving magma. Similarly, lower levels of yttrium are observed in more primitive basalts (Ray et al., 2011). As for sample 214, it could be that the other samples are enriched in Zr relative to it, as basalts that erupt at active continental margins often are enriched in Nb, Ta, Zr and Hf (Pearce, 1983).

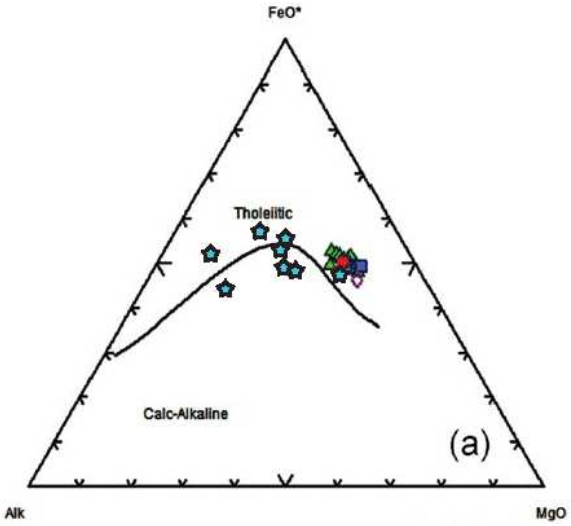

Figure 79: Alkalies-Iron-Magnesium classification and differentiation diagram after Irvine and Baragar (1971), showing both MBDZ data (blue stars) and data from the Christmas Cove Dike, the Higganum Dike, and the Caraquet Dike. The MBDZ data describes a significantly different trend than the CAMP intrusions. (Modified from McHone et al., 2014).

CAMP data from McHone et al. (2014) was plotted alongside data from the MBDZ (Figure 69). The CAMP data represents within-plate rifting magma due to crustal extension, i.e. continental rifting. In comparing the data from McHone et al. (2014) to the REE data from the MBDZ, it becomes apparent that there is a significant difference in REE concentration between the two sample sets (Figure 69). This difference underscores that the MBDZ is not a part of CAMP, both geochemically and temporally (a timeline of events is presented later in the discussion). The chemical difference between the two data sets also indicates that the MBDZ did not form in a continental rift setting. The MBDZ is significantly enriched in REE relative to the various CAMP dikes, as would be expected from an OIB source (e.g. Tristan da Cunha, Cape Verde), rather than a MORB source (Fitton, 2010).

Comparing the MBDZ to various other formation environments shows another significant difference in REE concentration (Figure 70). The Figure from White (2010) shows

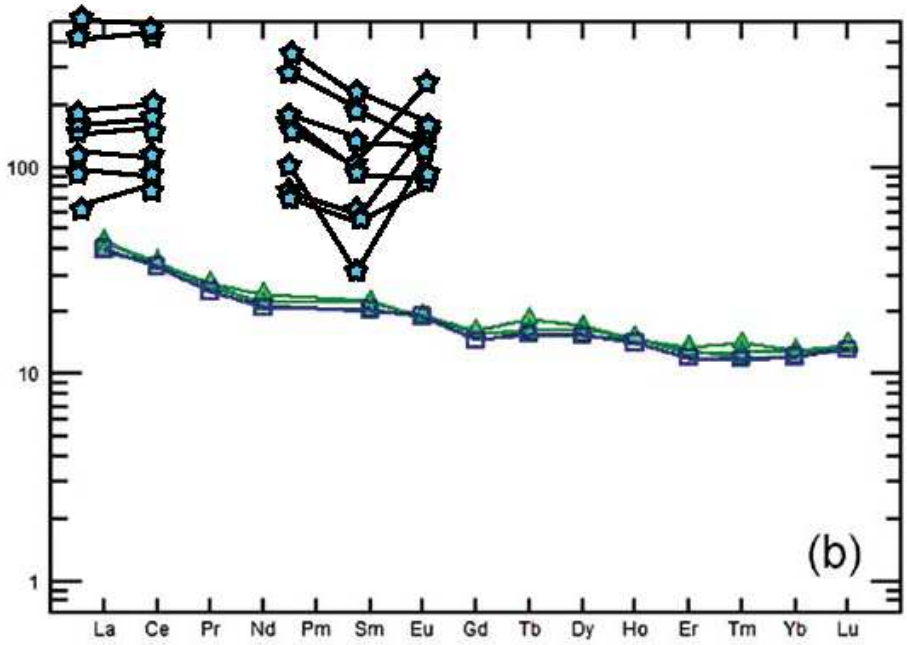

Figure 82: Rare earth element plot normalized to chondrite, showing data from the MBDZ (blue stars), Christmas Cove dike, Higganum dike, and Caraquet dike. The extreme difference in values makes a strong case that the MBDZ is not a part of CAMP. (Modified from McHone et al., 2014).

MORB and various types of OIB (EM I, EM II, HIMU). OIB is proposed as the characteristic basalt type that erupts at hotspots and frequently erupts in continental rift systems (Fitton, 2007; White, 2010). The substantive difference between the MBDZ data and the data from White (2010) indicates a much more enriched source for the MBDZ magma than would be expected from an OIB source. This indicates that the MBDZ is also not OIB-like in composition, but instead represents an intrusion much more enriched in incompatible elements. Again, performing isotopic analyses on the MBDZ samples would provide more certainty in determining the tectonic formation of the MBDZ, as isotopes do not fractionate (Winter, 2010). This means that the initial isotope ratio of a melt will be identical to the melted source isotope ratio. The isotopes vary depending on the tectonic environment, and can be determined by $^{87}Sr/^{86}Sr$ ratios (Winter, 2010).

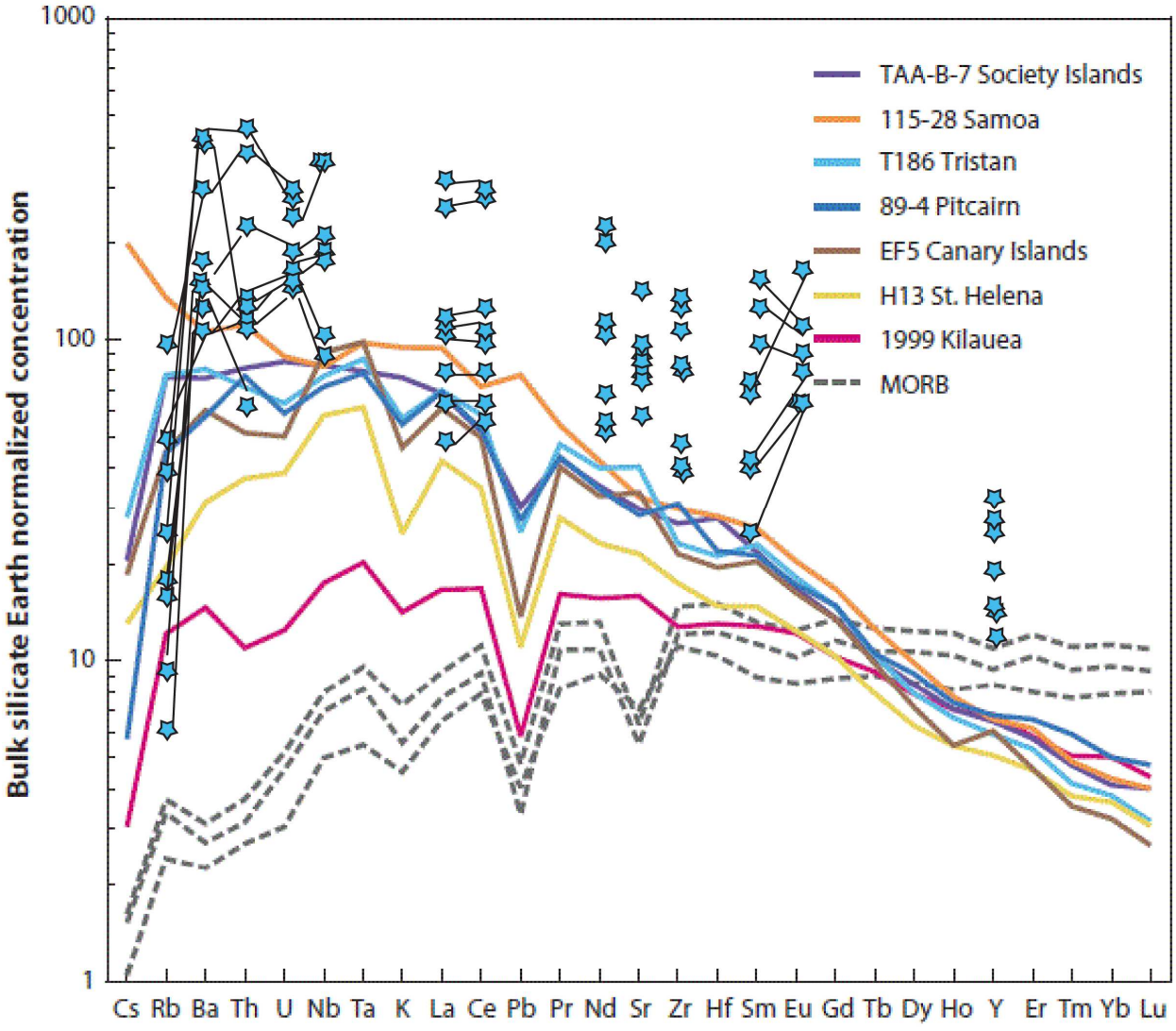

Figure 85: Spider diagram from White (2010) showing chondrite normalized concentrations, ordered by increasing compatibility. MORB, Hawaii, the Canary Islands, St. Helena (HIMU - OIB), Tristan da Cunha, Pitcairn (EM-1 - OIB), Samoa, and the Society Islands (EM-2 - lOIB). MBDZ data (blue stars) are also plotted.

4.3 Mineralogy of the Mill Brook Dike Zone

Comparison of the plagioclase phenocryst composition of the MBDZ to data from McHone et al. (2014) shows a relationship between the rims of the labradorite/bytownite phenocrysts from the dike at Swans Island, ME. The plagioclase phenocryst composition of the MBDZ is An_{50}-An_{70} (Figure 71). This can be compared as well to the observations of Fowler-Billings (1944), who observed optically that the plagioclase has a composition of An_{42}-An_{70}.

Optical work done for this study by the author confirms the presence of sericite, a

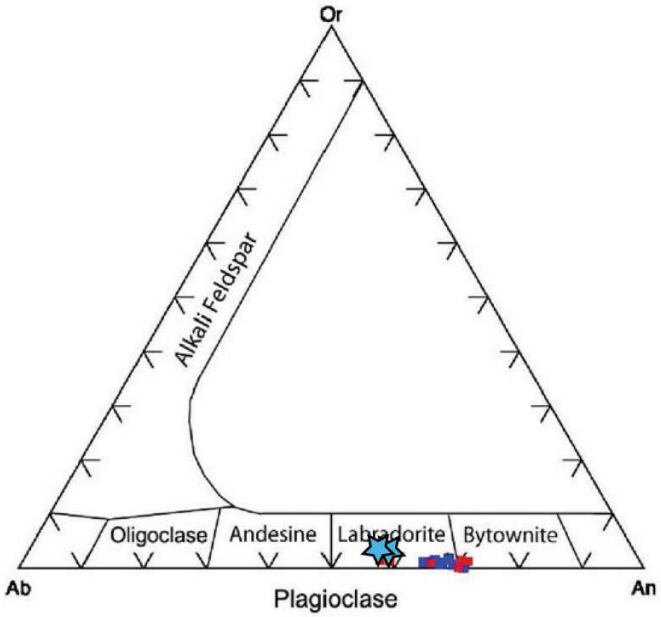

Figure 86: Comparison of plagioclase phenocryst composition. Blue stars indicate data from the Mill Brook Dike Zone. Blue squares indicate cores of labradorite/bytownite grains, while red squares indicate the rim. The labradorite/bytwonite grains are from the Swans Island Dike (Modified from McHone et al., 2014).

common alteration mineral of plagioclase feldspar, and is often seen in hydrothermal alteration of felsic rocks rather than mafic rocks (Creasey, 1966; Rose, 1970; Lowell and Guilbert, 1970). The majority of the samples in this study appear to be diabases, as determined by the mineralogy and texture (Klein and Hurlbut, 1986; Fowler-Billings, 1944). Diabases are attributed to extensional crustal environments (Armstrong et al., 1982).

The extent of mineral alteration apparent in these dikes is not seen in the adjacent lithologic units within the study area. The alteration minerals and cataclasite textures indicate some hydrothermal and tectonic event that both altered and fractured the grains in the dikes, either at the same or different times. Possibly the alteration and cataclasis are due to the

reactivation of the Ammonoosuc fault in the Cretaceous, which would have preferentially used the existing planes of weakness, i.e. the MBDZ (Roden-Tice et al., 2009).

Zoned plagioclase found in the coarse interior of several dike samples indicates changing pressure and temperature conditions, which could result from crystallization due to exhumation of the dike from below to the surface (i.e. sample G4b). If the dike injected around 100 Mya, the area of study would have been approximately 2 kilometers below the surface, assuming the constant exhumation rate of 0.02 mm/yr as calculated by Roden-Tice et al. (2012).

4.4 Comparison of Mill Brook Dike Zone to Presidential Range Dikes

Previous Bates Geology thesis students, Kindley (2011) and Gardner (2010), performed paleostress and petrogenetic analyses of the mafic intrusions found in the Mount Washington quadrangle. Both workers observed flow textures of the basalts in Great Gulf and Huntington Ravine, respectively. The basalts in both study areas were found to contain amygdules of calcite, and in a few cases, chlorite. Alteration is present in the majority of samples, which both Kindley and Gardner interpret as hydrothermal alteration.

Kindley (2011) sampled three dikes in Great Gulf: the Clay Gully dike, the Diagonal Gully dike, and the Airplane Gully dike. Kindley did not perform XRF analyses, and therefore did not classify the dikes by chemical composition. The Clay Gully dike strikes approximately 70˚ and dips 65˚S. The Diagonal and Airplane Gully dikes both strike at a similar angle to the Clay Gully dike, but dip at 75˚S. Kindley interpreted the flow banding present in the dike samples as evidence for repeated brittle injections, which are likely related to phases of the rifting-drifting of Pangea (Petcovic and Dufek, 2005). Plagioclase compositions throughout the dikes found in Great Gulf were consistent at An_{60} - An_{70}.

Gardner sampled three dikes in Huntington's Ravine: the Pinnacle Dike (45, 58SE), the Upper Trail Dike (270, 89.5N), and the Escape Hatch Dike (263, 59N). Both the Pinnacle Dike and Escape Hatch Dike were found to be alkalic dolerites, while the Upper Trail Dike was found to be an andesite (Figure 65; Gardner, 2010). Separate flows are visible in the samples, ranging in texture from coarse-grained to fine-grained. Gardner interpreted these textures to suggest fluid flow in the basalt due to continuous and multiple magma injections.

No flow textures were observed in the thin section samples from the Mount Dartmouth quadrangle. Additionally, no amygdules were observed. However, the large dike underneath the Mill Brook Bridge did show evidence of multiple injections, as seen in Figures 71 and 72 below. Though no flow banding was observed in the samples taken from the 20 meter dike below the Mill Brook Bridge, based on the field observations it seems likely that these structures represent the same mechanism of multiple brittle injections that were responsible for creating the flow banding textures in the Great Gulf and Huntington's Ravine dikes (Petcovic and Dufek, 2005). This can be confirmed from the presence of internal chilled margins, as seen in Figures 72 and 73.

Figure 88: 20 meter wide dike below Mill Brook Bridge, striking 207˚, dipping 63˚NW. Dashed red arrows show areas of "dike-within-dike" injections. Note rock hammer for scale. Image from Eusden, 2014.

Figure 87: Detail of above photograph, red lines highlight the dike injection that shows chill margins from brittle injection. Image from Eusden, 2014.

4.5 Model for the Paleostress and Emplacement History of the Mill Brook Dike Zone, its Subsequent Alteration and Cataclasis

This section attempts to outline the paleostress and emplacement history of the MBDZ as well as its post-intrusion alteration and cataclasis history. Figure 74 shows the orientation of all joint and dike data from the study area. In the Mount Dartmouth study area, the MBDZ and all other dikes have N-S strikes with similarly oriented joints. This suggests an overall E-W extensional setting for the MBDZ and the dikes and joints of the Mt Dartmouth quad in general.

Both the synoptic equal area projection for the study area and the Mill Brook specific equal area projection show N-S striking data, indicating a quadrangle-wide distribution of N-S

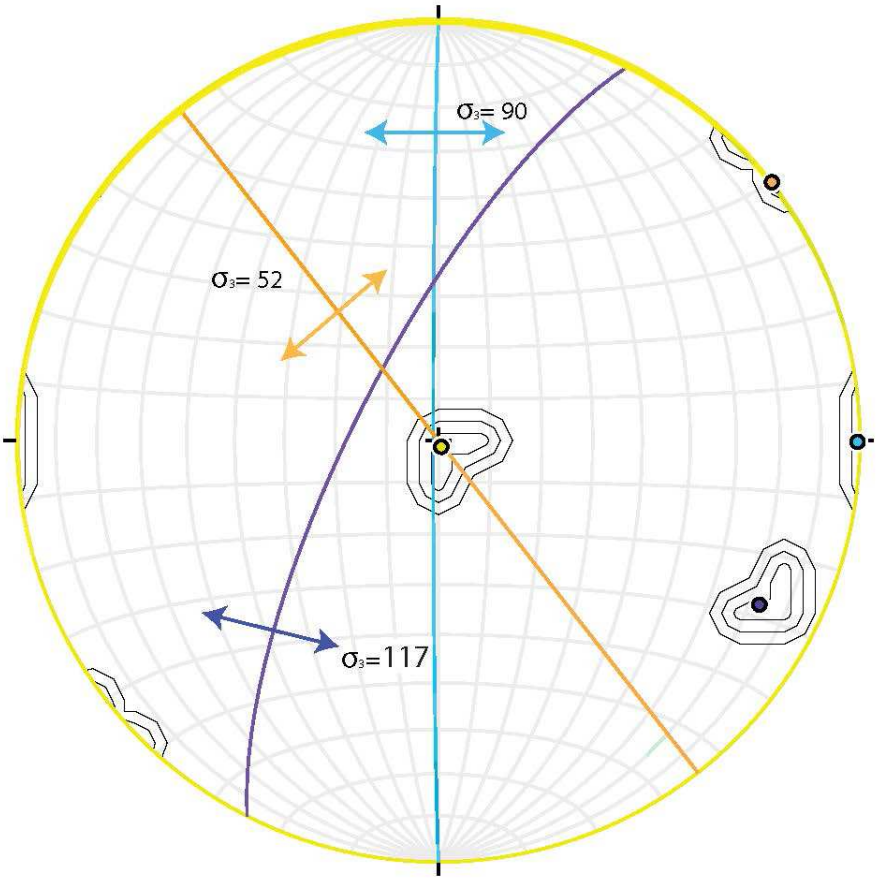

Figure 91: σ3 is oriented perpendicular to the average orientation of each joint set. Therefore, extension is oriented parallel to σ3. This stereonet represents the results of the entire data set, both joint and dike data.

striking joints in addition to the N-S striking dike zone (Figure 74). This supports the E-W stress of the MBDZ. N-S striking joints were not found at Upper Falls, potentially constraining the extent of the E-W paleostress field. This indicates localization of paleostress fields within a small geographic area (Figure 29). Otherwise, the N-S striking fractures appear to be distributed throughout the quadrangle, and can be correlated to the N-S striking dikes as shown by the synoptic equal area projection.

Kindley (2011) proposed the N-S striking joint set as the youngest set found in the Great Gulf Wilderness, as found from the cross-cutting relationship with the other observed joint sets. Both Gardner (2010) and Kindley found N-S striking fractures in the Presidential Range, but no dikes associated with those fractures. Kindley (2011) proposed that the timing of this set could be constrained by an AFT exhumation study done by Roden-Tice et al. (2011). The study showed a period of no cooling around the Mt. Washington summit area between 130-60 Ma, followed by a period of rapid cooling from 60 Ma to present. Kindley (2011) hypothesized that this last stage of unroofing acted as a mechanism of formation of the observed sub-horizontal joint set, thereby making the N-S striking joints older than 60 Ma. Gardner (2010) suggests the potential involvement of a hotspot, as they often have multiple stress fields associated with their creation.

Kindley (2011) offers the explanation of N-S joint formation as a result of uplift variations between coastal New England, the White mountains, and southern Quebec based on the AFT exhumation study performed by Roden-Tice et al. (2012). This study revealed a significant difference in the paleo height of Mt. Washington and Pinkham Notch between 60-120 Ma, such that Pinkham Notch was higher than Mt. Washington (Figure 69). Flanking the White Mountains are major normal fault systems (Ammonoosuc and late stage Norumbega), creating a possible horst system that encompasses the White Mountains (Roden-Tice and Wintsch, 2002; West and Roden-Tice, 2003). Regional tilting occurring between 120 and 60 Ma resulted in uplift of Bronson Hill Terrane rocks (Roden-Tice and Wintsch, 2002). Kindley (2010) proposed that subsequent normal faulting of the Norumbega Fault Zone created a major drainage in Pinkham Notch (West and Roden-Tice, 2003). Kindley then proposed that the flexure of the White Mountain horst resulted in an E-W extensional stress field.

Based on the geochemistry and structural data of this study, one working hypothesis for the formation of the Mill Brook Dike Zone would be hotspot related magmatism taking

advantage of inherited N-S oriented structures from Taconic/Acadian faults. The Mill Brook Dike Zone does not belong to CAMP magmatism as it is geochemically distinct from other large regional mafic intrusions (Figures 68, 69, and 71). The N-S orientation of the dikes indicates intrusion after emplacement of the NEQ province, as the dikes that belong to the NEQ province strike NE-SW (McHone and Butler, 1984). The MBDZ crosscuts the Cherry Mountain syenite, which is Jurassic in age. No cross cutting relationships were observed in the field between the MBDZ and the Jurassic Conway Granite in the SW corner of the quad. Therefore the MBDZ must be younger than the Cherry Mountain pluton and possibly of late Jurassic to Cretaceous in age.

Apatite fission track (AFT) dating of rocks in the northern New Hampshire by Roden-Tice et al. (2009) shows an offset of AFT ages across the Ammonoosuc and Northy Hill faults with older ages (circa 140 Ma) NW of these faults and younger ages SE of the faults (circa 80 Ma). This constrains a period of regional cataclasis and possibly fault-adjacent alteration to sometime < 80Ma. Since the Ammonoosuc and Northy Hill Faults are fairly close to the MDBZ, the cataclasis in the MBDZ might be related to faulting along these structures (Figure 76). Furthermore the silicified zone marking the Pine Peak Fault mapped in the quadrangle is somewhat constrained by its truncation against the Jurassic Conway Granite. If this fault caused the alteration and cataclasis in the MBDZ, that would push the intrusion of the MBDZ back into the Jurassic. This is a less likely scenario given the correlation to the Cretaceous NEQ province for dikes in the nearby Presidential Range that are older than the MBDZ. Hydrothermal alteration is seen throughout the samples, indicated by the presence of amphibole and chlorite (hydrous phases). The paleo-depth of the study area at this time (2 km) suggest that the type of alteration and the cataclasis are as expected at shallow depths

Thus, the age of intrusion of the MBDZ can be constrained to be 100 ± 20 Mya while the

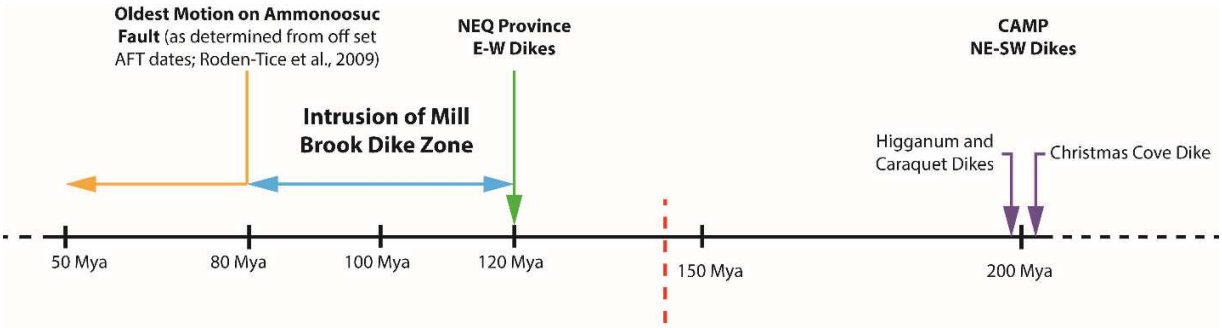

Figure 92: Timeline showing age of tectonic events, regional mafic intrusions, and relative age of intrusion of Mill Brook Dike Zone.

age of alteration and cataclasis appears to be < 80 Ma (Figure 75). Additionally, as per McHone et al.'s (2014) observation, the large regional mafic intrusions have a younging trend from east to west, potentially making the MBDZ one of the younger large mafic intrusions.

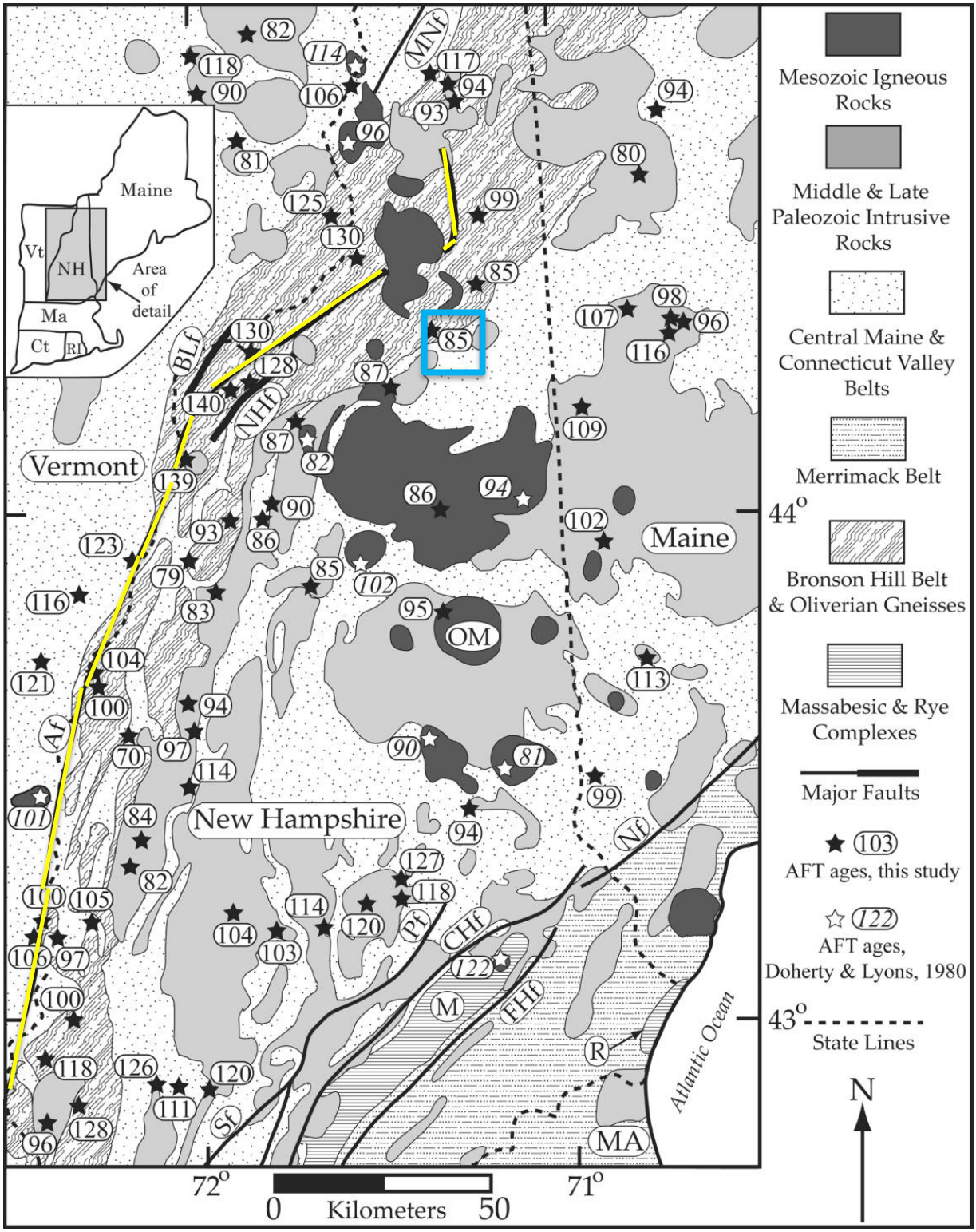

Figure 93: Apatite fission-track ages (Ma) superimposed on generalized geologic map of eastern Vermont, New Hampshire, and western Maine. Ammonoosuc fault is highlighted in yellow, study area is highlighted in blue. (Modified from Roden-Tice et al., 2009).

The AFT data from by Roden-Tice et al. (2009) indicates Early Cretaceous uplift and cooling, which provides legitimacy to the hypothesis of the passage of the North American plate over the Great Meteor hotspot (Crough, 1981; Sleep, 1990). Roden-Tice et al. (2009) also hypothesize the range of Early Cretaceous AFT dates stretching across the majority of northern New Hampshire indicates regional extension and unroofing due to the North American plate's passage over the Great Meteor hotspot. The Great Meteor hotspot is thought to have existed as a plume between 125 and 70 Ma (McHone, 2015). However, the mantle plume hypothesis does not explain all Cretaceous igneous features, as some are scattered far from the supposed track of the hotspot (Figure 77). Additionally, there is no age progression of the intrusions moving offshore (McHone, 2015). McHone (2015) proposes a model that instead attributes the magmatism to a combination of tectonic events and thermal structures of the upper mantle, together these would be responsible for the creation of the observed mafic

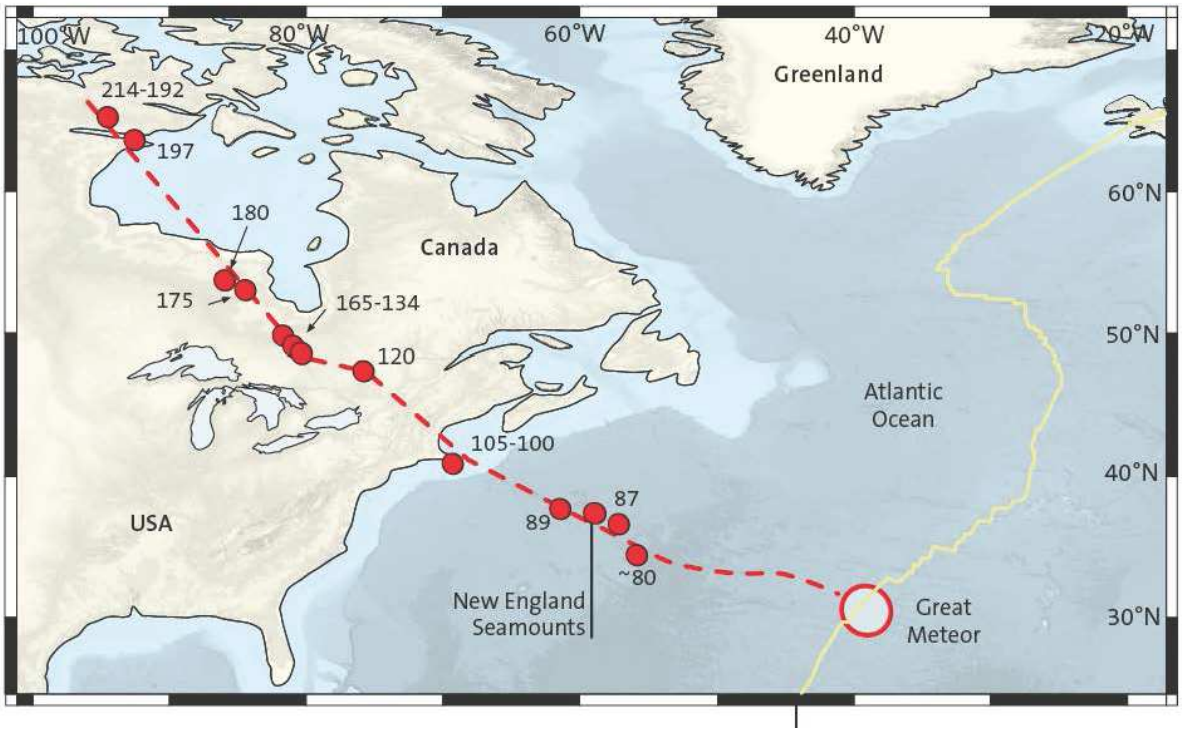

Figure 94: Figure from Frisch et al., (2011) showing interpreted trajectory of the Great Meteor hotspot.

intrusions. This model moves the plume from the core-mantle boundary, and places it closer to the upper mantle.

Another explanation would incorporate part of McHone's (2015) model, and take into consideration the movement of the ocean floor due to the Mid-Atlantic Ridge. The New England Seamount Chain lies along a fracture zone, resulting from a discontinuity of sea-floor spreading (Uchupi et al., 1970). The magma rising from the upper mantle could take advantage of the weakness of the transform faults created by the Mid-Atlantic Ridge, which would allow for magma to intrude along a non-linear path (Figure 79). The offset due to the transform faults would result in subsequent mafic intrusions that would potentially parallel each other in terms of orientation. This model avoids the complication of the age progression, since the magma will intrude at any given time into the weakness in the crust. The model does rely however, on the presence of a thermal anomaly in the upper mantle to create magma. The MBDZ would represent an in-plate continental crustal expression of this model, as it would have been emplaced while the North Atlantic plate was riding over the upper mantle thermal anomaly.

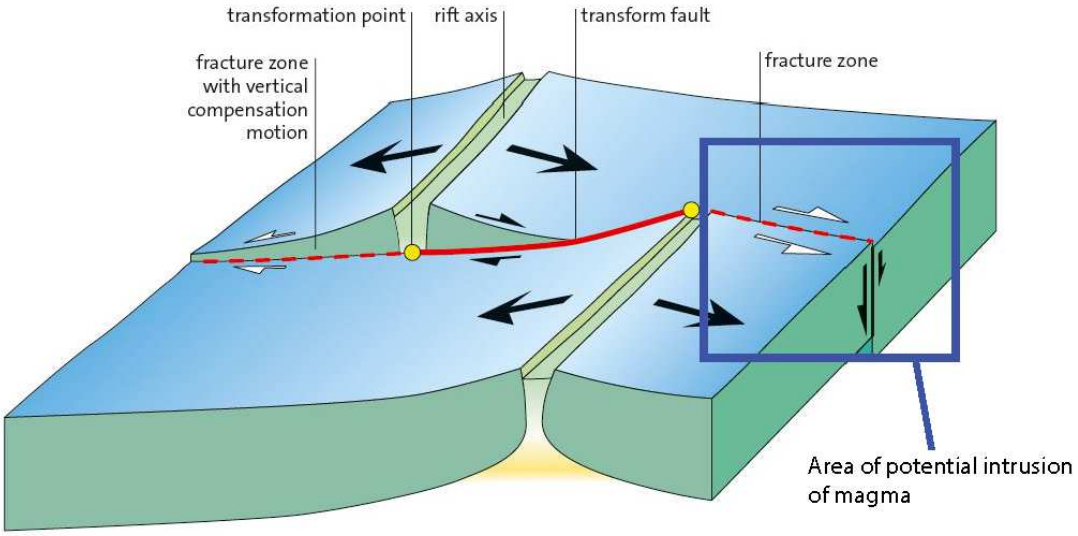

Figure 95: Figure from Frisch et al. (2011) showing the anatomy of a transform fault. Proposed area of magma intrusion highlighted with blue box.

Hotspots and mantle plumes are controversial, and have long been proposed to explain large igneous intrusions and provinces (White and McKenzie, 1989; Beutel et al., 2014; McHone, 2000). In order to more rigorously assess if the MBDZ was created by the Great Meteor hotspot, more field work would need to be done to determine if there is any doming in the study area as is often observed near hotspot intrusions, and further geochemical work should be done to determine if the dike chemistry suggests deep mantle-derived magma. Further fieldwork should also be done to the north of the study area into the Jefferson Quadrangle to determine if the MBDZ extends beyond the Mount Dartmouth quadrangle. This would also help to constrain and refine the understanding of the paleostress around the dike, by indicating whether it is geographically limited to the Mount Dartmouth quadrangle, or can be extended to a larger area.

5. Conclusion

The N-S oriented Mill Brook Dike Zone was previously discovered and analyzed by Fowler-Billings (1944). The rediscovery of this area gives an opportunity to bring the Mill Brook Dike Zone into the modern era of plate tectonics. In particular, this allows for the application of more advanced analytical techniques to dissect the composition and tectonic formation of the MBDZ.

The similar strikes of the various observed intrusions composing the MBDZ indicate a significant tectonic relationship. The Mill Brook Dike Zone appears to be among the youngest mafic intrusions in the Northeast. It is geochemically distinct from other dikes of similar size (i.e. Christmas Cove, Higganum, Caraquet dikes). The MBDZ also crosscuts the Cherry Mountain Syenite, making it younger than the Jurassic. It therefore must have intruded during the early Cretaceous, post-dating CAMP magmatism.

This study also found four separate paleostress fields in the Mount Dartmouth quadrangle, creating the brittle structural features observed throughout the study area. Three of the four paleostress fields were active during the Mesozoic, and the fourth active during the Cenozoic, as determined from cross-cutting relationships. The oldest set was the NE-SW joint set, the second oldest set was the NW-SE striking set, the third oldest was the N-S oriented set. The youngest set are the sheeted joints, which are likely due to glacial unloading. Orientation of σ_3 was determined by calculating the average orientation of poles orthogonal to the observed structures.

There is significant opportunity for future work on the Mill Brook Dike Zone. This includes age dating of MBDZ samples to further constrain the timing of intrusion. More samples could be collected to create a more robust statistical data set to examine geochemical variation, i.e. the AFM ternary diagram. Additional analyses in the form of isotope geochemistry should be done to investigate the formation of the MBDZ in terms of tectonic environment. Finally, further fieldwork into the Jefferson quadrangle to the north should be done to determine the north-south extent of the MBDZ and to gather further samples if possible.

6. References

Adams, J., Kline, M., Richardson, K., Rogers, J., 1962, The Conway granite of New Hampshire as a major low-grade thorium resource: Proceedings Of The National Academy Of Sciences Of The United States Of America, v. 48, p. 1898-1905.

Allen, T., Creasy, J., Davis, P.T., Eusden, J.D., Fowler, B.K., & Thompson, W.B., 2001, The Notches: Bedrock and Surficial Geology of New Hampshire's White Mountains. David P. West and Richard H. Bailey, editors, Guidebook for Geological Field Trips in New England, Geological Society of America, 2001 Annual Meeting. p. 1-33.

Armstrong, R.L., Eisbacher, G.H., Evans, P.D. 1982, Age and stratigraphic-tectonic significance of Proterozoic diabase sheets, Mackenzie Mountains, northwestern Canada: Canadian Journal of Earth Sciences = Revue Canadienne des Sciences de la Terre, v. 19, no. 2, p. 316-323.

Beutel, E.K., Alexander, M., Kotecha, A., Edwards D., 2002, To plume or not to plume: SC Mesozoic diabase dike orientations, stress fields during the break-up of Pangea, and the feasibility of a causal plume: Eos, Transactions, American Geophysical Union, v. 83, p. 1043.

Billings, M. P., Chapman, C. A., Chapman, R. W., Fowler-Billings, K., & Goldthwait, R. P., 1946, The geology of the Mount Washington Quadrangle, New Hampshire: Geological Society of America Bulletin, v. 57, p. 261-273.

Billings, M. P., Fowler-Billings, K., Chapman, C. A., Chapman, R. W. & Goldthwait, R.P., 1979, The Geology of the Mount Washington Quadrangle, New Hampshire, Concord: State of New Hampshire Department of Resources and Economic Development.

Billings, M.P., 1956, The Geology of New Hampshire; Part II, Bedrock Geology: New Hampshire State Planning and Development Commission, American Geological Institute, p. 203.

Bradbury, Savile, Mortimer Abramowitz, and Michael W. Davidson. "Microscope Configuration." Olympus Microscopy Resource Center. Microscope Resource Center. Web. 30 Nov. 2014. <http://www.olympusmicro.com/primer/techniques/polarized/configuration.html>.

Bradley, D, Tucker, R, Lux, D, Harris, A, & McGregor, D 2000, 'Migration of the Acadian Orogen and foreland basin across the Northern Appalachians of Maine and adjacent areas', U. S. Geological Survey Professional Paper

Blackburn, T, Olsen, P, Bowring, S, McLean, N, Kent, D, Puffer, J, McHone, G, Rasbury, E, & Et-Touhami, M 2013, 'Zircon U-Pb geochronology links the end-Triassic extinction with the Central Atlantic magmatic province', Science, 340, 6135, pp. 941-945,

Burke, K.B.S., Hamilton, J.B., and Gupta, V.K. 1973. The Caraquet Dyke: Its Tectonic Significance: Canadian Journal of Earth Sciences, 10, pp. 1760–1768.

Callegaro, Sara, Marzoli A., Bertrand H., Chiaradia M., Reisberg L., Meyzen C., Bellieni G., Weems R.E., Merle R., 2013, Upper and lower crust recycling in the source of CAMP basaltic dykes from southeastern North America: Earth And Planetary Science Letters v. 376, p.186-199.

Castro, C., 2010, Paleostress Analysis of Mesozoic Fractures and Basalt Dikes in Tuckerman Ravine, NH, Bates Geology Thesis.

Chapman, R.W., 1937, Petrology of the syenite stock at Cherry Mountain, New Hampshire: American Journal Of Science, v. 33, p. 174-186.

Choe, Saebyul C., 2014, Petrographic Analysis and Tectonic Implications of the Plutons in the Gilead 7.5 Quadrangle: Connections to the Piscataquis Volcanic Arc and Sebago Batholith, Bates Geology Thesis

.

Creasey, S.C., 1966, Hydrothermal alterations. Titley, S.R. and Hicks, C.L., (Eds.), Geology of the Porphyry Copper Deposits, Southwestern North America: University of Arizona Press, p. 51-74.

Creasy, J.W., and Eby, N., 1983, The White Mountain Batholith as a model of Mesozoic felsic magmatism in New England: Abstracts With Programs - Geological Society Of America v. 15, p. 549.

Crough, S.T., 1981, Mesozoic hotspot epeirogeny in eastern North America: Geology v. 9, no. 1, p. 2-6.

Best, M.G., 1982, Igneous and Metamorphic Petrology. San Francisco: Freeman. Print.

Davis, G. H., 1984, Structural Geology of Rocks and Regions. New York: Wiley. Print.

Dorais, Michael J., Wintsch, R.P., Nelson, W., Tubrett, M., 2009, Insights Into The Acadian Orogeny, New England Appalachians; A Provenance Study Of The Carrabassett And Kittery Formations, Maine: Atlantic Geology, v. 45, p. 50-71.

Dunlap, M., and Adaskaveg, J. E.. "Introduction to the Scanning Electron Microscope Theory, Practice, & Procedures." SEM/EDS Manual (n.d.): University of California Merced, 1 Jan. 2001. Web. 30 Nov. 2014. <https://imf.ucmerced.edu/>.

Dunn, A.M., Reynolds, P.H., Clarke, D.B., & Ugidos, J.M.,1998, A comparison of the age and composition of the Shelburne dyke, Nova Scotia, and the Messejana dyke, Spain: Canadian Journal of Earth Sciences, 35, p. 1110–1115.

Dupee, M., Minor, J., Eusden, J.D., 2002, Continued Bedrock Geologic Mapping in the Presidential Range, N.H.: A progress report for EDMAP 2001: Geological Society of America Abstracts with Programs, v. 34, p. A-68.

Eby, G.N., Krueger H.W., & Creasy, J.W., 1992, Geology, geochronology, and geochemistry of the White Mountain Batholith, New Hampshire: Special Paper - Geological Society Of America v. 268, p. 379-397.

Eusden J., de Garmo, A., Friedman, P., Garesche, J., Gaynor, A., Granducci, J., Johnson, A.H., Maconochie, J., Peters, S.P., O'Brien, J.B., & Widmann, B.L., 1996b, Bedrock geology of the Presidential Range, New Hampshire: Guidebook to field trips in northern New Hampshire and adjacent regions of Maine and Vermont: Harvard University, Cambridge, MA, p. 59-78.
Eusden, Dykstra, Anderson, K., Beaudry, E., Dupee, M., Larkin, R., Minor, J., & Weling, D., 2006, Domes, Volcanics, Migmatites, Refolded Folds And Granites; A Transect From The Bronson Hill Arc Into The Central Maine Cover, Northern Presidential Range, New Hampshire: Annual Meeting - New England Intercollegiate Geological Conference v. 98, p. 167-180.

Eusden, J. Dykstra, Jr., Garesche, J.M., Johnson, A.H., Maconochie, J., Peters, S.P., O'Brien, J.B., & Widmann, B.L., 1996a, Stratigraphy And Ductile Structure Of The Presidential Range, New Hampshire; Tectonic Implications For The Acadian Orogeny: Geological Society Of America Bulletin v. 108, p. 417-436.

Eusden, J.D., and Lux, D.R., 1994, Slow late Paleozoic exhumation in the Presidential Range of New Hampshire as determined by the 40Ar/39Ar relief method: Geology, v. 22, no. 10, p. 909-912.

Eusden, John Dykstra. The Presidential Range: Its Geologic History and Plate Tectonics. Lyme, NH: Durand, 2010. Print.

Faure, S., Tremblay, A., & Angelier, J., 1996a, Alleghanian paleostress reconstruction in the Northern Appalachians; intraplate deformation between Laurentia and Gondwana: Geological Society of America Bulletin, v. 108, no. 11, p. 1467-1480.

Faure, S., Tremblay, A., & Angelier, J., 1996b, State of intraplate stress and tectonism of northeastern America since Cretaceous times, with particular emphasis on the New England-Quebec igneous province: Tectonophysics, v. 255, no. 1-2, p. 111-134.

Faure, S., Tremblay, A., Malo, M., & Angelier, J., 2006, Paleostress analysis of Atlantic crustal extension in the Quebec Appalachians: Journal of Geology, v. 114, no. 4, p. 435-448.

Fitton, J.G., 2007, The OIB paradox: Special Paper - Geological Society of America, v. 430, p. 387-412.

Foland, K. A., Faul, H., 1977, Ages of the White Mountain intrusives; New Hampshire, Vermont, and Maine, USA: American Journal Of Science v. 277, p. 888-904.

Foley, M.B., Eusden, J.D., 2009, Contact relations between the Ammonoosuc Volcanics and Jefferson Dome, northern NH: Abstracts With Programs - Geological Society Of America v. 41, p. 79.

Fowler-Billings, K., 1944, Igneous and Metasedimentary Dikes of the Mt. Washington Area, New Hampshire, Bulletin of the Geological Society of America, v. 56, p. 1255-1278.

Gardner, P., 2010, Mesozoic Extension in the Presidential Range, Huntington Ravine, NH, Bates Geology Thesis.

Haase, K.M., Stoffers, P., Garbe-Schoenberg, C.D., 1997, The petrogenetic evolution of lavas from Easter Island and neighbouring seamounts, near-ridge hotspot volcanoes in the SE Pacific: Journal of Petrology, v. 38, no. 6, p. 785-813.

Hames, W. E., McHone J.G., Renne, P.R., Ruppel, C., 2003, The Central Atlantic Magmatic Province; insights from fragments of Pangea: Geophysical Monograph v.136.

Hames, W. E., Renne P. R., and Ruppel C., 2000, New evidence for geologically instantaneous emplacement of earliest Jurassic Central Atlantic magmatic province basalts on the North American margin: Geology v.28, p. 859-862.

Hanson, L.S., Bradley, D.C., 1993, Late Silurian to Early Devonian paleogeography of the Kearsage-Central Maine Basin revealed by paleocurrents and sedimentary facies: Abstracts with Programs – Geological Society of America, v. 25, no. 6, p. 360.

Hatch, N. L. & Moench, R. H., 1984. Bedrock Geologic Map of the Wilderness and Roadless Areas of the White Mountain National Forest, Coos, Carroll, and Grafton Counties, New Hampshire. United States Geologic Survey, Miscellaneous Investigations Map MF–1594–A.
Hatcher, R.D., 2010, The Appalachian Orogen; A Brief Summary: Memoir - Geological Society Of America v. 206, p. 1-19.

Henderson, D. M., Billings, M.P., Creasy, J.W., Wood, S.A., 1977, Geology of the Crawford Notch Quadrangle, New Hampshire. United States: N. H. Department. Resources and Economic Development, Concord, N. H., United States. P1-29.

Hibbard, J., van Staal, C., and Rankin, D., 2007, A comparative analysis of pre-Silurian crustal building blocks of the northern and the southern Appalachian orogeny: American Journal fo Science, v. 207, no. 1, p. 23-45.

Irvine, T.N., Baragar, W.A., 1971, A guide to the chemical classification of the common volcanic rocks: Canadian Journal of Earth Sciences = Revue Canadienne des Sciences de la Terre, v. 8, no. 5, p. 523-548.

Jourdan, F., Marzoli, A., Bertrand, H., Cirilli, S., Tanner, L., Kontak, D., McHone, G., Renne, P., and Bellieni, G., 2009, 40Ar/39Ar ages of CAMP in North America: Implications for the Triassic-Jurassic boundary and the 40K decay constant bias: Lithos., v. 110, no. 1-4, p. 167-180.

Kamb, W.B., 1959, Ice petrofabric observations from Blue Glacier, Washington, in relation to theory and experiment: Journal of Geophysical Research, v. 64, no. 11, p. 1891-1909.

Karabinos, P., Samson, S.D., Hepburn, J.C., Stoll, H.M., 1998, Taconian Orogeny In The New England Appalachians; Collision Between Laurentia And The Shelburne Falls Arc: Geology v. 26, p. 215-218.

Kindley, C., 2011, Paleostress Analysis of Mesozoic Extension in Fractures and Basalt Dikes, Great Gulf, NH, Bates Geology Thesis.

Klein, C., Hurlbut, C.S. Jr., 1986, Manual of Mineralogy: Wiley, 20th ed., p. 483.
Larkin, R.R., Eusden, J.D., 2004, Electron microprobe age dating of monazite from the Bretton Woods Pluton, Presidential Range, New Hampshire: Abstracts With Programs - Geological Society Of America v. 36, p. 152.

LeTourneau, P.M., Olsen, P.E., 2003, The Great Rift Valleys Of Pangea In Eastern North America: Volume 2, Sedimentology, Stratigraphy, And Paleontology; Introduction: Columbia University Press: New York, NY, United States, p. 1-4.

Lowell, J.D., Guilbert, J.M., 1970, Lateral and vertical alteration - mineralization zoning in porphyry copper deposits: Economic Geology, v. 65, p. 373 -408.

Lowell, J.D., Guilbert, J.M., 1970, Lateral and vertical alteration - mineralization zoning in porphyry copper deposits: Economic Geology, v. 65, p. 373 -408.

Lyons, J.B., Bothner, W.A., Moench, R.H., & Thompson Jr., J.B., 1997, Bedrock geologic map of New Hampshire: US Geological Survey, scale 1:250,000.

McHone, J. G., 2000, Non-Plume Magmatism And Rifting During The Opening Of The Central Atlantic Ocean: Tectonophysics, v. 316, p. 287-296.

McHone, J.G., 1988, Tectonic and paleostress patterns of Mesozoic intrusions in eastern North America: Elsevier : Amsterdam, Netherlands.

McHone, J.G., 1988, Tectonic and paleostress patterns of Mesozoic intrusions in eastern North America, in Manspeizer, W.R., ed., Triassic-Jurassic Rifting: Continental Breakup and the Origin of the Atlantic Ocean and Passive Margins, Part B: New York, Elsevier, p. 607-619.

McHone, J.G., 2015, Do deep mantle plumes explain the Mesozoic igneous features of New England?, Geological Society of America, Abstracts with Programs, v. 47, p. 122.
McHone, J.G., Anderson, D.L., Beutel, E.K., Fialko, Y.A., 2005, Giant dikes, rifts, flood basalts, and plate tectonics; a contention of mantle models: Special Paper - Geological Society Of America v.388, p. 401-420.

McHone, J.G., Butler, J.R., 1984, Mesozoic igneous provinces of New England and the opening of the North Atlantic Ocean: Geological Society Of America Bulletin v. 95, p. 757-765.

McHone, J.G., Hussey II, A.M., West Jr., D.P., Bailey, D.G., 2014, The Christmas Cove Dyke of coastal Maine, USA, and regional sources for Early Mesozoic flood basalts in northeastern North America: Atlantic Geology, v. 50, p. 66-90.

McHone, J.G., Ross, M.E., Greenhough, J.D., 1987, Mesozoic dyke swarms of eastern North America: Special Paper - Geological Association Of Canada v. 34, p. 279-288.

Merle, R., Marzoli, A., Reisberg, L., Bertrand, H., Nemchin, A. A., Chiaradia, M., Callegaro, S., Jourdan, F., Bellieni, G., Kontak, D., Puffer, J., & McHone, J. G., 2014, Sr, Nd, Pb and Os isotope systematics of CAMP tholeiites from eastern North America (ENA); evidence of a subduction-enriched mantle source: Journal Of Petrology, v. 55, p. 133-180.

Moench, R.H., Aleinikoff, J.N., 2002, Stratigraphy, geochronology, and accretionary terrane settings of two Bronson Hill arc sequences, northern New England: Physics and Chemistry of the Earth, v. 27, no. 1-3, p. 47-95.

Nesse, William D, 2000, Introduction to Mineralogy: New York, Oxford University Press. Print.

Olsen, P.E., 1997, Stratigraphic record of the early Mesozoic breakup of Pangea in the Laurasia-Gondwana Rift System: Annual Review of Earth & Planetary Sciences, v. 25, no. 1, p. 337.

Palfy, J., Kocsis, A.T., 2014, Volcanism of the Central Atlantic magmatic province as the trigger of environmental and biotic changes around the Triassic-Jurassic boundary: Special Paper - Geological Society Of America, v. 505, p. 245-261.

Pearce, J.A., 1983, Role of Sub-continental Lithosphere in Magma Genesis at Active Continental Margins, In Hawkesworth, C.J., and Norry, M.J., (Eds.), Continental Basalts and Mantle Xenoliths, Nantwich, Cheshire. Shiva Publication, 230-249.

Pearce, J.A., Cann, J.R., 1973, Tectonic setting of basic volcanic rocks determined using trace element analyses: Earth and Planetary Science Letters, v. 19, no. 2, p. 290-300.

Pearce, J.A., Cann, J.R., 1973, Tectonic setting of basic volcanic rocks determined using trace element analyses: Earth and Planetary Science Letters, v. 19, no. 2, p. 290-300.

Petcovic, H., Dufek, J., 2005, Modeling magma flow and cooling in dikes; implications for emplacement of Columbia River flood basalts: Journal Of Geophysical Research, v. 110, p. B10.

Philpotts, A.R., Asher, P.M., 1993, Wallrock melting and reaction effects along the Higganum diabase dike in Connecticut: contamination of a continental flood basalt feeder: Journal of Petrology, v. 34, p. 1029–1058.

Puffer, J. H., 2001, Contrasting high field strength element contents of continental flood basalts from plume versus reactivated-arc sources: Geology v. 29, p. 675-678.

Puffer, J.H., 2003, A reactivated back-arc source for CAMP magma, *in* Hames, W.E., McHone, J.G., Renne, P., and Ruppel, C. eds., The Central Atlantic Magmatic Province: Insights from

Fragments of Pangea, American Geophysical Union: Washington, DC, United States, United States, p. 151-162.

Puffer, John H, 2003, A reactivated back-arc source for CAMP magma: Geophysical Monograph v. 136, p. 151-162.

Ray, J., Gautam S., Biswajit G., 2011, Topics in Igneous Petrology. Dordrecht: Springer Science Business Media B.V. Print.

Reusch, D.N., van Staal, C.R., 2012, The Dog Bay-Liberty Line and its significance for Silurian tectonics of the Northern Appalachian Orogen: Canadian Journal Of Earth Sciences = Revue Canadienne Des Sciences De La Terre v.49, p. 239-258.

Roden-Tice M., West D., Potter J., Raymond S., Winch J., 2009, Presence of a long-term lithospheric thermal anomaly; evidence from apatite fission-track analysis in northern New England: Journal Of Geology, v.117, p. 627-641.

Roden-Tice, M.K., Eusden J.D., Wintsch, R.P., 2012, Apatite fission-track evidence for the Cretaceous development of kilometer scale relief and steady state Tertiary topography in New England: Geomorphology v. 141-142, p. 114-120.

Roden-Tice, M.K., Wintsch, R.P., 2002, Early Cretaceous normal faulting in southern New England; evidence from apatite and zircon fission-track ages: Journal of Geology, v. 110, no. 2, p. 159 - 178.

Rose, A.N., 1970, Zonal relations of wall rock alteration and sulfide distribution of porphyry copper deposits: Economic Geology, v. 65, p. 205-20.

Schlische, R.W., Withjack M.O., Olson, P.E., 2003, Relative timing of CAMP, rifting, continental breakup, and basin inversion; tectonic significance: Geophysical Monograph v. 136, p. 33-59.

Schlische, Roy W., Martha Oliver Withjack, and Paul E. Olson. 2003. "Relative timing of CAMP, rifting, continental breakup, and basin inversion; tectonic significance." Geophysical Monograph 136, 33-59.

Scotese, C.R., 2010, Paleomap Project: http://www.scotese.com.

Sears, J.W., 2007, Lithospheric Control Of Gondwana Breakup; Implications Of A Trans-Gondwana Icosahedral Fracture System: Special Paper - Geological Society Of America v. 430, p. 593-601.

Shen, S, Crowley, J, Wang, Y, Bowring, S, Erwin, D, Sadler, P, Cao, C, Rothman, D, Henderson, C, Ramezani, J, Zhang, H, Shen, Y, Wang, X, Wang, W, Mu, L, Li, W, Tang, Y, Liu, X, Liu, L, Zeng, Y, Jiang, Y, & Jin, Y 2011, 'Calibrating the end-Permian mass extinction', Science, 334, 6061, pp. 1367-1372

Sleep, N. H., 1990, Monteregian hotspot track; a long-lived mantle plume: Journal Of Geophysical Research, v. 95, p. 21.

Stewart, D., Wright, B., Unger, J., Phillips, J., & Hutchinson, D., 1997, Global geoscience transect 8: Quebec-Maine-Gulf of Maine transect, Southeastern Canada, Northeastern United States of America: US Geological Survey, Global Geoscience Transects.

Storey, B.C., Leat, P.T., Ferris, J.K., 2001, The location of mantle-plume centers during the initial stages of Gondwana breakup: Special Paper - Geological Society Of America v. 352, p. 71-80.

Tremblay, A., Pinet, N., 2005, Diachronous Supracrustal Extension In An Intraplate Setting And The Origin Of The Connecticut Valley-Gaspe And Merrimack Troughs, Northern Appalachians: Geological Magazine v. 142, p. 7-22.

Uchupi, E., Phillips, J.D., Prada, K.E. 1971, Origin and structure of the New England Seamount Chain: Collected Reprints - Woods Hole Oceanographic Institution, v. Part 2, no. 2374.

West, D.P., Roden-Tice, M.K., 2003, Late Cretaceous reactivation of the Norumbega fault zone, Maine; evidence from apatite fission-track ages. Geology [Boulder], v. 31, no. 7, p. 649-652.

White, W.M., 2010, Oceanic Island Basalts and Mantle Plumes: The Geochemical Perspective: Annual Review of Earth and Planetary Sciences, v. 38.1, p. 133-160.

Whiteside, J.H., Olsen, P.E., Kent, D.V., Fowell, S.J., Et-Touhami, M., 2007, Synchrony between the Central Atlantic Magmatic Province and the Triassic-Jurassic mass-extinction event?: Palaeogeography, Palaeoclimatology, Palaeoecology v. 244, p. 345-367.
Winter, John D., 2010, Principles of Igneous and Metamorphic Petrology. Second Edition ed. New York: Prentice Hall. Print.

7. Appendix

Below are spectra collected with SEM/EDS. The sample number is noted at the top, along with the point sample it represents (i.e. Sample 108B(1)_pt1 refers to point one of sample 108B). Quantative raw data collected with the SEM/EDS are reported at the end, only selected points (those thought to have the most bearing on understanding the mineralogy of the MBDZ) were

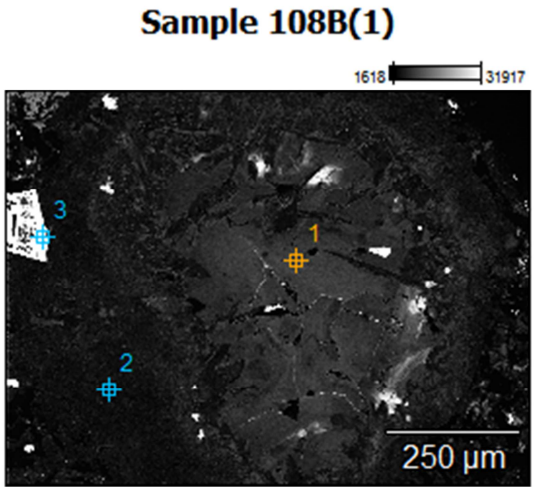

exported from the NSS program to be used for this thesis.

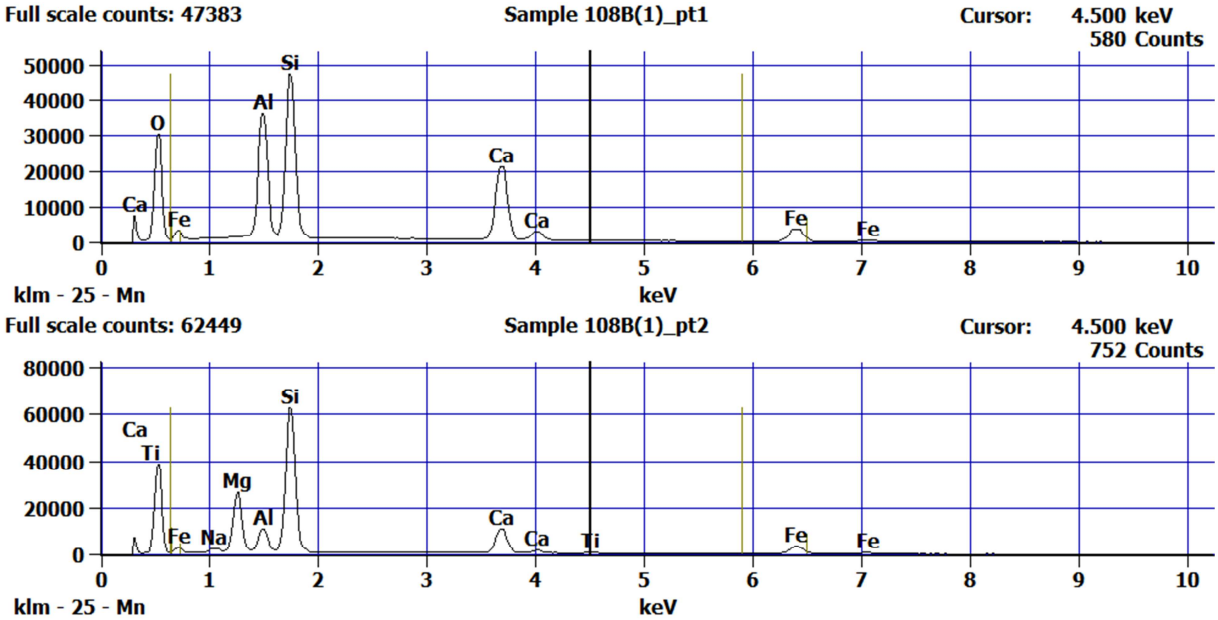

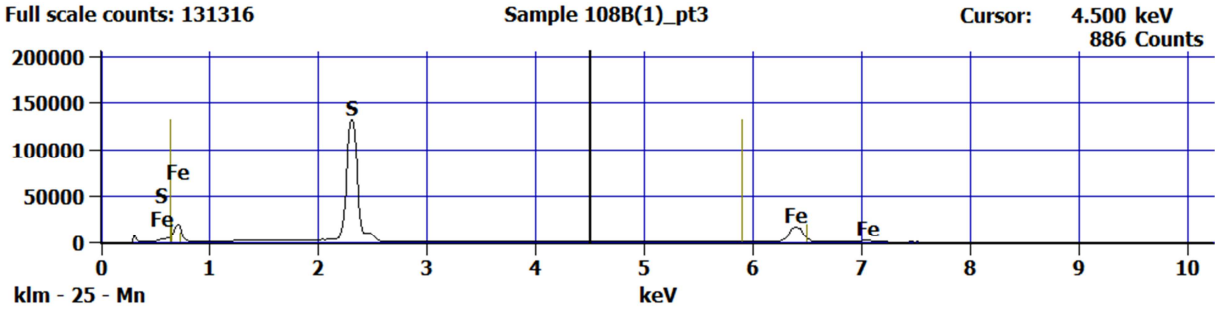

Sample 131B(1)

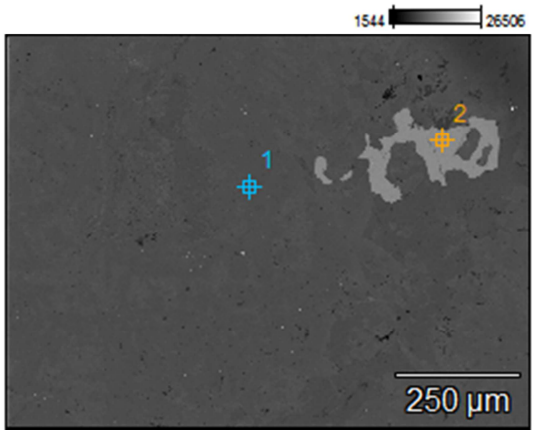

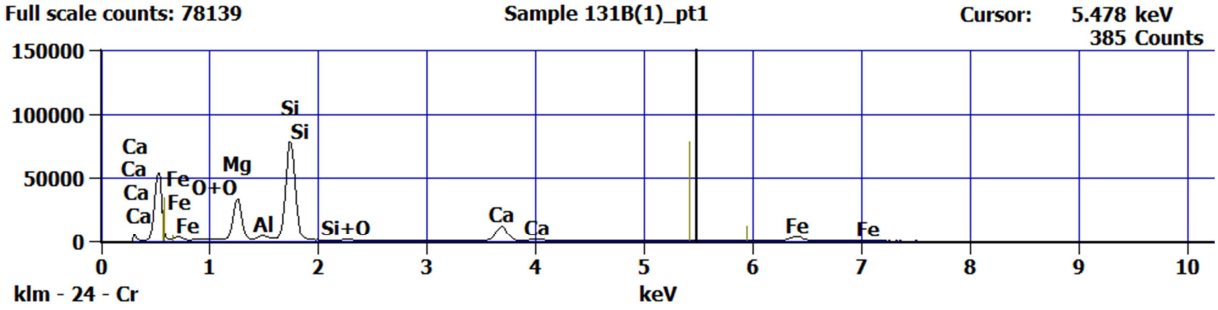

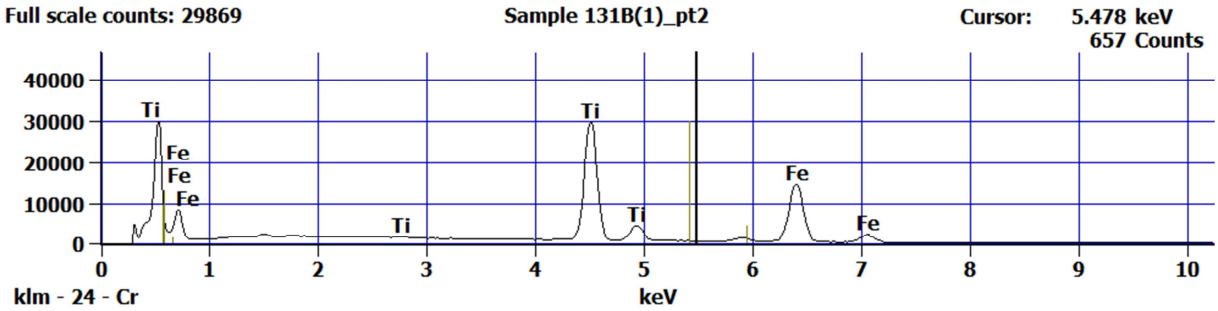

Sample 131B(3)

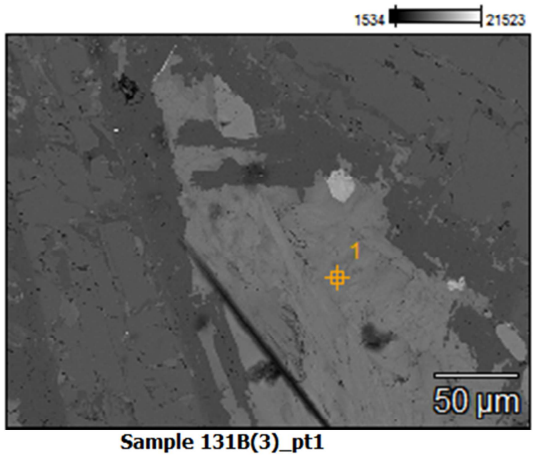

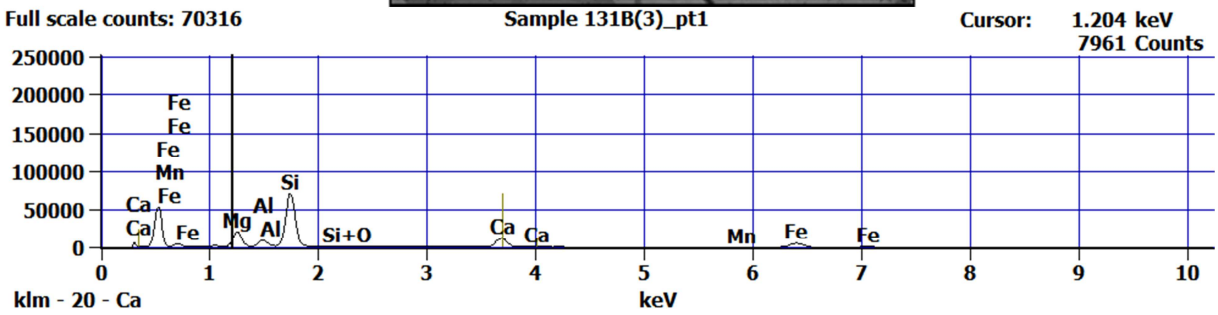

Sample 131B(4)

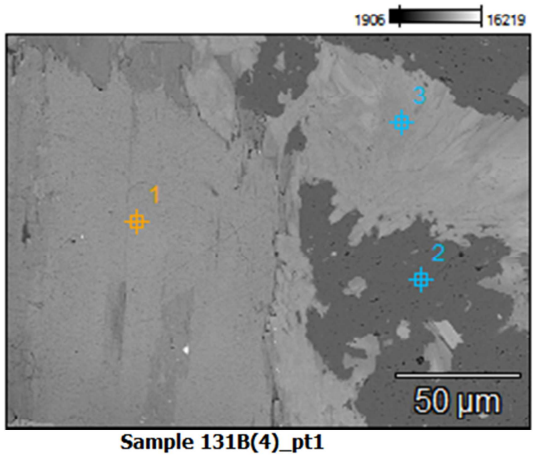

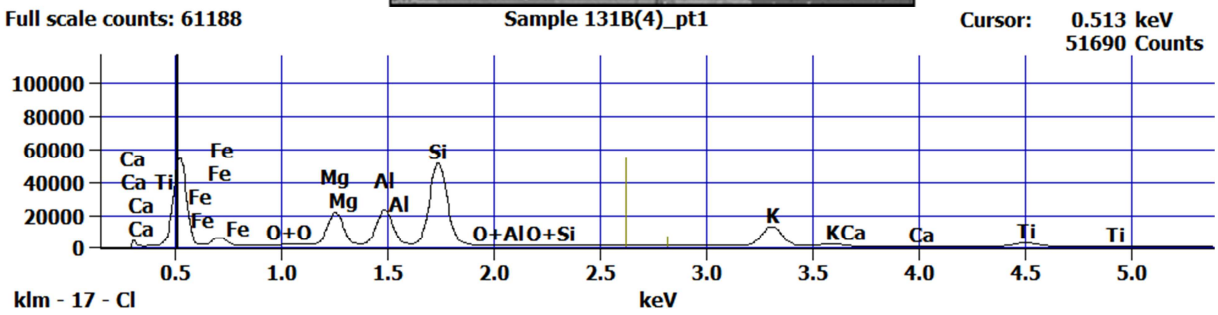

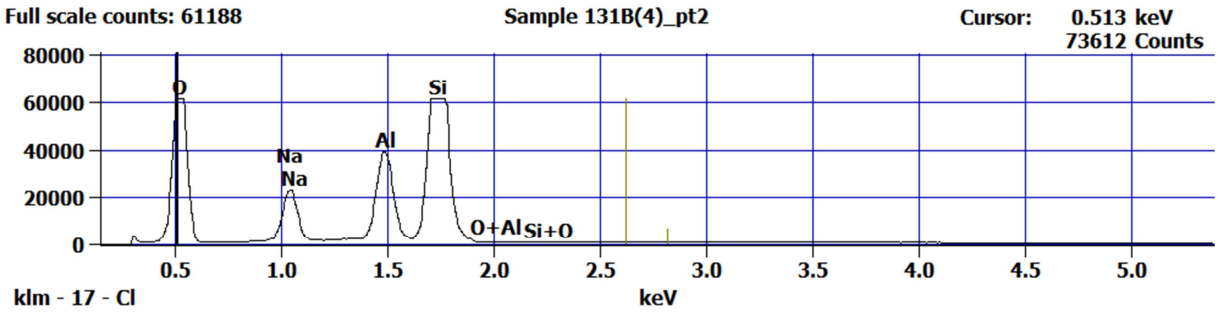

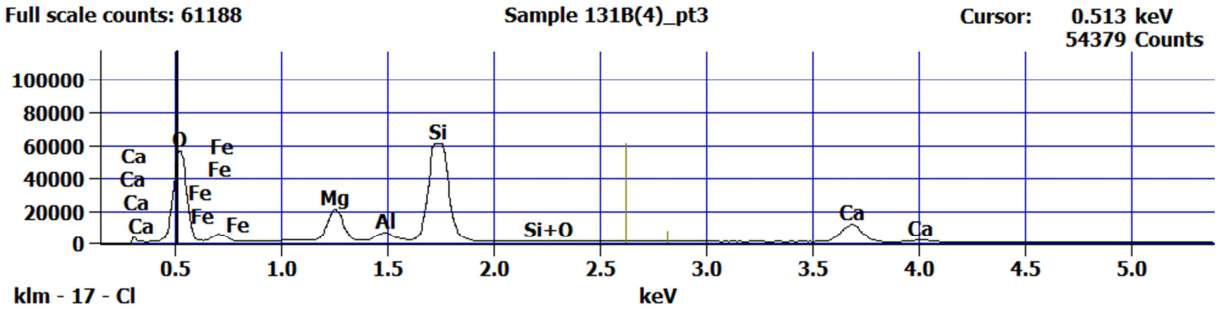

Sample 52B(3)

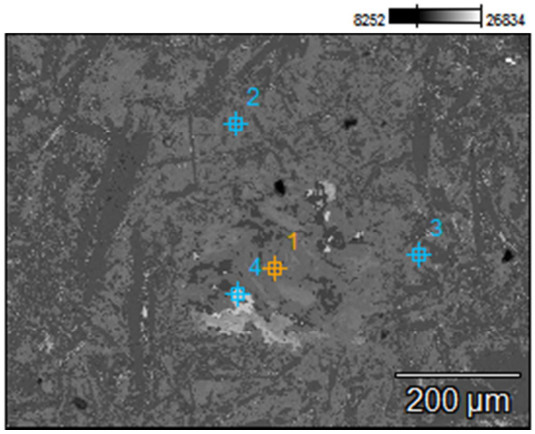
8252
26834
2
1
3
4
200 µm

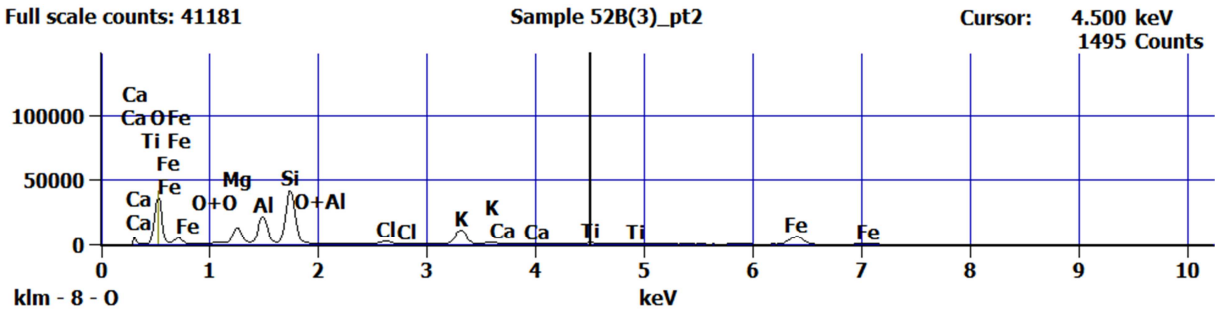
Full scale counts: 41181
Sample 52B(3)_pt2
Cursor: 4.500 keV
1495 Counts
100000
50000
0
Ca
Ca O Fe
Ti Fe
Fe
Fe
Ca
Ca
Fe
O+O
Mg
Al
Si
O+Al
Cl Cl
K
K
Ca Ca
Ti Ti
Fe
Fe
0 1 2 3 4 5 6 7 8 9 10
klm - 8 - O
keV

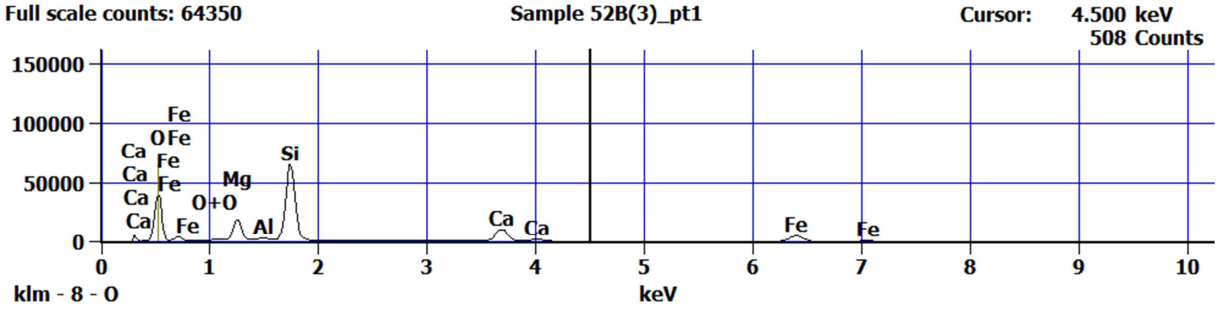
Full scale counts: 64350
Sample 52B(3)_pt1
Cursor: 4.500 keV
508 Counts
150000
100000
50000
0
Fe
Ca O Fe
Ca Fe
Ca Fe
Ca
Fe
O+O
Mg
Al
Si
Ca Ca
Fe
Fe
0 1 2 3 4 5 6 7 8 9 10
klm - 8 - O
keV

Sample 52B(3)

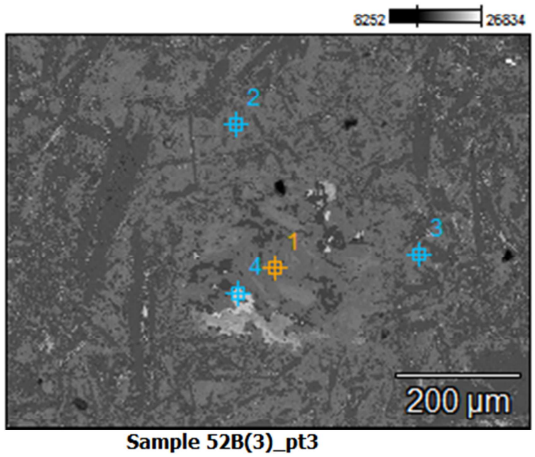
8252
26834
2
1
3
4
200 µm

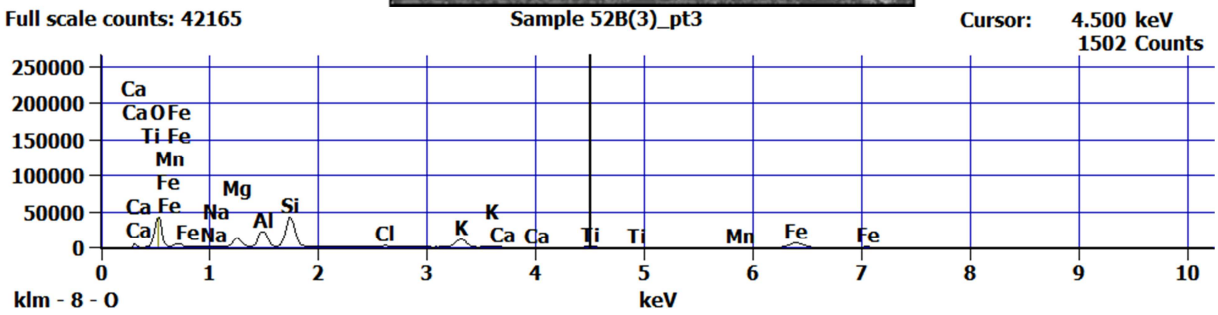
Full scale counts: 42165
Sample 52B(3)_pt3
Cursor: 4.500 keV
1502 Counts
250000
200000
150000
100000
50000
0
Ca
Ca O Fe
Ti Fe
Mn
Fe
Mg
Ca Fe
Na
Si
Ca Fe
Na
Al
Cl
K
K
Ca Ca
Ti
Ti
Mn
Fe
Fe
0 1 2 3 4 5 6 7 8 9 10
klm - 8 - O
keV

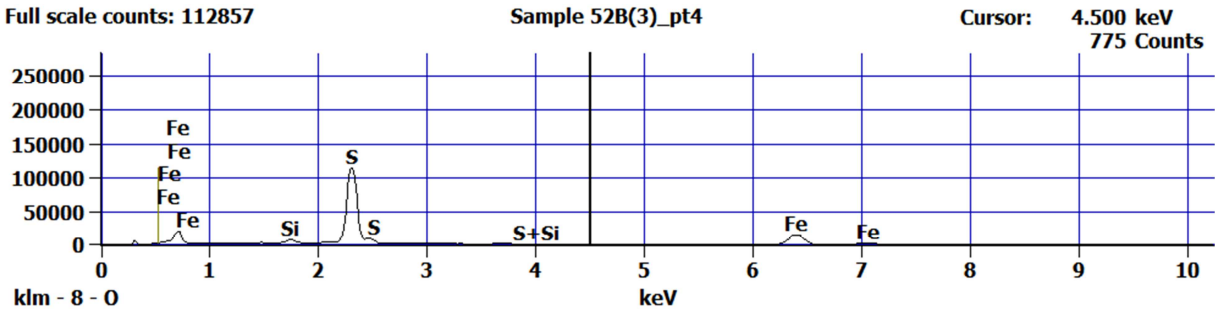
Full scale counts: 112857
Sample 52B(3)_pt4
Cursor: 4.500 keV
775 Counts
250000
200000
150000
100000
50000
0
Fe
Fe
Fe
Fe
Fe
S
Si
S
S+Si
Fe
Fe
0 1 2 3 4 5 6 7 8 9 10
klm - 8 - O
keV

Sample 58B(1)

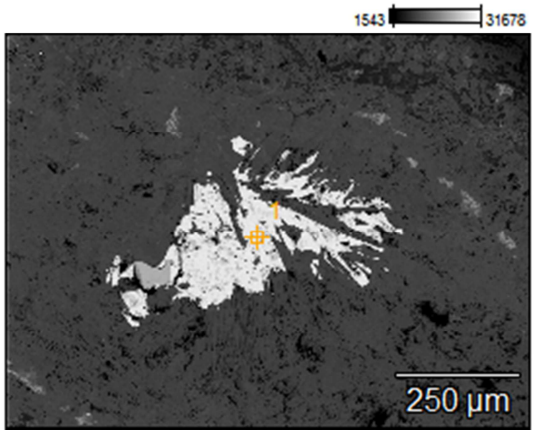
1543
31678
1
250 µm

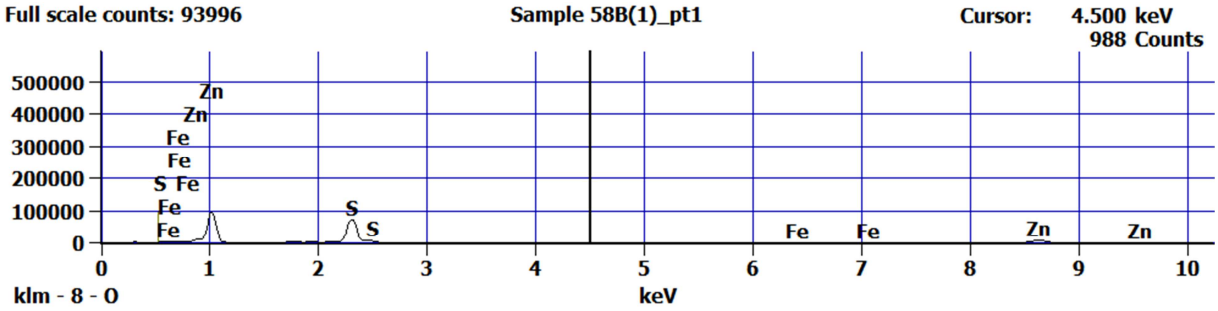
Full scale counts: 93996
Sample 58B(1)_pt1
Cursor: 4.500 keV
988 Counts
500000
400000
300000
200000
100000
0
Zn
Zn
Fe
Fe
S Fe
Fe
Fe
S
S
Fe
Fe
Zn
Zn
0
1
2
3
4
5
6
7
8
9
10
klm - 8 - O
keV

Sample 58B(2)

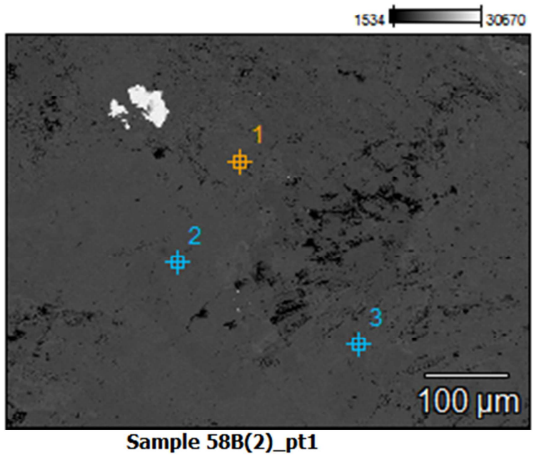
1534
30670
1
2
3
100 µm

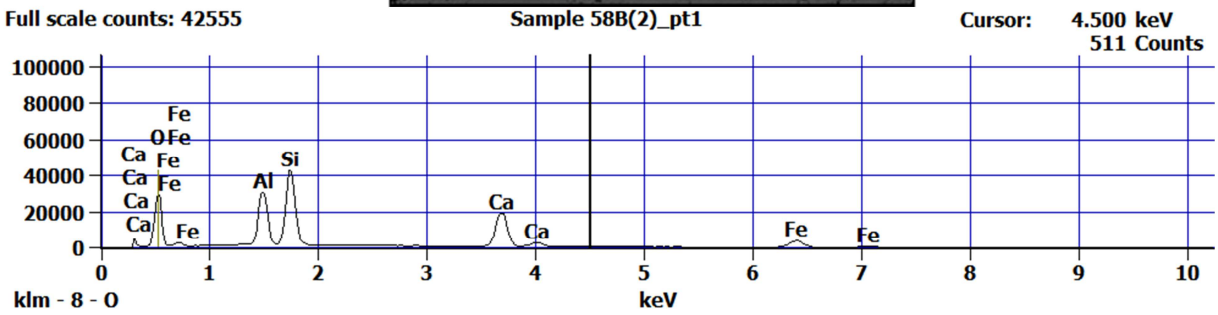
Full scale counts: 42555
Sample 58B(2)_pt1
Cursor: 4.500 keV
511 Counts
100000
80000
60000
40000
20000
0
Fe
O Fe
Ca
Fe
Ca
Fe
Ca
Si
Al
Ca
Fe
Ca
Ca
Fe
Fe
0 1 2 3 4 5 6 7 8 9 10
klm - 8 - O
keV

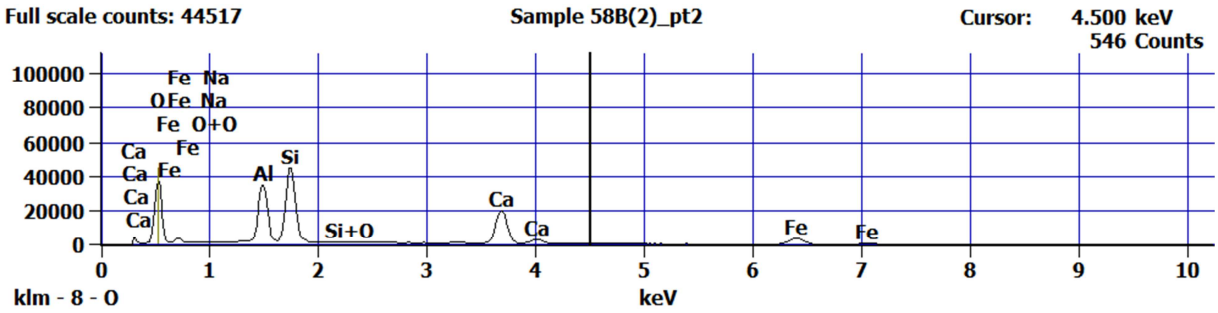
Full scale counts: 44517
Sample 58B(2)_pt2
Cursor: 4.500 keV
546 Counts
100000
80000
60000
40000
20000
0
Fe Na
O Fe Na
Fe O+O
Ca
Fe
Ca
Fe
Ca
Si
Al
Ca
Si+O
Ca
Ca
Fe
Fe
0 1 2 3 4 5 6 7 8 9 10
klm - 8 - O
keV

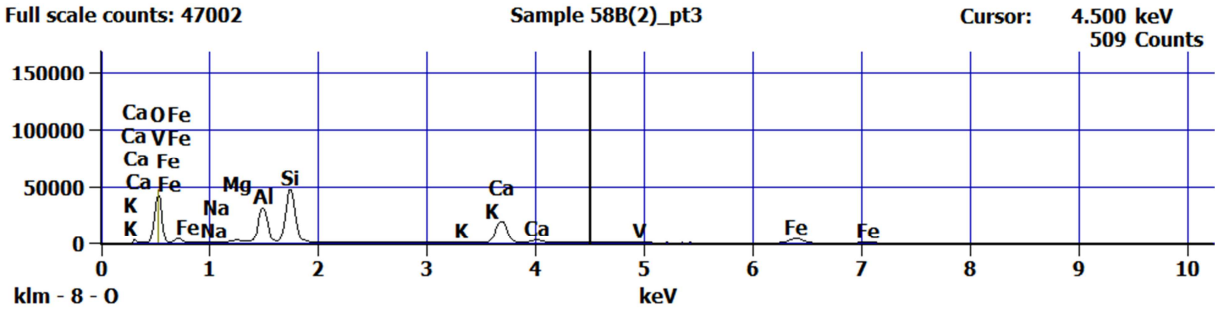
Full scale counts: 47002
Sample 58B(2)_pt3
Cursor: 4.500 keV
509 Counts
150000
100000
50000
0
Ca O Fe
Ca V Fe
Ca Fe
Ca Fe
K
K
Fe
Mg
Na
Na
Al
Si
Ca
K
K
Ca
V
Fe
Fe
0 1 2 3 4 5 6 7 8 9 10
klm - 8 - O
keV

Sample G4A(2)

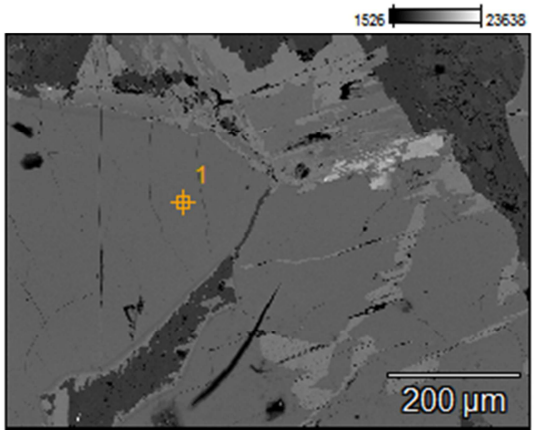
1526
23638
1
200 µm

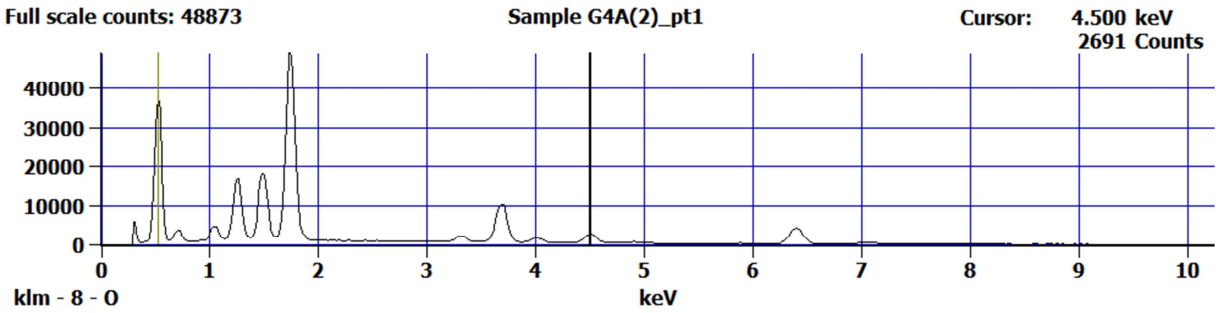
Full scale counts: 48873
Sample G4A(2)_pt1
Cursor: 4.500 keV
2691 Counts
40000
30000
20000
10000
0
0
1
2
3
4
5
6
7
8
9
10
klm - 8 - O
keV

Sample G4A(3)

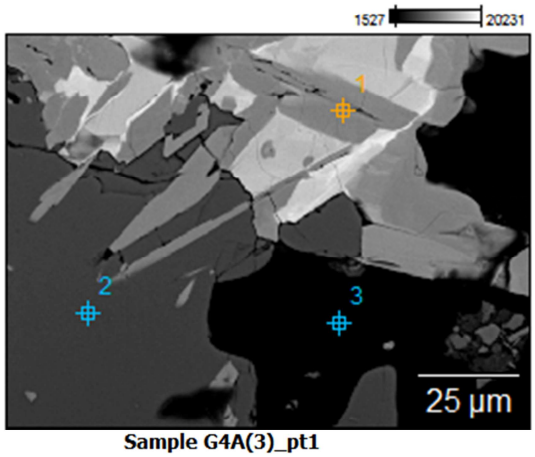
1527
20231
1
2
3
25 µm

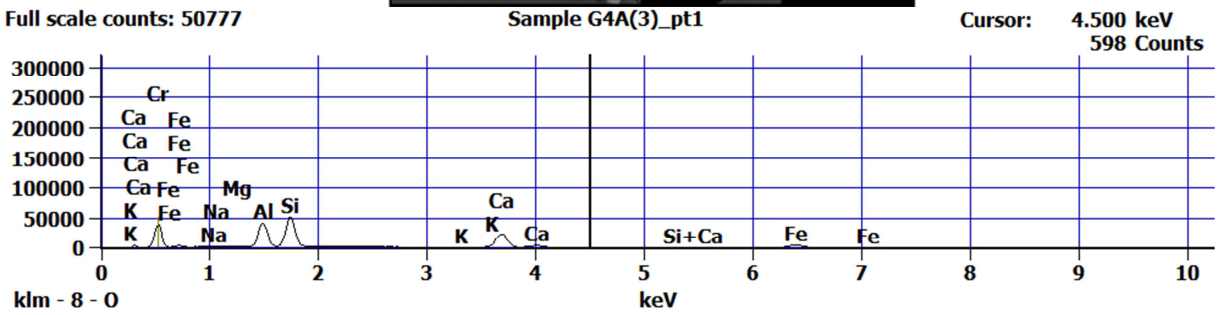
Full scale counts: 50777
Sample G4A(3)_pt1
Cursor: 4.500 keV
598 Counts
300000
250000
200000
150000
100000
50000
0
Cr
Ca Fe
Ca Fe
Ca Fe
Ca Fe
K Fe
K
Mg
Na
Na
Al
Si
Ca
K
Ca
K
Si+Ca
Fe
Fe
0 1 2 3 4 5 6 7 8 9 10
klm - 8 - O
keV

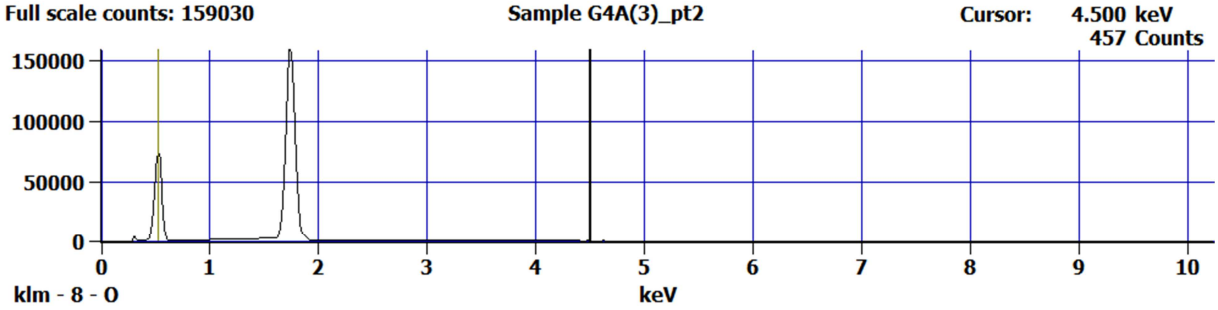
Full scale counts: 159030
Sample G4A(3)_pt2
Cursor: 4.500 keV
457 Counts
150000
100000
50000
0
0 1 2 3 4 5 6 7 8 9 10
klm - 8 - O
keV

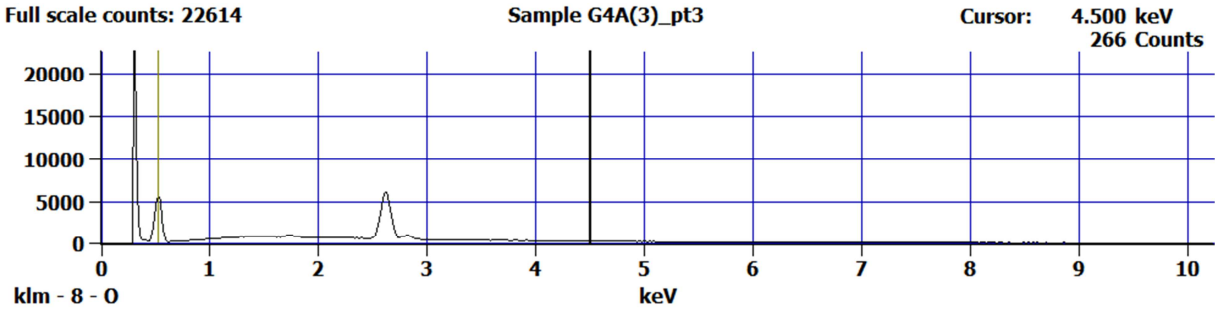
Full scale counts: 22614
Sample G4A(3)_pt3
Cursor: 4.500 keV
266 Counts
20000
15000
10000
5000
0
0 1 2 3 4 5 6 7 8 9 10
klm - 8 - O
keV

Sample 214(3)

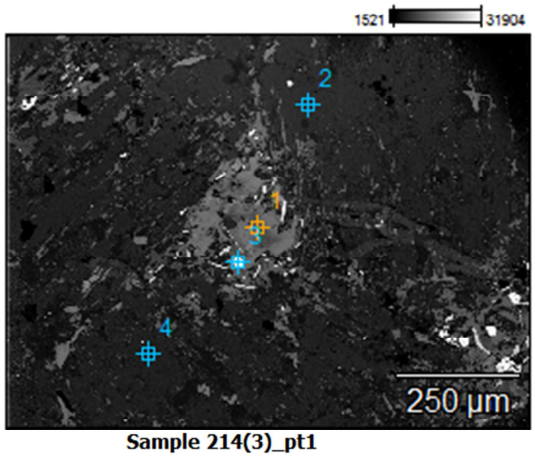
1521
31904
1
2
3
4
250 µm

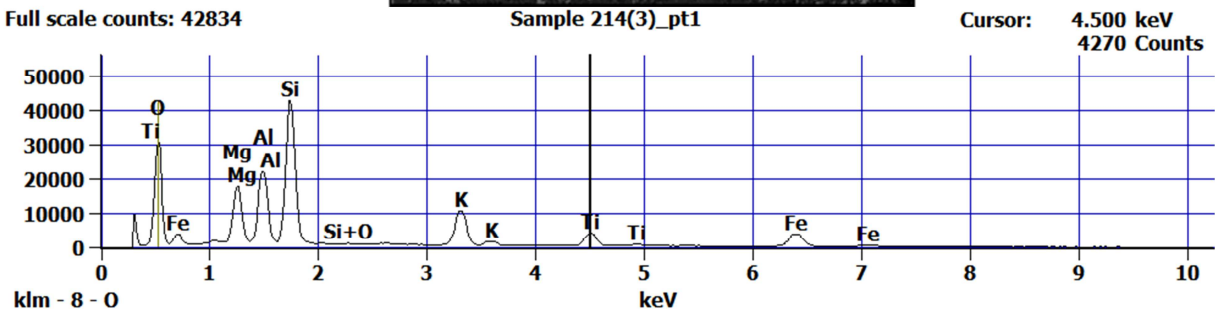
Full scale counts: 42834
Sample 214(3)_pt1
Cursor: 4.500 keV
4270 Counts
50000
40000
30000
20000
10000
0
O
Ti
Fe
Mg
Mg
Al
Al
Si
Si+O
K
K
Ti
Ti
Fe
Fe
0 1 2 3 4 5 6 7 8 9 10
klm - 8 - O
keV

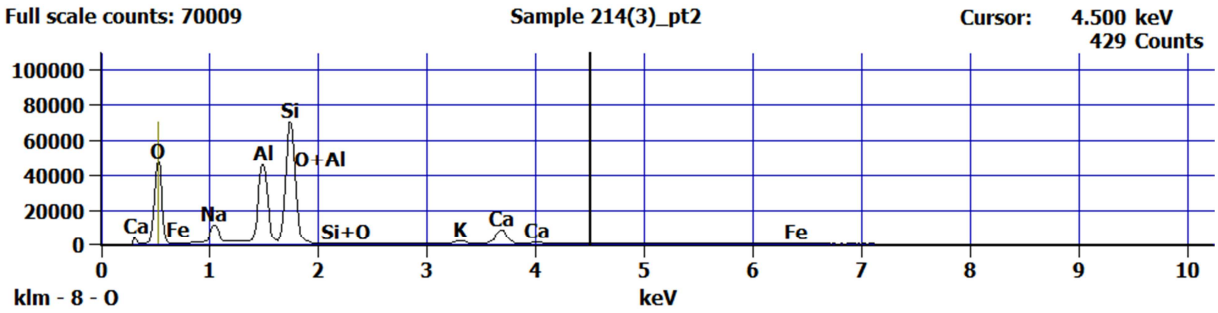
Full scale counts: 70009
Sample 214(3)_pt2
Cursor: 4.500 keV
429 Counts
100000
80000
60000
40000
20000
0
Ca
Fe
O
Na
Al
Si
O+Al
Si+O
K
Ca
Ca
Fe
0 1 2 3 4 5 6 7 8 9 10
klm - 8 - O
keV

Sample 214(3)

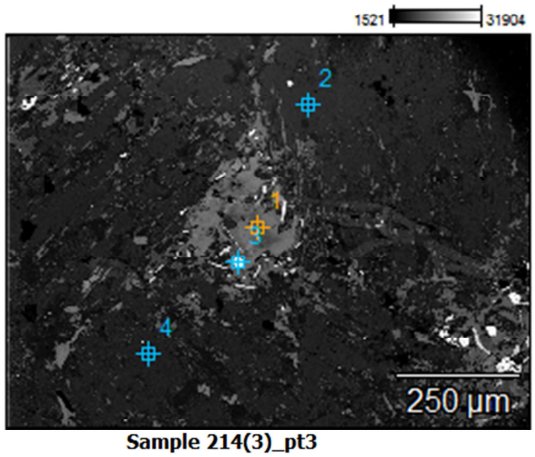
1521
31904
1
2
3
4
250 µm

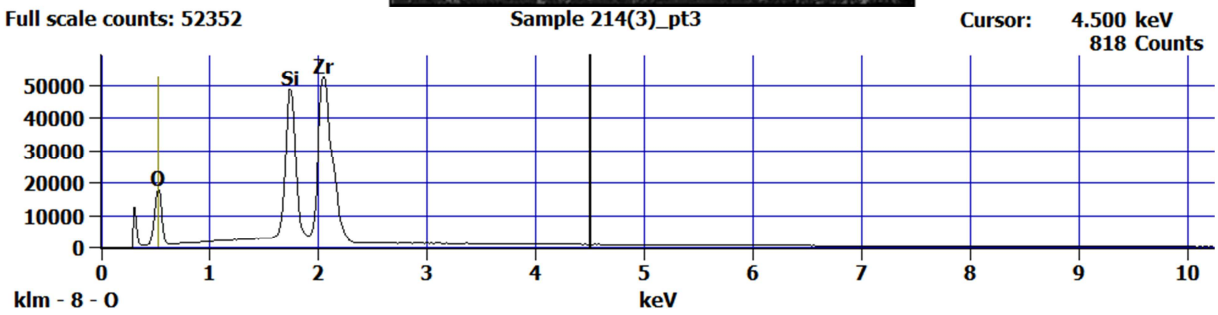
Full scale counts: 52352
Sample 214(3)_pt3
Cursor: 4.500 keV
818 Counts
50000
40000
30000
20000
10000
0
Si
Zr
O
0 1 2 3 4 5 6 7 8 9 10
klm - 8 - O
keV

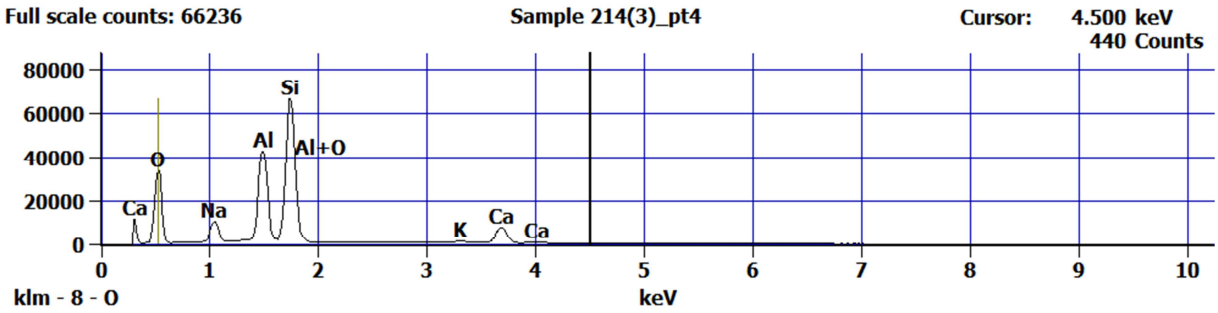
Full scale counts: 66236
Sample 214(3)_pt4
Cursor: 4.500 keV
440 Counts
80000
60000
40000
20000
0
Si
Al
Al+O
O
Ca
Na
K
Ca
Ca
0 1 2 3 4 5 6 7 8 9 10
klm - 8 - O
keV

Wed Feb 11 09:40:23 2015 Sample 108B pt 1
Gaussian Fit Chi² value: 65.870
Correction Method: ZAF
Acc.Voltage: 15.0 kV Take Off Angle: 30.2°

Element Line	Net Counts	Net Error	Int. Cps/nA	Int. Error	Element Wt.%	Compnd Wt.%	Compnd Error	Compnd Formula	Num. of Cations
O K	201026	± 898	4.74	4.74	42.23S	---	---		
Al K	301261	± 1163	6.14	6.14	11.74	± 0.05		Al2O3	3.626
Si L	0	± 0	0.00	0.00	---	---	---		
Si K	427416	± 1547	8.16	8.16	17.68	± 0.06		SiO2	5.247
Ca L	6	± 4	0.02	0.02	---	---			
Ca K	274161	± 933	4.92	4.92	17.67	± 0.06		CaO	3.675
Fe L	22570	± 202	1.07	1.07	---	---	---		
Fe K	59105	± 307	1.62	1.62	10.68	± 0.06		Fe2O3	1.594
			---			---			
Total			100.00		14.14				

Wed Feb 11 09:48:21 2015 Sample 108B pt 2
Gaussian Fit Chi² value: 509.869
Correction Method: ZAF
Acc.Voltage: 15.0 kV Take Off Angle: 30.2°

Element Line	Net Counts	Net Error	Int. Cps/nA	Int. Error	Element Wt.%	Compnd Wt.%	Compnd Error	Compnd Formula	Num. of Cations
O K	0	± 0	0.00	0.00	44.15S	---	---		
Na K	11306	± 172	0.91	0.91	0.86	± 0.01		Na2O	0.299
Mg K	203664	± 852	4.50	4.50	8.36	± 0.03		MgO	2.743
Al K	83371	± 431	2.27	2.27	3.62	± 0.02		Al2O3	1.071
Si L	0	± 0	0.00	0.00	---	---	---		
Si K	565179	± 2007	10.59	10.59	23.75	± 0.08		SiO2	6.742
Ca L	19685	± 237	1.25	1.25	---	---	---		
Ca K	133344	± 542	2.86	2.86	9.01	± 0.04		CaO	1.792
Ti L	54817	± 301	1.59	1.59	---	---	---		
Ti K	2505	± 122	0.64	0.64	0.26	± 0.01		TiO2	0.043
Fe L	9913	± 160	0.84	0.84	---	---	---		
Fe K	53367	± 288	1.52	1.52	9.98	± 0.05		Fe2O3	1.425
			---			---			
Total			100.00		14.12				

Fri Feb 13 13:56:39 2015 108 pt 3
Gaussian Fit Chi-squared value: 46.337 Errors:+/-1 Sigma
Correction Method: ZAF
Acc.Voltage: 15.0 kV Take Off Angle: 30.2 deg

Element Line	Net Error	Int. Cps/nA	Int. Error	Element Wt.%	Wt.% Error	Compnd Formula	Num. of Cations	
O K	+/-0	0.00	0.00	50.23	S ---	---		
S L	+/-0	0.00	0.00	---	---	---		
S K	+/-4365	7290.92		23.03	27.02	+/-0.09	SO3	---
Fe L	+/-693	982.55		3.66	---	---	---	
Fe K	+/-852	1429.67		4.50	22.76	+/-0.07	Fe2O3	---

Total				100.00				

Wed Feb 11 09:59:25 2015 Sample 131b pt 1
Gaussian Fit Chi² value: 410.029
Correction Method: ZAF
Acc.Voltage: 15.0 kV Take Off Angle: 33.1°

Element Line	Net Counts	Net Error	Int. Cps/nA	Int. Error	Element Wt.%	Wt.% Error	Compnd Formula	Num. of Cations	
O K	0	± 0	0.00	0.00	44.01	S ---	---		
Mg K	268861	± 1073		4.92	4.92	9.74	± 0.04	MgO	3.207
Al K	29220	± 243		1.11	1.11	1.15	± 0.01	Al2O3	0.341
Si L	0	± 0	0.00	0.00	---	---	---		
Si K	705261	± 2458		11.28	11.28	26.50	± 0.09	SiO2	7.547
Ca L	1	± 4	0.02	0.02	---	---	---		
Ca K	146717	± 580		2.66	2.66	9.29	± 0.04	CaO	1.853
Fe L	16425	± 174		0.80	0.80	---	---	---	
Fe K	52909	± 288		1.32	1.32	9.31	± 0.05	FeO	1.334
				----------			----------		
Total				100.00		14.28			

Wed Feb 11 10:04:47 2015 Sample 131b pt 2
Gaussian Fit Chi² value: 115.725
Correction Method: ZAF
Acc.Voltage: 15.0 kV Take Off Angle: 33.1°

Element Line	Net Counts	Net Error	Int. Cps/nA	Int. Error	Element Wt.%	Wt.% Error	Compnd Formula	Num. of Cations
O K	0	± 0	0.00	0.00	31.85	S ---	---	
Ti L	191847	± 795	3.65	3.65	---	---	---	
Ti K	414325	± 1280	5.87	5.87	32.30	± 0.10	TiO2	1.016
Fe L	61456	± 345	1.58	1.58	---	---	---	
Fe K	234352	± 762	3.50	3.50	35.85	± 0.12	FeO	0.967
Total			100.00		1.98			

Wed Feb 11 10:28:34 2015 Sample 131b pt 3
Gaussian Fit Chi² value: 556.263
Correction Method: ZAF
Acc.Voltage: 15.0 kV Take Off Angle: 33.1°

Element Line	Net Counts	Net Error	Int. Cps/nA	Int. Error	Element Wt.%	Wt.% Error	Compnd Formula	Num. of Cations
O K	0	± 0	0.00	0.00	42.24	S ---	---	
Mg K	163731	± 711	3.26	3.26	6.24	± 0.03	MgO	2.140
Al K	70419	± 386	1.77	1.77	2.77	± 0.02	Al2O3	0.855
Si L	0	± 0	0.00	0.00	---	---	---	
Si K	638785	± 2236	10.26	10.26	24.23	± 0.08	SiO2	7.190
Ca L	9	± 5	0.02	0.02	---	---	---	
Ca K	146951	± 579	2.66	2.66	9.17	± 0.04	CaO	1.907
Fe L	35961	± 252	1.16	1.16	---	---	---	
Fe K	88288	± 387	1.78	1.78	15.35	± 0.07	FeO	2.290
Total			100.00		14.38			

Wed Feb 11 10:22:32 2015 Sample 131b pt 4
Gaussian Fit Chi² value: 318.096
Correction Method: ZAF
Acc.Voltage: 15.0 kV Take Off Angle: 33.1°

Element Line	Net Counts	Net Error	Int. Cps/nA	Int. Error	Element Wt.%	Wt.% Error	Compnd Formula	Num. of Cations
O K	0	± 0	0.00	0.00	39.80	S ---	---	
Mg K	161365	± 708	3.25	3.25	6.19	± 0.03	MgO	2.047
Al K	183497	± 772	3.54	3.54	7.23	± 0.03	Al2O3	2.155
Si L	0	± 0	0.00	0.00	---	---	---	
Si K	457609	± 1652	7.58	7.58	18.01	± 0.07	SiO2	5.156
K L	3591	± 149	0.68	0.68	---	---	---	
K K	146980	± 591	2.71	2.71	7.95	± 0.03	K2O	1.634
Ti L	278389	± 944	4.33	4.33	---	---	---	
Ti K	33502	± 246	1.13	1.13	3.10	± 0.02	TiO2	0.521
Fe L	25935	± 249	1.14	1.14	---	---	---	
Fe K	103099	± 427	1.96	1.96	17.71	± 0.07	FeO	2.550
				---		---		
Total				100.00		14.06		

Wed Feb 11 10:26:10 2015 Sample 131b pt 5
Gaussian Fit Chi² value: 856.488
Correction Method: ZAF
Acc.Voltage: 15.0 kV Take Off Angle: 33.1°

Element Line	Net Counts	Net Error	Int. Cps/nA	Int. Error	Element Wt.%	Wt.% Error	Compnd Formula	Num. of Cations
O K	433118	± 2130	9.77	9.77	48.72	S ---	---	
Na K	168216	± 731	3.35	3.35	8.83	± 0.04	Na2O	1.009
Al K	332276	± 1265	5.80	5.80	10.84	± 0.04	Al2O3	1.056
Si L	0	± 0	0.00	0.00	---	---	---	
Si K	892776	± 3071	14.09	14.09	31.60	± 0.11	SiO2	2.956
				---		---		
Total				100.00		5.02		

Fri Feb 13 13:58:18 2015 131b pt 6
Gaussian Fit Chi-squared value: 56.583 Errors:+/-1 Sigma
Correction Method: ZAF
Acc.Voltage: 15.0 kV Take Off Angle: 33.1 deg

Element Line	Net Error	Int. Cps/nA	Int. Error	Element Wt.%	Wt.% Error	Compnd Formula	Num. of Cations
O K	+/-1584	1748.01		7.26	43.32S	---	---
Mg K	+/-695	729.29	3.18	5.90	+/-0.03	MgO	0.896
Al K	+/-312	222.65	1.43	1.84	+/-0.01	Al2O3	0.252
Si L	+/-0	0.00	0.00	---	---	---	
Si K	+/-2316	3038.47	10.61	23.99	+/-0.08	SiO2	3.155
Ca L	+/-4	0.03	0.02	---	---	---	
Ca K	+/-559	639.62	2.56	8.32	+/-0.03	CaO	0.766
Fe K	+/-419	459.34	1.92	16.64	+/-0.07	Fe2O3	1.100
Fe L	+/-288	210.68	1.32	---	---	---	
Total			100.00			6.169	

Wed Feb 11 10:38:12 2015 Sample 52B pt 1
Gaussian Fit Chi² value: 411.801
Correction Method: ZAF
Acc.Voltage: 15.0 kV Take Off Angle: 32.3°

Element Line	Net Counts	Net Error	Int. Cps/nA	Int. Error	Element Wt.%	Wt.% Error	Compnd Formula	Num. of Cations
O K	0	± 0	0.00	0.00	42.11S	---	---	
Mg K	139608	± 632	3.45	3.45	6.50	± 0.03	MgO	0.610
Si L	0	± 0	0.00	0.00	---	---	---	
Si K	574647	± 2047	11.19	11.19	25.80	± 0.09	SiO2	2.094
Ca L	8	± 5	0.03	0.03	---	---	---	
Ca K	131165	± 535	2.92	2.92	9.81	± 0.04	CaO	0.558
Fe L	25969	± 210	1.15	1.15	---	---	---	
Fe K	75819	± 351	1.92	1.92	15.78	± 0.07	FeO	0.644
Total				100.00			3.91	

Fri Feb 13 14:03:04 2015 52B pt 2
Gaussian Fit Chi-squared value: 30.841 Errors:+/-1 Sigma
Correction Method: ZAF
Acc.Voltage: 15.0 kV Take Off Angle: 32.3 deg

Element Line	Net Error	Cps/nA	Int. Error	Element Wt.%	Wt.% Error	Compnd Formula	Num. of Cations	
O K	+/-1047	1300.91	5.71	40.37	S	---	---	
Mg K	+/-485	536.81	2.65	4.51	+/-0.02	MgO	0.735	
Al K	+/-724	931.55	3.95	7.85	+/-0.03	Al2O3	1.153	
Si L	+/-0	0.00	0.00	---	---	---		
Si K	+/-1354	2004.87	7.39	16.95	+/-0.06	SiO2	2.392	
Cl L	+/-0	0.00	0.00	---	---	---		
Cl K	+/-203	99.26	1.11	1.04	+/-0.01	Cl	0.116	
K L	+/-0	0.00	0.00	---	---	---		
K K	+/-537	703.65	2.93	8.13	+/-0.03	K2O	0.824	
Ca L	+/-5	0.03	0.03	---	---	---		
Ca K	+/-141	9.60	0.77	0.13	+/-0.01	CaO	0.013	
Ti L	+/-135	15.68	0.74	---	---	---		
Ti K	+/-173	76.46	0.94	1.51	+/-0.02	TiO2	0.125	
Fe K	+/-412	534.34	2.25	19.51	+/-0.08	Fe2O3	1.384	
Fe L	+/-270	223.86	1.47	---	---	---		
Total			100.00			6.742		

Fri Feb 13 14:03:33 2015 52B pt 3
Gaussian Fit Chi-squared value: 23.007 Errors:+/-1 Sigma
Correction Method: ZAF
Acc.Voltage: 15.0 kV Take Off Angle: 32.3 deg

Element Line	Net Error	Int. Cps/nA	Int. Error	Element Wt.%	Wt.% Error	Compnd Formula	Num. of Cations	
O K	+/-1184	1497.83	6.47	40.34	S	---	---	
Na K	+/-128	13.02	0.70	0.20	+/-0.01	Na2O	0.035	
Mg K	+/-480	529.12	2.62	4.34	+/-0.02	MgO	0.707	
Al K	+/-767	1001.23	4.19	8.21	+/-0.03	Al2O3	1.207	
Si K	+/-1371	2034.68	7.49	16.81	+/-0.06	SiO2	2.374	
Si L	+/-0	0.00	0.00	---	---	---		
Cl K	+/-206	102.16	1.13	1.04	+/-0.01	Cl	0.116	
Cl L	+/-0	0.00	0.00	---	---	---		
K K	+/-547	724.27	2.99	8.16	+/-0.03	K2O	0.828	
K L	+/-0	0.00	0.00	---	---	---		
Ca L	+/-5	0.03	0.03	---	---	---		
Ca K	+/-136	2.42	0.74	0.03	+/-0.01	CaO	0.003	
Ti K	+/-171	72.50	0.93	1.39	+/-0.02	TiO2	0.115	
Ti L	+/-146	23.62	0.80	---	---	---		
Mn L	+/-0	0.00	0.00	---	---	---		
Mn K	+/-103	6.04	0.56	0.19	+/-0.02	MnO	0.014	
Fe K	+/-416	541.91	2.27	19.29	+/-0.08	Fe2O3	1.370	
Fe L	+/-325	252.02	1.78	---	---	---		
Total			100.00			6.770		

Fri Feb 13 14:04:16 2015 52b pt 4
Gaussian Fit Chi-squared value: 47.122 Errors:+/-1 Sigma
Correction Method: ZAF
Acc.Voltage: 15.0 kV Take Off Angle: 32.3 deg

Element Line	Net Error	Int. Cps/nA	Int. Error	Element Wt.%	Wt.% Error	Compnd Formula	Num. of Cations	
O K	+/-0	0.00	0.00	49.85	S	---	---	
Si L	+/-0	0.00	0.00	---	---	---		
Si K	+/-312	258.79	1.70	0.97	+/-0.01	SiO2	---	
S L	+/-0	0.00	0.00	---	---	---		
S K	+/-3760	6452.03	20.55	25.86	+/-0.08	SO3	---	
Fe L	+/-706	1041.11	3.86	---	---	---		
Fe K	+/-794	1350.39	4.34	23.32	+/-0.07	Fe2O3	---	
Total			100.00					

Fri Feb 13 14:05:31 2015 58b pt 1
Gaussian Fit Chi-squared value: 56.108 Errors:+/-1 Sigma
Correction Method: ZAF
Acc.Voltage: 15.0 kV Take Off Angle: 33.6 deg

Element Line	Net Error	Int. Cps/nA	Int. Error	Element Wt.%	Wt.% Error	Compnd Formula	Num. of Cations	
O K	+/-0	0.00	0.00	39.51	S ---	---		
S L	+/-0	0.00	0.00	---	---	---		
S K	+/-2434	3955.36		12.95	19.38	+/-0.06	SO3	---
Fe L	+/-271	210.34		1.44	---	---	---	
Fe K	+/-219	133.93		1.16	2.41	+/-0.02	Fe2O3	---
Zn L	+/-2772	4488.21		14.74	---	---	---	
Zn K	+/-448	682.73		2.38	38.69	+/-0.14	ZnO	---

Total				100.00				

Wed Feb 11 10:50:31 2015 Sample 58b pt 2
Gaussian Fit Chi² value: 45.867
Correction Method: ZAF
Acc.Voltage: 15.0 kV Take Off Angle: 33.6°

Element Line	Net Counts	Net Error	Int. Cps/nA	Int. Error	Element Wt.%	Wt.% Error	Compnd Formula	Num. of Cations
O K	192680	± 865	4.60	4.60	40.88	S ---	---	---
Al K	254744	± 1006	5.35	5.35	11.21	± 0.04	Al2O3	1.301
Si L	0	± 0	0.00	0.00	---	---	---	
Si K	380732	± 1395	7.42	7.42	17.74	± 0.06	SiO2	1.977
Ca L	6	± 4	0.02	0.02	---	---	---	
Ca K	244308	± 849	4.52	4.52	18.24	± 0.06	CaO	1.425
Fe L	20152	± 192	1.02	1.02	---	---	---	
Fe K	56683	± 297	1.58	1.58	11.93	± 0.06	FeO	0.669
			----------			----------		
Total			100.00			5.37		

Fri Feb 13 14:06:11 2015 58b pt 3
Gaussian Fit Chi-squared value: 43.141 Errors:+/-1 Sigma
Correction Method: ZAF
Acc.Voltage: 15.0 kV Take Off Angle: 33.6 deg

Element Line	Net Error	Int. Cps/nA	Int. Error	Element Wt.%	Error	Compnd Formula	Num. of Cations	
O K	+/-1060	1292.29	5.64	42.32	S	---	---	
Na K	+/-132	10.61	0.70	0.16	+/-0.01	Na2O	0.021	
Al K	+/-1111	1523.56	5.91	11.80	+/-0.05	Al2O3	1.323	
Si L	+/-0	0.00	0.00	---	---	---		
Si K	+/-1474	2159.07	7.84	17.84	+/-0.06	SiO2	1.921	
Ca K	+/-853	1306.70	4.54	17.32	+/-0.06	CaO	1.307	
Ca L	+/-4	0.03	0.02	---	---	---		
Fe L	+/-212	130.62	1.13	---	---	---		
Fe K	+/-287	282.70	1.53	10.56	+/-0.06	Fe2O3	0.572	
			---			---		
Total			100.00			5.143		

Wed Feb 11 19:54:32 2015 Sample 58B pt 4
Gaussian Fit Chi-squared value: 46.126 Errors:+/-1 Sigma
Correction Method: ZAF
Acc.Voltage: 15.0 kV Take Off Angle: 33.6 deg

Element Line	Net Error	Int. Cps/nA	Int. Error	Element Wt.%	Error	Compnd Formula	Num. of Cations	
O K	+/-1193	1482.38	6.35	42.09	S	---	---	
Al K	+/-1003	1350.46	5.34	10.41	+/-0.04	Al2O3	1.173	
Si K	+/-1534	2252.88	8.16	18.25	+/-0.07	SiO2	1.975	
Si L	+/-0	0.00	0.00	---	---	---		
Ca K	+/-856	1311.21	4.55	17.10	+/-0.06	CaO	1.297	
Ca L	+/-4	0.03	0.02	---	---	---		
Fe L	+/-235	165.37	1.25	---	---	---		
Fe K	+/-313	330.34	1.66	12.15	+/-0.06	Fe2O3	0.661	
			---			---		
Total			100.00			5.107		

Wed Feb 11 19:59:19 2015 Sample 214 pt 1
Gaussian Fit Chi-squared value: 166.870 Errors:+/-1 Sigma
Correction Method: ZAF
Acc.Voltage: 15.0 kV Take Off Angle: 33.2 deg

Element Line	Net Error	Int. Cps/nA	Int. Error	Element Wt.%	Error	Compnd Formula	Num. of Cations
O K	+/-0	0.00	0.00	41.98S	---	---	
Mg K	+/-619	711.40	3.22	5.98	+/-0.03	MgO	1.877
Al K	+/-763	945.83	3.97	8.22	+/-0.03	Al2O3	2.322
Si L	+/-0	0.00	0.00	---	---	---	
Si K	+/-1392	1970.27	7.25	17.37	+/-0.06	SiO2	4.714
K L	+/-207	5.40	1.08	---	---	---	
K K	+/-529	658.63	2.76	8.02	+/-0.03	K2O	1.564
Ti L	+/-686	913.28	3.57	---	---	---	
Ti K	+/-300	276.17	1.56	5.81	+/-0.03	TiO2	0.924
Fe L	+/-169	59.78	0.88	---	---	---	
Fe K	+/-313	323.62	1.63	12.61	+/-0.06	Fe2O3	1.722
Total			100.00			13.122	

Fri Feb 13 14:00:39 2015 sample 214 pt 2
Gaussian Fit Chi-squared value: 74.996 Errors:+/-1 Sigma
Correction Method: ZAF
Acc.Voltage: 15.0 kV Take Off Angle: 33.2 deg

Element Line	Net Error	Int. Cps/nA	Int. Error	Element Wt.%	Error	Compnd Formula	Num. of Cations
O K	+/-1356	1656.93	7.06	46.93S	---	---	
Na K	+/-421	419.78	2.19	5.00	+/-0.03	Na2O	0.593
Al K	+/-1458	2035.59	7.59	14.24	+/-0.05	Al2O3	1.440
Si L	+/-3	0.01	0.02	---	---	---	
Si K	+/-2222	3312.11	11.57	25.96	+/-0.09	SiO2	2.521
K L	+/-0	0.00	0.00	---	---	---	
K K	+/-186	89.08	0.97	1.02	+/-0.01	K2O	0.071
Ca K	+/-444	523.38	2.31	6.86	+/-0.03	CaO	0.467
Ca L	+/-82	19.57	0.43	---	---	---	
Total			100.00			5.091	

Wed Feb 11 20:09:03 2015 Sample 214 pt 3
Gaussian Fit Chi-squared value: 261.755 Errors:+/-1 Sigma
Correction Method: ZAF
Acc.Voltage: 15.0 kV Take Off Angle: 33.2 deg

Element Line	Net Error	Int. Cps/nA	Int. Error	Element Wt.%	Wt.% Error	Compnd Formula	Num. of Cations
O K	+/-559	590.00	2.91	35.97	S ---	---	
Si L	+/-0	0.00	0.00	---	---	---	
Si K	+/-1551	2228.32	8.08	17.13	+/-0.06	SiO2	1.085
Zr L	+/-2090	3856.96	10.89	46.90	+/-0.13	ZrO2	0.915
Zr M	+/-4	0.01	0.02	---	---	---	
Total			100.00				2.000

Wed Feb 11 20:10:25 2015 Sample 214 pt 4
Gaussian Fit Chi-squared value: 208.453 Errors:+/-1 Sigma
Correction Method: ZAF
Acc.Voltage: 15.0 kV Take Off Angle: 33.2 deg

Element Line	Net Error	Int. Cps/nA	Int. Error	Element Wt.%	Wt.% Error	Compnd Formula	Num. of Cations
O K	+/-983	1018.17	5.12	47.09	S ---	---	
Na K	+/-390	366.18	2.03	4.73	+/-0.03	Na2O	0.559
Al K	+/-1356	1863.51	7.06	14.11	+/-0.05	Al2O3	1.421
Si L	+/-0	0.00	0.00	---	---	---	
Si K	+/-2104	3105.20	10.96	26.32	+/-0.09	SiO2	2.548
K L	+/-0	0.00	0.00	---	---	---	
K K	+/-180	78.34	0.94	0.97	+/-0.01	K2O	0.067
Ca K	+/-419	477.18	2.18	6.78	+/-0.03	CaO	0.460
Ca L	+/-5	0.05	0.03	---	---	---	
Total			100.00				5.055

Fri Feb 13 14:07:50 2015 sample G41 pt 1
Gaussian Fit Chi-squared value: 32.344 Errors:+/-1 Sigma
Correction Method: ZAF
Acc.Voltage: 15.0 kV Take Off Angle: 30.4 deg

Element Line	Net Error	Int. Cps/nA	Int. Error	Element Wt.%	Wt.% Error	Compnd Formula	Num. of Cations	
O K	+/-1057	1334.81	5.86	42.38	S	---	---	
Na K	+/-231	153.09	1.28	2.20	+/-0.02	Na2O	0.361	
Mg K	+/-587	708.47	3.25	5.51	+/-0.03	MgO	0.855	
Al K	+/-642	809.75	3.56	6.38	+/-0.03	Al2O3	0.892	
Si K	+/-1579	2416.94	8.75	18.82	+/-0.07	SiO2	2.530	
Si L	+/-0	0.00	0.00	---	---	---		
K K	+/-203	105.81	1.12	1.12	+/-0.01	K2O	0.108	
K L	+/-0	0.00	0.00	---	---	---		
Ca L	+/-5	0.03	0.03	---	---	---		
Ca K	+/-516	686.89	2.86	8.32	+/-0.03	CaO	0.784	
Ti K	+/-232	171.46	1.29	3.15	+/-0.02	TiO2	0.249	
Ti L	+/-137	21.65	0.76	---	---	---		
Fe K	+/-322	359.49	1.78	12.13	+/-0.06	Fe2O3	0.820	
Fe L	+/-221	152.98	1.22	---	---	---		
Total			100.00			6.599		

Fri Feb 13 14:08:29 2015 sample G4a pt 2
Gaussian Fit Chi-squared value: 48.843 Errors:+/-1 Sigma
Correction Method: ZAF
Acc.Voltage: 15.0 kV Take Off Angle: 30.4 deg

Element Line	Net Error	Int. Cps/nA	Int. Error	Element Wt.%	Wt.% Error	Compnd Formula	Num. of Cations	
O K	+/-1116	1303.42	5.64	42.58	S	---	---	
Al K	+/-1272	1684.91	6.42	12.31	+/-0.05	Al2O3	1.714	
Si K	+/-1642	2303.43	8.29	18.01	+/-0.06	SiO2	2.410	
Si L	+/-0	0.00	0.00	---	---	---		
Ca K	+/-961	1432.44	4.85	17.52	+/-0.06	CaO	1.642	
Ca L	+/-4	0.03	0.02	---	---	---		
Fe L	+/-206	115.84	1.04	---	---	---		
Fe K	+/-297	279.64	1.50	9.58	+/-0.05	Fe2O3	0.645	
Total			100.00			6.411		

Fri Feb 13 14:09:00 2015 sample G4a pt 3
Gaussian Fit Chi-squared value: 620.932 Errors:+/-1 Sigma
Correction Method: ZAF
Acc.Voltage: 15.0 kV Take Off Angle: 30.4 deg

Element Line	Net Int. Error	Cps/nA	Int. Error	Element Wt.%	Wt.% Error	Compnd Formula	Num. of Cations
O K	+/-2095	2368.98		10.58	53.26	S ---	---
Si L	+/-0	0.00	0.00 ---	---	---		
Si K	+/-4918	7312.95		24.84	46.74	+/-0.16	SiO2 1.000
			----------		----------		
Total			100.00		1.000		